

Wetting, Prewetting and Surface Freezing Transitions in Fluid Ga-Bi and Ga-Pb Alloys: A Surface Light Scattering Study

Zur Erlangung des akademischen Grades eines
DOKTORS DER NATURWISSENSCHAFTEN

(Dr. rer. nat.)

von der Fakultät für Chemie

der

Universität Karlsruhe (TH)

angenommene

DISSERTATION

von

M.Sc. Ahmed Ayyad

aus Ost Jerusalem, Palästina

Dekan: Prof. Dr. M. Metzler

1. Gutachter: Prof. Dr. W. Freyland

2. Gutachter: Prof. Dr. M. Ballauff

Tag der mündlichen Prüfung: 25. Oktober 2002

Contents

Zusammenfassung, Abstract	1
1 Introduction	5
2 Some basic aspects of fluid interfaces and capillary wave spectroscopy	10
2.1 Surface structure and energy of liquid metals	10
2.2 Wetting and surface phase transitions	12
2.2.1 <i>Wetting and Cahn's scenario of critical point wetting</i>	12
2.2.2 <i>First and second order wetting transitions</i>	13
2.2.3 <i>Why is wetting a phase transition?</i>	14
2.2.4 <i>Wetting transitions in binary liquid mixtures</i>	15
2.3 Capillary waves at liquid surfaces and interfaces	19
2.3.1 <i>Physical origin of capillary waves</i>	19
2.3.2 <i>Dispersion equation of capillary waves at a free liquid surface</i>	20
2.3.3 <i>Modification of the dispersion equation</i>	20
2.3.4 <i>Scattering of light by capillary waves</i>	22
2.3.5 <i>The necessity of heterodyne technique for the detection of light scattered by capillary waves</i>	24
2.3.6 <i>The spectrum of the scattered light and its relation to the power spectrum of capillary waves</i>	26
3 Experiment	29
3.1 Experimental set-up for surface light scattering	29
3.2 Materials and sample preparation	30
3.2.1 <i>Preparation of the pure liquid Gallium sample</i>	32
3.2.2 <i>Preparation of liquid Ga-Bi and Ga-Pb sample alloys</i>	33
3.3 Measuring procedure	35
3.4 Wave number measurements and data analysis	40
3.4.1 <i>Measurements of the incident and the scattering angles</i>	40
3.4.2 <i>Data analysis, instrumental broadening corrections and error discussion</i>	43
4 Results	46
4.1 Surface tension of pure liquid Ga and its temperature dependence	46
4.2 Temperature and composition dependence of the surface energy of Ga-Bi and Ga-Pb liquid alloys	49
4.3 Estimate of the viscosity of pure Ga, pure Bi, Ga-Bi and Ga-Pb liquid alloys	59

4.4 Surface freezing in Ga-Bi and Ga-Pb liquid alloys.....	61
5 Discussion	75
5.1 Anomalous behaviour of capillary wave damping in liquid metals and alloys.....	75
5.2 Wetting and prewetting transitions in liquid $\text{Ga}_x\text{Bi}_{1-x}$ and $\text{Ga}_x\text{Pb}_{1-x}$	78
5.2.1 <i>Surface excess entropy and its dependence on x_{Bi} or x_{Pb}</i>	78
5.2.2 <i>Analysis of the concentration dependence of the surface free energy according to the Gibbs adsorption equation</i>	82
5.2.3 <i>Inconsistency of the monolayer model with the Gibbs adsorption equation</i>	91
5.2.4 <i>Analysis of the characteristic change of the surface quantities by a multilayer model</i>	93
5.2.5 <i>Estimate of the thickness of the interfacial region</i>	98
5.3 Surface freezing and surface viscoelasticity of Ga-Bi and Ga-Pb liquid alloys..._	101
5.3.1 <i>Surface excess viscoelastic modulus of Bi and Pb solid- like films</i>	102
5.3.2 <i>Concentration and temperature dependence of the surface excess viscoelastic modulus</i>	105
Appendix	111
References	123

Zusammenfassung

Die Grenzflächenenergie und Entropie sowie teilweise die Viskosität flüssiger Ga-reicher Ga-Bi und Ga-Pb Legierungen wurden bei Temperaturen bis 620 K untersucht. Hierzu wurde die Methode der Kapillarwellenspektroskopie erstmals für Messungen bei erhöhten Temperaturen eingesetzt, um die Grenzflächeneigenschaften der fluiden Legierung berührungslos messen zu können. Die Auswertung der konzentrationsabhängigen Grenzflächenenergie im Konzentrationsbereich von $10^{-2} \lesssim x_{Bi} \lesssim 10^{-1}$ bei Temperaturen von $450 \text{ K} \lesssim T \lesssim 500 \text{ K}$ nach der Gibbs Adsorptionsgleichung ergibt einen Grenzflächenexzess von $\Gamma_{Bi} \sim 1.32 \cdot 10^{-5} \text{ mol m}^{-2}$. Dies beweist, dass an der Grenzfläche flüssig/dampfförmig reines Bi angereicht ist, das mit zunehmender Temperatur leicht abnimmt. Bei kleineren Molenbrüchen x_{Bi} nimmt Γ_{Bi} diskontinuierlich ab, so wie es für einen Vorbenetzungsphasenübergang 1. Ordnung zu erwarten ist. Ein ähnliches Verhalten wird für das Ga-Pb System gefunden, wobei im Konzentrationsbereich von $10^{-3} \lesssim x_{Pb} \lesssim 10^{-2}$ und bei Temperaturen von $550 \text{ K} \lesssim T \lesssim 600 \text{ K}$ eine Grenzflächenadsorption von $\Gamma_{Pb} \sim 1.2 \cdot 10^{-5} \text{ mol m}^{-2}$ gefunden wird. Die hier beobachteten Änderungen der Grenzflächenenergie und Entropie widersprechen einem einfachen Einschichtmodell zur Beschreibung der Grenzflächenphase, was kürzlich aus Röntgenreflexionsmessungen gefolgert wurde. Stattdessen lassen sich die charakteristischen Änderungen der hier gemessenen thermodynamischen Grenzflächengrößen zwanglos in einem Mehrschichtmodell beschreiben. Die Dicke der mehrschichtigen Grenzflächenphase konnte erstmals aus den Änderungen der relativen Grenzflächenentropie abgeschätzt werden. Danach werden für das Ga-Bi System Werte im Bereich 10-20 Å gefunden und entsprechend für das Ga-Pb Werte zwischen 6 und 12 Å, wobei ein Anstieg der dicken Benetzungsfilme bei Annäherung an die vollständige Benetzung am monotektischen Punkt erfolgt. Alle Isoplethen der Grenzflächenenergie zeigen ein deutliches Abknicken bei Temperaturen von 10-20 K oberhalb der Liquiduskurve. Die zugehörigen diskontinuierlichen Sprünge in der Grenzflächenentropie weisen auf einen Phasenübergang 1. Ordnung des Grenzflächenerstarrens hin, der kürzlich für das Ga-

Bi System mit Hilfe von SHG Messungen gefunden wurde. Das Grenzflächenerstarren in Ga-Legierungen wurde in diesem Bereich im Detail erstmals mit Hilfe der Kapillarwellenspektroskopie bei verschiedenen Wellenzahlen und Temperaturen untersucht. Dieser Grenzflächenphasenübergang ist gekennzeichnet durch eine sprunghafte Änderung der Grenzflächenenergie sowie durch ein Hystereseverhalten, was auf einen Grenzflächenphasenübergang 1. Ordnung hinweist. Eine Analyse der Wellenzahlabhängigkeit der Kapillarwellenspektren liefert Aussagen über die viskoelastischen Eigenschaften der erstarrten Grenzflächenfilme mit Dicken im Bereich von $\sim 1\text{nm}$. Insbesondere zeigt der Grenzflächenexzess viskoelastischen Moduli Eigenschaften, die für einen metallischen grenzflächenerstarrten strukturierten Film sprechen, der an der Grenzfläche der fluiden Ga-Bi und Ga-Pb beim Abkühlen gebildet wird. Mit Zunahme der Bi-Konzentration bei Annäherung an den monotektischen Punkt verschwindet der viskoelastische Grenzflächenexzessmodul. Im System Ga-Pb sind diese Charakteristika weniger ausgeprägt. In einem einfachen Keimbildungsmodell kann der Übergang des Grenzflächenerstarrrens in diesen Legierungen durch ein 2D-Gefrieren von stark unterkühlten Benetzungsfilmen beschrieben werden. Diese Erklärung ist auch konsistent mit dem "tetra point wetting scenario".

Abstract

The surface energy, surface entropy and, partly, the viscosity of liquid Ga-Bi and Ga-Pb alloys at compositions mainly in the Ga-rich phase region have been studied at temperatures up to 620 K. Measurements have been performed by the non-invasive method of capillary wave spectroscopy which has been applied for the first time to investigate the surface properties of a liquid alloy at elevated temperatures. For liquid Ga-Bi alloys, analysis of the concentration dependence of the surface energy according to the Gibbs adsorption equation yields that in the composition range of $10^{-2} \lesssim x_{Bi} \lesssim 10^{-1}$ and at temperatures of $450 \text{ K} \lesssim T \lesssim 500 \text{ K}$ a surface excess of $\Gamma_{Bi} \sim 1.32 \cdot 10^{-5} \text{ mol m}^{-2}$ resides at the liquid-vapour interface corresponding to pure Bi, with a tendency to decrease with increasing temperature. At lower x_{Bi} a reduction of Γ_{Bi} occurs which is evidence of a prewetting transition. The same trend is found for the Ga-Pb system with $\Gamma_{Pb} \sim 1.2 \cdot 10^{-5} \text{ mol m}^{-2}$ in the composition range of $10^{-3} \lesssim x_{Pb} \lesssim 10^{-2}$ and for temperatures between $550 \text{ K} \lesssim T \lesssim 600 \text{ K}$. The variations of surface energy and entropy with composition are not consistent with a description by a simple monolayer model as was deduced from X-ray reflectivity results. Instead it is found that a multilayer model qualitatively accounts for the characteristic change of the surface quantities. The thickness of the multilayer interfacial region is estimated from the change of the relative surface entropy. This yields values between 10 and 20 Å for Ga-Bi alloys and between 6 and 12 Å for the Ga-Pb alloy with a trend for an increasing number of surface layers towards the complete wetting transition at the monotectic point. All isopleths of the surface energy exhibit clear kinks at temperatures 10-20 K above the liquidus curve for compositions below the monotectic point. The corresponding discontinuity of the surface entropy is consistent with a first order transition of surface freezing reported recently for the Ga-Bi system by SHG measurements.

Surface freezing in these Ga-based alloys has been studied in detail for the first time by capillary wave spectroscopy at various wave numbers and temperatures. The surface freezing transition is marked by a sharp drop of the surface tension and a

hysteresis behaviour indicating a first order interfacial phase transition. Analysis of the capillary wave spectra yields information on the surface excess viscoelastic modulus governing shear normal to the surface plane which is found to be consistent with a metallic solid-like surface freezing film on top of the Ga-Bi or Ga-Pb alloy. The magnitude of the observed drop in the surface tension has been found to decrease with increasing Bi concentration and vanishes approaching the monotectic point. Surface freezing in an eutectic Ga-Pb alloy is less marked than in its Ga-Bi counterpart. In a simple nucleation model the surface freezing in these alloys is described by the freezing of the strongly undercooled wetting films consistent with the tetra point wetting scenario.

Chapter 1

Introduction

Wetting is a phenomenon that occurs as a consequence of the existence of surfaces and interfaces. A boundary or surface is defined as the termination of the bulk state (a solid or liquid) where the equations based on three-dimensionality are not sufficient to describe the complete physical state of the system [1]. At the surface region bulk symmetry is perturbed and gives rise to altered interaction forces. This broken symmetry, sketched in Fig. 1, is responsible for the peculiar behaviour of surfaces and interfaces which leads to different types of phenomena e.g. surface tension, the existence of capillary waves at liquid surfaces etc. In addition a surface of a solid is considered to be a point of defects, which induce e.g. surface melting of certain pure metals at temperatures below the bulk melting point [2].

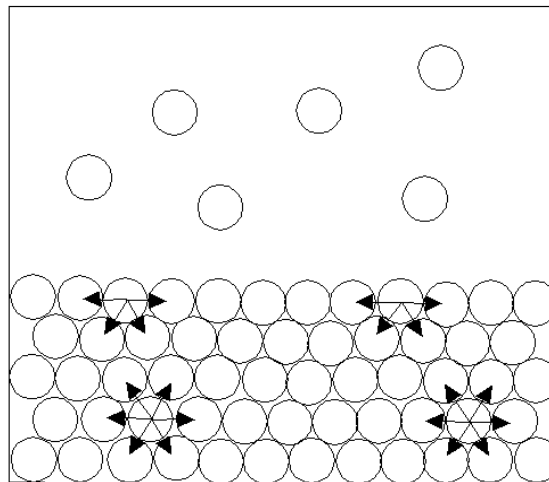


Figure 1. Symmetry and asymmetry of interaction forces of particles in the interior and at the surface of a solid or liquid phase. The interaction forces in the gas phase are practically negligible compared to the condensed phase [1].

To visualize wetting phenomena, consider for example a liquid drop placed on a surface. Three distinguishable situations may result depending on the contact angle θ formed between the drop and the surface. If θ is zero, the drop has spread across the surface and the resulting situation is called complete wetting. If on the other hand θ is

between 0° and 180° the drop does not spread or partially wets the surface. The remaining probable situation is that $\theta > 180^\circ$ and in this case the surface is dry.

In 1977 Cahn [3] pointed out, through his pioneering study of the asymptotic behaviour of the Young's equation, the expectation that transition from partial to complete wetting should occur in any three-phase system including systems displaying a liquid miscibility gap (e.g. binary liquid mixtures) and that the transition involves a prewetting phenomenon at a temperature $T_w < T_c$, where T_c is the critical temperature of a one-component fluid in case of liquid drops on substrates or a critical temperature of mixing in case of binary liquid mixtures and T_w is a wetting transition temperature. The order of the wetting transition is defined by the changes of the thickness as a function of temperature of the wetting film at T_w and the consequent discontinuity in the free energy derivatives at the transition temperature.

Clearly, wetting transition is an interfacial phase transition from partial to complete wetting. Cahn's prediction stimulated many investigations of these wetting and prewetting phenomena both theoretically and experimentally, for reviews see e.g. [4, 5]. Experimental studies mainly focused on systems characterized by Van der Waal's interactions. Only recently a few examples of metallic systems have been studied experimentally. Among these are the binary liquid alloys Ga-Bi and Ga-Pb which exhibit a liquid-liquid miscibility gap below a critical temperature T_c . An unusual surface segregation in the Ga-Bi system was first reported by Perepezko *et al* [6] who studied the undercooling of finely dispersed liquid alloy droplets and, on solidification of Ga-rich droplets, found a large scale segregation of a Bi-phase shell surrounding a central Ga-phase. The authors explain this observation by Cahn's theory of critical point wetting [3]. Stimulated by these observations Freyland *et al* have studied the liquid-vapour interface of Ga-rich alloys at thermal equilibrium by ellipsometry [7, 8]. These results show that along the coexistence curve approaching the monotectic temperature of $T_{mon} = 495$ K the thickness of this film jumps to a value of the order of 50 \AA which is characteristic of a complete wetting transition which experimentally was first visible at these conditions. Several X-ray reflectivity and grazing incidence diffraction measurements have been performed in Ga-rich alloys to probe the microscopic structure of the liquid-vapour interface, both the normal and in-plane structure [9-11]. From these data it is concluded that a complete monolayer of the low surface tension Bi-component segregates at the interface and that the structure of this surface layer is like that of supercooled bulk liquid bismuth. Above the monotectic

temperature a Bi-rich wetting film of about 30 Å thickness intrudes between the Bi-monolayer and the Ga-rich bulk liquid [11]. The concentration profile of this film shows a highly diffuse interface with the bulk phase. Very recently, surface freezing has been observed at the surface of Ga-rich liquid alloys at temperatures clearly above those of the liquidus curve for $T < T_{mon}$ [12].

Very similar interfacial phenomena have been observed in the liquid Ga-Pb system. Using Auger spectroscopy Chatain and Wynblatt [13] measured the surface composition of a Ga-rich liquid in equilibrium with Pb-rich solid and from the logarithmic divergence of the thickness of the surface layer they found evidence of a complete wetting transition approaching the monotectic point. From a detailed analysis of surface energy measurements by a layering model [14] of the interface composition profile they concluded that complete wetting extends into the metastable regime of liquid-liquid coexistence [15]. The wetting transition temperature and the prewetting critical point are estimated to be below 300 K [16]. Indications of surface freezing in an eutectic Ga-Pb alloy have been reported recently by Rice and coworkers who studied the liquid interface by X-ray reflectivity and diffraction measurements [17]. Surface melting and surface freezing are peculiar types of wetting transitions [5, 18]. In the former case, the solid-vapour interface is completely wet by the liquid phase approaching the triple point along the sublimation line. Examples that have been investigated intensively, both experimentally and theoretically, include metals, rare gas crystals and ice – see e.g. [19-21]. In surface freezing in an one-component system a crystalline or solid-like film forms at the liquid-vapour interface at temperatures above those for bulk freezing. Among the best studied examples are alkanes and alcohols [22-27]. For pure liquid metals it has been argued that surface induced freezing in general should be absent [28].

Recently, first observations of surface freezing in liquid binary metallic alloys, the Ga-Pb [17] and the Ga-Bi systems [29], have been reported. X-ray reflectivity and grazing incidence X-ray diffraction measurements of Ga-rich Ga-Pb alloys (0.054 at % Pb) indicate that the liquid-vapour interface is stratified for several atomic diameters into the bulk liquid. Surface freezing in liquid Ga-Bi alloys has been studied by second harmonic and plasma generation measurements for compositions between the eutectic and the monotectic point. In this composition range solid-like films are observed on top of the bulk liquid phase at surface freezing temperatures T_{sf} clearly above the liquidus line. On melting of these films hysteresis behaviour is

found, indicating a first order interfacial phase transition. An estimate of the lower limit of the film thickness from SHG measurements yields values of the order of one nm [29]. The relation of this freezing transition with the observed wetting transition in Ga-Bi [7] is of particular interest. Possibly, the surface freezing in these alloys reflects the freezing of the respective Bi-rich wetting films.

The presence of wetting and prewetting transitions and the related surface freezing transition in the metallic binary liquid alloys Ga-Bi and Ga-Pb can be detected by surface energy measurements as a function of temperature and composition [14], since surface energy is sensitive to changes in adsorption through the Gibbs adsorption isotherm. The existing studies of the temperature and composition dependence of the surface energy of binary liquid alloys have been made using invasive methods, mainly the sessile drop method [15, 30] and to a smaller extent by the maximum pressure method. These and other existing tensiometers (e.g. Wilhelmy plate method, ring method) can perturb the mechanical stability of the surface under study and may be sources of impurities. For example the Wilhelmy plate method failed to detect a well-defined discontinuous jump in the surface tension upon surface freezing of n-heptadecane as a function of temperature [22] which was later detected by the non-invasive optical method of capillary wave spectroscopy [23].

The aim of this work is to study wetting and prewetting transitions and the related surface freezing transitions in the metallic binary liquid alloys Ga-Bi and Ga-Pb by capillary wave spectroscopy. We report measurements of the surface tension of liquid Ga-Bi and Ga-Pb alloys as a function of composition and temperature up to 620 K. The surface tension of an alloy at these conditions has been determined for the first time by surface light scattering or capillary wave spectroscopy. We have focused on the Ga-rich region to get further insight into the wetting characteristics from the change of the surface energy σ and surface adsorption Γ . Information on the surface entropy is obtained from the temperature coefficient of σ .

In addition we report the first investigation of surface freezing in these Ga-based alloys and the hysteresis behaviour of the freezing transition. Capillary wave spectroscopy provides information on the viscoelasticity of the surface freezing films.

The outline of the thesis is as follows: the basic aspects of wetting and prewetting transitions and the theory of capillary wave spectroscopy are given in chapter 2. In

chapter 3, a description of the experimental set-up, sample preparation and the measuring procedure follows. The experimental results are presented in chapter 4. Chapter 5 provides a discussion of the obtained results. The main topics discussed are:

- 1- A 2D-phase diagram known as the prewetting line obtained from changes in the slopes of the Gibbs adsorption isotherms for the Ga-Bi system.
- 2- The linkage between a wetting film of Bi or Pb and surface freezing of these films on top of the bulk liquid Ga-Bi and Ga-Pb.
- 3- Viscoelasticity of these surface freezing films.

Chapter 2

Some basic aspects of fluid interfaces and capillary wave spectroscopy

2.1 Surface structure and energy of liquid metals

From experiment and theory [31] it is well known that conduction electrons in metals are nearly free. From theory it has been anticipated that X-ray and neutron diffraction experiments on liquid metals would reveal that a liquid metal consists of mobile positive ions and conduction electrons [31]. Thus a liquid metal is a two-component system in contrast to a dielectric liquid which can be described as an one-component fluid [32-34]. The ions are coupled to the conduction electrons through Coulomb interactions.

From the structural point of view the fundamental differences between liquid metals and dielectric fluids are not manifested in the bulk structure of the two. The pair correlation function describing the structure of liquids is almost identical for a free-electron liquid metal (e.g. Na) and a simple dielectric liquid, such as liquid Ar, over the whole liquid density range [35]. However the surface structure of a liquid metal differs from that of a dielectric liquid because the interatomic interactions depend strongly on the changing density along the liquid-vapour interface in the case of a liquid metal. The transition from the liquid to the vapour phase corresponds to a transition from a metallic to a non-metallic state. By contrast the type of interactions remains the same along the liquid-vapour transition in the case of a dielectric liquid. The conduction electrons at the surface of a liquid metal create a sort of hard wall that suppresses positional fluctuations of the ion cores near surface. A direct consequence of this is the prediction of atomic layering at the surface. The latter is described as positional ordering of the ions normal to the surface [36]. The distribution of positive charges is discontinuous at the surface of a liquid metal [32-34] which will induce oscillations in the essentially non-classical electron density near the surface. The distribution of the positive charges depends on the excess electron density. As a

consequence the ionic and electronic distributions may both have oscillations in the transition region near the surface.

Figure 2.1 shows the recently observed oscillatory electron density profiles of the Gallium-vapour interface at different temperatures as indicated in the figure. For more details on Fig. 2.1 and the model used to generate these types of oscillatory electron density profiles the reader is referred to ref. [37].

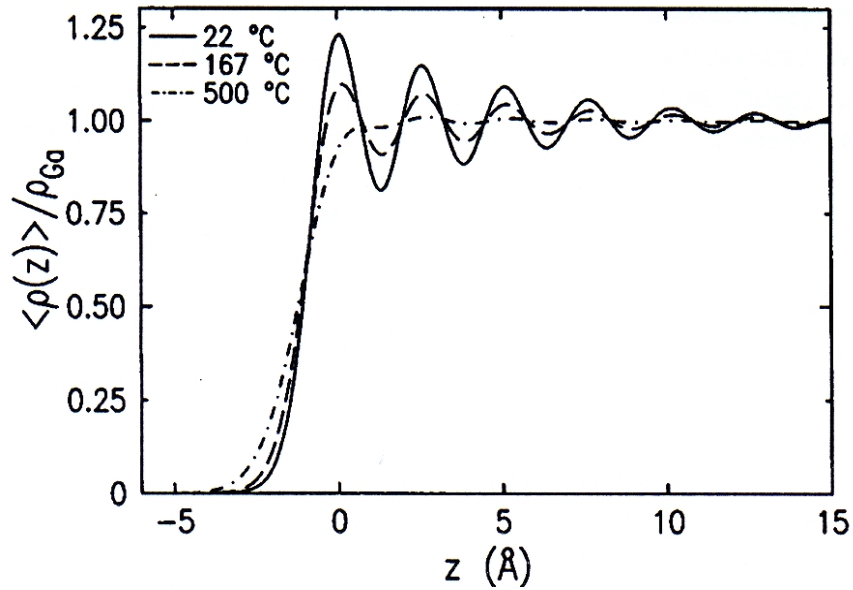


Figure 2.1. Oscillatory electron density profile of the Gallium-vapour interface at different temperatures taken from ref. [37].

The surface energy σ of a liquid metal system is about one order of magnitude greater than that of dielectric liquids [38]. It ranges from 70 (for Cs), to 2700 mJm⁻² (for Re) at their melting points [38]. It differs substantially from that of dielectric liquids due to the expected non-coincidence of the electronic and ionic distributions (though charge neutrality must be reserved). Therefore, there is an electric double layer contribution to the surface energy which is absent in the case of dielectric liquids. Frenkel e.g. [38] attributed a large contribution to the surface energy of liquid Hg from this electrostatic part. Another contribution to the surface energy of a liquid metal arises from the self-energy term due to the coulombic or screened coulombic interaction of an ion with its neutralizing cloud of conduction electrons. The latter depends on the local electron density. A third contribution to σ of a liquid metal

arises from the electronic excitations in a form of plasmon modes which differ from bulk to surface. Another feature of certain liquid metals is that the temperature variation of σ ($d\sigma/dT$) is more sensitive to the surface structure than σ itself. Anomalous positive $d\sigma/dT$ was observed for Cu, Zn and Cd 100 K above the melting point [38]. This anomalous behaviour was attributed to a crystalline nature of the utmost surface layers of these metals. In these cases the familiar monotonic decreasing temperature dependence was observed only at higher temperatures where the liquid surface thermally delocalises, and systems exhibiting positive slopes were shown to ultimately invert their behaviours [38].

2.2 Wetting and surface phase transitions

2.2.1 Wetting and Cahn's scenario of critical point wetting

Consider a liquid drop resting on a solid substrate (e.g. a water drop on a glass plate) as shown in Fig. 2.2. It is a common natural phenomenon.

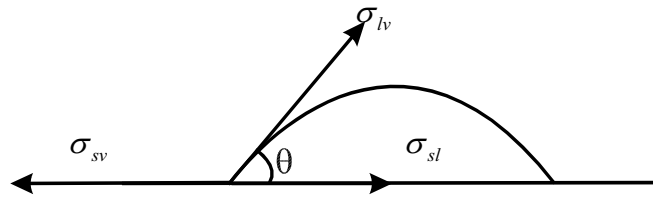


Figure 2.2. A liquid drop resting on a solid substrate, partial wetting.

The situation depicted in Fig. 2.2 is commonly called partial wetting since the surface of the substrate is partially covered with the liquid. The equilibrium shape of such a drop is determined by three forces acting at the contact line between the drop and the substrate [5]. These are the liquid-vapour interfacial tension σ_{lv} , the solid-vapour interfacial tension σ_{sv} and the solid-liquid interfacial tension σ_{sl} . They are connected mathematically via the Young's equation [39] as

$$\cos \theta = \frac{\sigma_{sv} - \sigma_{sl}}{\sigma_{lv}}. \quad (2.1)$$

where θ is the contact angle. Now if $\theta = 0$ the substrate is called completely wet. If $0 < \theta < \pi$ it is called non-wet and if $\theta = \pi$ it is dry. So wetting can be viewed as a direct

consequence of the Young's equation. If the liquid wets the substrate then a liquid layer of certain thickness is formed. The wetting (spreading) can be spontaneous e.g. a drop of water on a clean glass plate, or by tuning the thermodynamics of the system e.g. raising the temperature, changing the chemical composition [5]. Raising the temperature for example implies approaching the critical temperature along the liquid-vapour coexistence curve, which leads to a decrease in the interfacial tensions and as a consequence the contact angle will also change, knowing that the interfacial tension vanishes at the critical point. Such an approach was studied by Cahn [3]. He studied the asymptotic behaviour of the Young's equation approaching the liquid-vapour critical point (T_c) and predicted the necessity of a wetting transition near the critical point. The main point in his scenario is that approaching T_c along the liquid-vapour coexistence curve, both σ_{lv} and the difference $\sigma_{sv} - \sigma_{sl}$ follow scaling laws of the type: $\sigma_{lv} \propto |T - T_c|^\beta$ ($\beta < 1$), and $\sigma_{sv} - \sigma_{sl} \propto |T - T_c|^\mu$ ($\mu > 1$) [5]. As a consequence there exists a temperature $T_w < T_c$, where $\theta = 0$, thus a transition from partial to complete wetting occurs. Cahn called this temperature the wetting transition temperature (T_w). Numerous experiments have been performed on different systems to check the validity of Cahn's argument and indeed this type of critical point wetting was observed. Examples of this experimental work can be found in [5, 40].

2.2.2 First and second order wetting transitions

The nomenclature of different types of interfacial phase transitions follows that of bulk phase transitions. The latter are known to occur either as first or second order phase transitions. In bulk phase transitions like fusion and vaporization, discontinuous changes occur in the thermodynamic extensive quantities of the system like enthalpy, volume etc. [39]. Very similar changes of the thermodynamic surface quantities have to be considered driving an interfacial phase transition. It is mentioned above that if a liquid wets a substrate, then a layer of a certain thickness of the former is formed on top of the latter. The liquid layer thickness is proportional to the surface coverage (Γ) where the latter is given by Gibbs adsorption equation [40]:

$$d\sigma = -S^\sigma dT - \Gamma d\mu . \quad (2.2)$$

where σ is the surface energy, S^σ is the excess surface entropy and μ is the chemical potential. So a change in one parameter leads to a change in the other. If below T_w the

thickness l is microscopic and at T_w it jumps to an infinite (macroscopic) value, then from equ. (2.2) there is discontinuity in the first derivative of the surface free energy and the wetting transition is termed first order [5]. An example is given in Fig. 2.3 for the discontinuous changes of $\Gamma(l)$ from low to high adsorption at constant T .

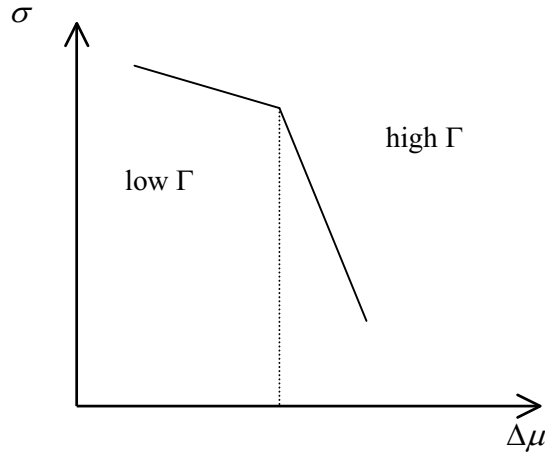


Figure 2.3. Surface energy σ vs chemical potential $\Delta\mu$ ($\Delta\mu = \mu - \mu_0$, μ_0 = chemical potential at coexistence for an one-component system) at constant T . Note that from equ. (2.2), $\Gamma = -(\partial\sigma / \partial\Delta\mu)_T$.

A first order wetting transition of this type was experimentally observed in different systems (solid-gas, solid-liquid and liquid-liquid) mainly characterised by Van der Waals interactions. Examples and a detailed discussion of different systems can be found in [5]. In case of a binary liquid mixture with a miscibility gap the first order wetting transition involves a prewetting line extending from T_w to the prewetting critical point [40]. The latter will be dealt with in a subsequent section. If the thickness of the wetting film grows continuously with temperature, the first derivative of the surface free energy is defined at T_w and the transition is called a second order wetting transition or critical wetting.

2.2.3 Why is wetting a phase transition?

It is relevant at this stage to address and answer the above question clearly but shortly. From what is mentioned above concerning bulk phase transitions, the bulk entropy changes discontinuously at the transition temperature T_t . Analogous to this, if the

thickness and thus the surface excess density (surface coverage) of a liquid film on a substrate (note that the substrate can be a liquid or a solid) becomes singular at the wetting temperature T_w , then the surface excess entropy will also become singular (see equ. 2.2). So the surface coverage is the order parameter of a surface wetting transition. In addition to surface excess entropy being singular the surface free energy will also become singular at the transition. The transition from one phase to the other is defined by these singularities. Therefore wetting is a phase transition [40].

2.2.4 Wetting transitions in binary liquid mixtures

Having defined an interfacial wetting transition and the different types in which it may occur from a general perspective, we will now introduce a particular case in which a liquid is wetted by another liquid in binary liquid mixtures. Solid substrates involve surface irregularities which complicate the spreading of liquid drops and the subsequent calculations of the thermodynamics of the system [5]. In addition, a solid substrate is supposed to be inert against a wetting liquid. The latter would imply a negative spreading coefficient $\chi \equiv \sigma_{sv} - \sigma_{sl} - \sigma_{lv} \leq 0$. However, this is not always the case and a positive spreading coefficient was experimentally observed. These complications are missing in case of interfacial wetting of a liquid by another liquid (binary liquid mixtures). A detailed study of this issue can be found elsewhere [41]. From Cahn's general argument it is assumed that in any three-phase system (the third component can be a solid substrate or vapour) and for temperatures close to the critical point, where two of the three phases become indistinguishable, complete wetting should occur.

In a binary liquid mixture the critical point is the consolute point where the two liquids become miscible [42]. We consider a temperature-composition phase diagram of a binary liquid mixture α - β (α = A-rich and β = B-rich) having an upper consolute point of mixing as shown below in Fig. 2.4(a) [7]. The parabolic curve, represented by the bold solid line in Fig. 2.4(a), is a typical demixing curve or a bulk coexistence line of the α - β system. A two-phase coexistence implies two minima in the Helmholtz free energy F at the respective compositions (x_α and x_β) of the two phases as shown below in Fig. 2.4(b) [42].

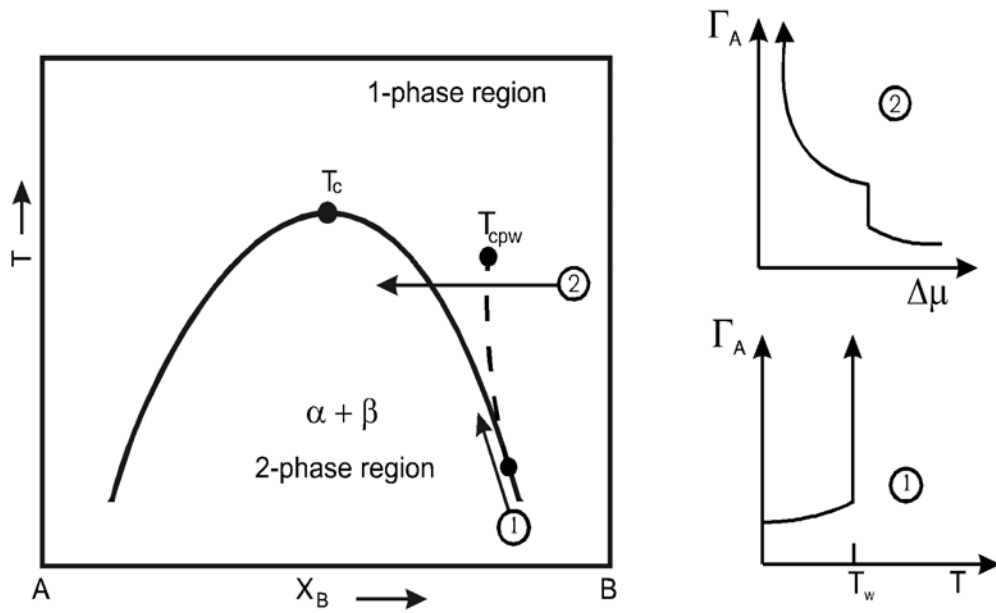


Figure 2.4(a). A temperature-mole fraction bulk phase diagram of a binary liquid mixture with a miscibility gap represented by the bold solid line. T_c is an upper bulk critical point at which demixing terminates. Included in the figure is the surface phase diagram with a wetting transition at coexistence at T_w and prewetting transitions from low to high adsorption along the prewetting line (bold dashed line). Changes in the surface excess density Γ along path (1) and (2) are discussed in the text.

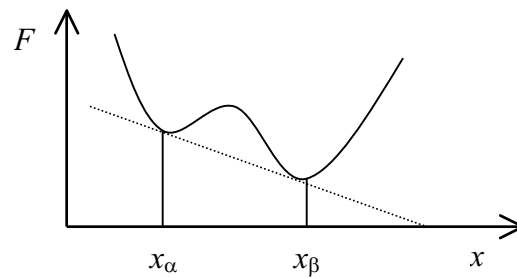


Figure 2.4(b). Helmholtz free energy $F = U - TS$ as a function of the mole fraction x at two-phase coexistence, where U is the internal energy, T is temperature and S is the entropy.

The existence of a surface on the other hand implies that there is a transition region where the density changes from one bulk value to the other. In the inhomogeneous transition region (2-phase region in Fig. 2.4(a)) the local free energy will be higher than in either of the bulk phases. Since this work is concerned with wetting transitions in binary liquid alloys, namely Ga-Bi and Ga-Pb liquid alloys, β may represent the

less dense, high surface energy component Ga, and α may represent either of the more dense, low surface energy components Bi or Pb.

We go back to Cahn's argument, which was already mentioned above. At a temperature $T_w < T_c$ a transition from partial to complete wetting occurs in the α - β system, and the β -vapour interface is replaced by the α -vapour interface. In other words the more dense, low surface energy component has segregated at the intrinsic β -vapour interface. Fig. 2.5 shows a schematic drawing of the transition from partial to complete wetting in a binary liquid mixture [42].

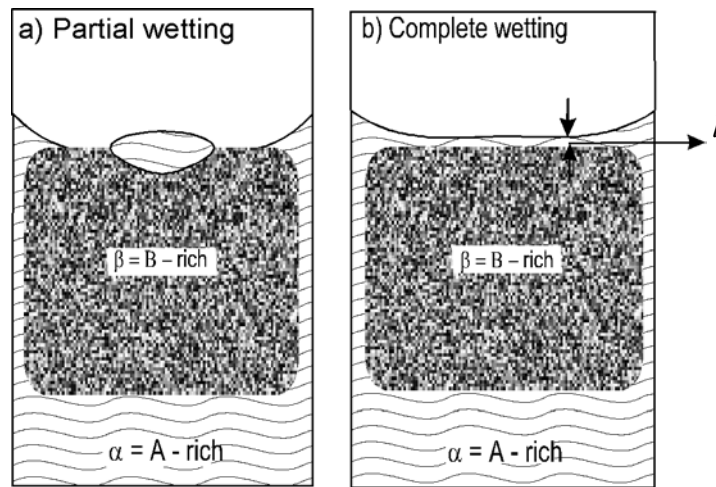


Figure 2.5. Wetting in the α - β binary liquid mixture: (a) partial-wetting state; (b) complete wetting state.

Fig. 2.5 represents a general case of a wetting transition in a binary liquid mixture. In the Ga-Bi and Ga-Pb liquid alloys, case (b) of Fig. 2.5 has been experimentally confirmed [43]. The partial wetting state depicted in part (a), where a drop of the segregated component forms at the β -vapour interface making a finite contact angle, has been observed in binary liquid mixtures [42]. The segregation of α occurs even when β has a lower density than α . Thus, interfacial wetting transition at the intrinsic β -vapour interface is an energetically driven phenomenon and gravity has little influence on it. However gravity plays a role in limiting the thickness l (Fig. 2.5(a)) of the intruding α -film and drives the wetting film slightly off coexistence [5]. This type of interfacial wetting occurs along the coexistence curve or off coexistence (in the one-phase region, see Fig. 2.4(a)) [42]. The former is the case when varying the

temperature at coexistence and the latter when varying the composition or chemical potential at constant temperature off coexistence.

The wetting transition off coexistence is the persistence of the transition in the one-phase region and is called prewetting transition [42]. The loci of this transition are represented by a line (dashed line in Fig. 2.4(a)) leaving the parabolic curve tangentially at the wetting transition point T_w and extending to the surface critical point T_{Cpw} (see Fig. 2.4(a)). This line is called a prewetting line [42]. As mentioned briefly in section 2.2.2, a first order surface phase transition involves a prewetting transition which represents a thin to thick transition in the thickness of the intruding layer (l) implying an abrupt change in adsorption at the interfacial region (Γ) or simply a low to high adsorption transition. In Fig. 2.4(a), a first order transition occurs along path (1) if Γ is finite for $T < T_w$ and diverges at T_w , and the Γ_A (note that for a two-component system Γ has to be replaced by the relative surface excess density $\Gamma_A(T, \mu_A)$ with a proper choice of Gibbs' dividing surface) versus T diagram of Fig. 2.4(a) shows the divergence of Γ_A ($l \propto \Gamma$) at T_w . On the other hand, a second order or critical wetting transition implies that at coexistence along path (1) Γ increases continuously for $T < T_w$ and diverges at T_w . Following path (2) from the B-rich end of the phase diagram, Γ exhibits two characteristic changes. On crossing the prewetting line Γ jumps from low to higher adsorption states, but the jump is a microscopic change. Approaching the coexistence curve it increases continuously and diverges at coexistence. This is denoted a complete wetting transition (pictured in Fig. 2.5(b)) and the Γ_A versus $\Delta\mu$ diagram in part (a) of Fig. 2.4 shows the changes of Γ_A along path (2). It is worth mentioning here that wetting transitions and prewetting phenomena generally prevail only in binary systems with a liquid miscibility gap [42].

The first experimental confirmation of the existence of a prewetting transition in a binary liquid mixture was made by Kellay *et al* (1993) using the dielectric methanol-cyclohexane system [42], while the existence of a prewetting line was experimentally observed by Rutledge and Taborék (1992) [42] for the first time in liquid He. Later wetting transitions and the subsequent characteristics were observed in other non-metal systems [42]. In case of binary liquid metals (alloys) wetting transition was first evidenced by Nattland *et al* (1996) in a Ga-Bi liquid alloy [43] and by Chatain *et al* (1996) in the Ga-Pb system [13].

2.3 Capillary waves at liquid surfaces and interfaces

2.3.1 Physical origin of capillary waves

Molecules or atoms at a two-fluid interface differ from their counterparts in the bulk of the fluid in that they miss their same neighbours at the other side of the interface [5]. As a consequence these molecules or atoms will have excess energy and an increased mean square vertical displacement in comparison to their counterparts in the bulk of the liquid. These thermally driven molecular scale displacements appear as propagating waves at the interface. Fig. 2.6 depicts such a surface mode and its Fourier component.

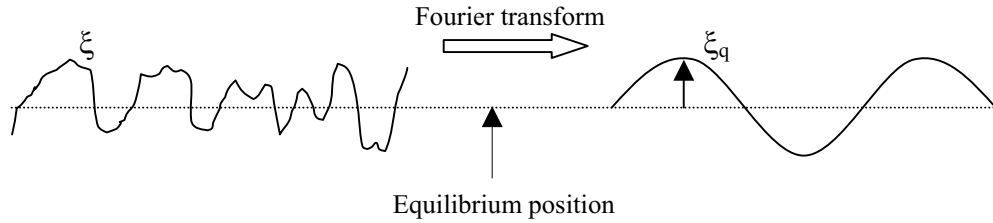


Figure 2.6. A surface mode and its Fourier component.

The surface tension of the liquid acts as a restoring force, similar to that of a harmonic oscillator [44]. That is why these surface waves are called capillary waves (CW), riplons or even surfons. When a surface wave moves across the liquid surface it will be damped by the liquid viscosity. Generally speaking, the propagation of waves at liquid surfaces and interfaces are governed by both bulk and surface properties. The mean square displacement per unit area of surface due to thermal motion is given by [44]:

$$\langle \xi_q^2 \rangle = \frac{k_B T}{\sigma q^2 + \rho g} \quad (2.3)$$

where k_B is the Boltzmann constant, σ is the surface tension of the liquid, ρ is its density, q is the wave vector, g is the gravity acceleration and T is the temperature. The gravity force comes into play at long wave lengths and has a negligible effect on the short wave lengths capillary waves $30 < \lambda_q < 300 \mu\text{m}$ [44]. The period of these surface modes is in the range of $1\mu\text{s} - 1\text{s}$ and their amplitudes range from $1-10^3 \text{ \AA}$ depending on the surface tension of the liquid as it is clear from equ. (2.3) [45]. The

ratio $y = \frac{\sigma\rho}{4\eta^2q}$ of the restoring forces to the viscous forces determines the propagation regimes of capillary waves. They are propagating if $y \gg 1$, and overdamped if $y \ll 1$. If $y \sim 1$ the situation is called critical damping [44].

2.3.2 Dispersion equation of capillary waves at a free liquid surface

Levich [46] and Lamb [47] have separately studied the dispersion behaviour of capillary waves, $\omega(q)$, on a free liquid surface. Solving the hydrodynamic linearized Navier-Stokes equation with the boundary conditions of normal and tangential stress being the same on both sides of the interface, in first approximation they obtained the dispersion equation which relates the propagation characteristics of the surface modes to the constitutive parameters of the system as [44]:

$$\left(i\omega + \frac{2\eta q^2}{\rho} \right)^2 + \frac{\sigma q^3}{\rho} = \frac{4\eta^2 q^4}{\rho^2} m_1. \quad (2.4)$$

Here σ is the surface tension, η is the viscosity, ρ is the density of the liquid, q is the wave vector, $m_1 = \sqrt{1 + \frac{i\omega\rho}{\eta q^2}}$ ($\text{Re}(m_1) > 0$) and $\omega = \omega_0 + i\kappa$ is the complex frequency, ω_0 and κ are the frequency and the temporal damping coefficient of the wave. To first order approximation the roots of equ. (2.4) are:

$$\omega = \omega_0 + i\kappa, \quad (2.5)$$

with:

$$\omega_0 = \sqrt{\frac{\sigma q^3}{\rho}} \quad \text{and} \quad \kappa = \frac{2\eta q^2}{\rho}. \quad (2.6)$$

Both ω_0 and κ are increasing functions of the wave vector $q = 2\pi/\lambda_q$. m given above can be interpreted as the inverse capillary penetration length, which gives a measure of the damping of the surface velocity field in the liquid [48]. By a free liquid surface it is meant that the liquid surface is free of adsorbed film (monolayer) or a surface freezing film. In case of the presence of a film the dispersion equation given above is not valid and a modification is needed.

2.3.3 Modification of the dispersion equation

When a monolayer or thin surface freezing film is present at a two-fluid interface, it exerts a resistance against various types of surface deformation [44, 49]. This was inferred from a notable increase in damping of capillary waves at the water surface in the presence of a molecular film. The increase in damping was interpreted in terms of a cohesive resistance to the extension of the film induced by surface deformation [50]. Further realization by Lucassen led to the conclusion that capillary waves are coupled to compressional surface waves sustained by compressional surface elasticity [50]. The effect as such is a resonance between the two modes occurring when their frequencies coincide [51]. This concept was treated by Kramer [52] who derived the dispersion equation of capillary-compressional waves at a liquid-film interface as

$$D(\omega) = \left\{ \frac{\varepsilon q^2}{\omega} + i\eta(q + m_2) \right\} \left\{ \frac{\gamma q^2}{\omega} - \frac{\omega\rho}{q} + i\eta(q + m_2) \right\} + [\eta(q - m_2)]^2 = 0. \quad (2.7)$$

with $m_2 = qm_1$; $\text{Re}(m_2) > 0$, ω , ρ , η , q , m_1 , were defined above in equ. (2.4).

The first term in equ. (2.7) refers to compressional surface waves, the second is for capillary waves and the last term is the squared coupling constant. Viscoelasticity of the surface film is captured in γ and ε , which are the transverse shear and compressional modulus, respectively [52]. Within the film there is viscous dissipation. This can be incorporated by expanding ε and γ as linear response functions [44]:

$$\begin{aligned} \gamma &= \bar{\gamma}_s + i\omega\bar{\eta}_t, \\ \varepsilon &= \varepsilon_0 + i\omega\varepsilon'. \end{aligned} \quad (2.8)$$

where $\bar{\gamma}_s$ is the surface excess elastic modulus, $\bar{\eta}_t$ is the surface excess shear viscosity, ε_0 is the compressional elastic modulus and ε' is the viscous part of ε . Neither $\bar{\eta}_t$ nor ε' are the conventional surface viscosity due to shear within the surface plane [51]. ε simply measures the resistance against any changes in area of a surface element, while γ measures the resistance against any changes in shape of the element [50]. A complete interpretation of the physical meaning of these surface viscosities can be found in [44]. Due to its complexity equ. (2.7) can only be solved numerically.

Another approach to surface viscoelasticity due to a structured surface and its influence on the propagation of surface waves was made by Tejero and Baus [53]. In their treatment the high frequency elastic, the low frequency hydrodynamic and the intermediate viscoelastic regimes are investigated separately. The outcome of their

study in the hydrodynamic regime (CW) is simply a modification of the roots (equ. 2.4) of the dispersion equation of capillary waves at a free liquid surface. Based on this and restricting the viscoelastic behaviour to the surface layer alone their results in the weakly damped domain reduce to making the simple substitutions in equ. (2.4) [51]:

$$\sigma_0 \rightarrow \sigma + \bar{\gamma}_s + i\omega\bar{\eta}_t, \quad (2.9)$$

where σ is the thermodynamic equilibrium surface tension. In first order equ. (2.4) becomes:

$$\omega = \sqrt{\frac{\sigma q^3}{\rho} + \frac{\bar{\gamma}_s q^3}{\rho}},$$

$$\kappa = \frac{2\eta q^2}{\rho} + \frac{\bar{\eta}_t q^3}{2\rho}. \quad (2.10)$$

It has been pointed out by Tejero and Baus that direct access to the liquid surface structure is attainable from experimental observations of the surface waves. In this work and when we come to our study on surface freezing in the binary liquid alloys Ga-Bi and Ga-Pb, we will focus on the capillary waves regime making use of the results of Tejero *et al.* (equ. 2.10).

2.3.4 Scattering of light by capillary waves

Electromagnetic theory pictures radiation as a sinusoidally varying electromagnetic field. When this field interacts with the constituents of matter (molecules or atoms) it will produce a sinusoidal oscillation of the electrons within the matter. Such oscillating charges will cause the constituents of matter to disperse some energy in directions other than the direction of the incident radiation. This is the core idea of light scattering [54-55].

Smoluchowski predicted the scattering of light from a thermally roughened surface in 1908 [56]. Five years later this prediction was checked by Mandelstam who noted some scattered light from a critical mixture of CS₂-(CH₃OH). This scattered light was not greatly removed from that of regular reflection which was one of the difficulties involved in surface light scattering studies. These observations opened the door to a new field, that of studying liquid surfaces by light scattering. Since then many developments have been made in the field both theoretically and experimentally especially after the invention of lasers in 1960. The difficulty of having a good

resolution of the scattered light from the reflected one stayed until 1976 when Hård *et al* [57] introduced a diffraction grating as a local oscillator. After this latter major development the technique was recognized as a good probe for liquid surfaces and the number of experiments was increased substantially. However, the technique involves some other difficulties which we will come to later in the experimental part.

Thermally excited capillary waves produce refractive index fluctuations [44], therefore when light impinges on a liquid surface some of it will be scattered while the major portion will be regularly reflected. The scattered light intensity caused by refractive index fluctuations is proportional to the capillary waves properties. The latter is connected to the liquid properties (e.g. surface tension and viscosity) via the dispersion equation (equ. 2.4).

Each surface mode (CW) and its Fourier component behaves like a moving diffraction grating and scatters light quasi-elastically in a sense that it changes its frequency by the Doppler effect [45].

We consider an incident beam of monochromatic light on a liquid surface as shown below:

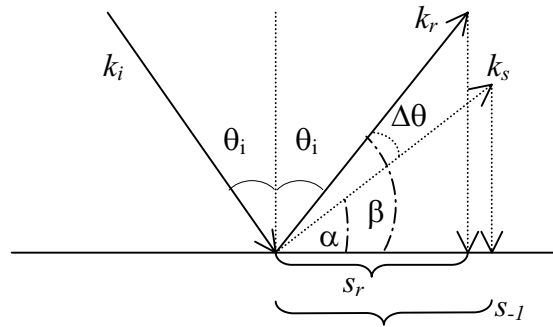


Figure 2.7. Geometry of light scattering from a liquid surface.

where k_i , k_r and k_s are the incident, reflected and scattered wave vectors. θ_i and $\Delta\theta$ are the incidence and the scattering angles, respectively. s_{-1} and s_r are the projections of k_s and k_r on the surface plane. Then by momentum conservation at the surface plane, the capillary wave vector q is defined as [44]:

$$q = s_{-1} - s_r = k_s \cos \alpha - k_r \cos \beta ,$$

with

$$k_s = k_r = \frac{2\pi}{\lambda_l} , \quad (2.11)$$

and for $\Delta\theta \ll \pi/2$, the wave vector q becomes:

$$q = \frac{2\pi}{\lambda_l} \Delta\theta \cos\theta_i . \quad (2.12)$$

Different values of q imply that each surface wave corresponds to a different scattering vector k_s . If ω_i is the frequency of the incident beam and ω_0 is the frequency of capillary wave then from energy conservation the frequency of the scattered light is

$$\omega_s = \omega_i \pm \omega_0 . \quad (2.13)$$

Since ω_i is $\sim 10^{15} \text{ s}^{-1}$ and $\omega_0 \sim 10^3\text{-}10^5 \text{ s}^{-1}$, it is difficult to resolve such a low frequency change from the huge frequency of the reflected beam. This problem can be tackled by a technique called heterodyne or light beating [45].

2.3.5 The necessity of heterodyne technique for the detection of light scattered by CW

The diffraction grating (DG) mentioned above is a major component in surface light scattering. It is made by deposition of a metal (e.g. Cr, FeO) on a glass plate and etching of the grating [58]. It splits the incoming beam into a main beam and diffracted ones:

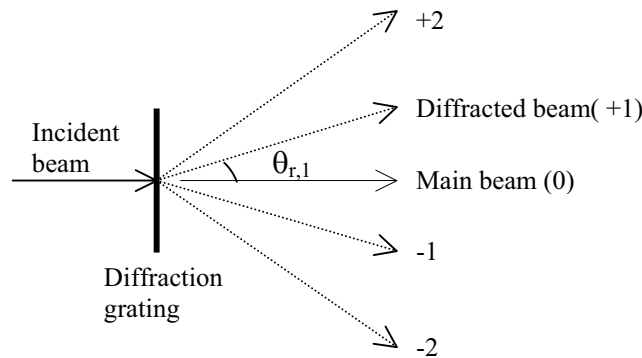


Figure 2.8. Splitting of an incident beam into main beam and diffracted ones.

The splitting mechanism as such is based on the constructive-destructive interference of the grating [59]. Thus, the diffraction grating provides well defined diffracted beams having the same ω as that of the incident beam and having different

diffraction angles θ_r with respect to the main beam e.g. $\theta_{r+3} = \frac{3}{2}\theta_{r+2} = 3\theta_{r+1}$, where the same applies to $-1, -2, \dots$ (see Fig. 2.8).

If this diffracted pattern is imaged on the liquid surface, each order (spot) and thus each θ_r will correspond to a different capillary wave number q on the surface i.e:

$$\lambda_q = \frac{\lambda_i}{\Delta\theta \cos\theta_i}; \text{ where } \lambda_i \text{ is the wavelength of the incident light and } \Delta\theta \cong \theta_r \text{ if the}$$

surface is flat. Thus, each scattered spot carries two frequency components $\omega_i \pm \omega_0$. In other words, the scattered light (shifted in frequency by a CW) is mixed with a reference, unshifted, coherent, regularly reflected light. This is called heterodyne mixing. This all is provided by the diffraction grating. If this mixed laser beam is sent to a detector (Photomultiplier, PMT) then the subsequent intensity variation will be modulated by a beat phenomenon [45]. The beat frequency is just the frequency difference between the shifted and unshifted laser light. The magnitude of the beat frequency is within the response of the PMT.

If \vec{E}_i and \vec{E}_s correspond to the incident and scattered electric fields, then for scattering from a single surface mode (CW) in one scattering direction:

$$\begin{aligned} \vec{E}_i &= \vec{E}_{0i} \exp(i(\vec{k}_i \vec{r} - \omega_i t)) \text{ and} \\ \vec{E}_s &= \vec{E}_{0s} \exp(i(\vec{k}_s \vec{r} - \omega_s t)), \end{aligned} \quad (2.14)$$

where \vec{E}_{0i} is the amplitude of the incident field, \vec{E}_{0s} is that of the scattered field, \vec{k}_i and \vec{k}_s are the wave vectors of the incident and the scattered fields, respectively, and \vec{r} is the propagation vector.

The PMT detection depends on the total electric field \vec{E}_{tot} at individual points on the photocathode. The spatial dependence of the field may be neglected since light cannot beat at two different points [45]. If we consider only the real parts of the field, then equ. (2.14) becomes at constant \vec{r} :

$$\vec{E}_{tot} = \vec{E}_{0i} \cos \omega_i t + \vec{E}_{0s} \cos \omega_s t, \quad (2.15)$$

and the intensity variation of the mixed fields will be

$$I_{tot} = \vec{E}_{tot}^2 = \vec{E}_{0i}^2 \cos^2 \omega_i t + \vec{E}_{0s}^2 \cos^2 \omega_s t + \vec{E}_{0i} \vec{E}_{0s} (\cos(\omega_s - \omega_i)t + \cos(\omega_s + \omega_i)t), \quad (2.16)$$

The term with $\omega_s + \omega_i$ will be averaged by the PMT due to its limited response. Since $\omega_s = \omega_i \pm \omega_0$ then

$$\begin{aligned}\cos(\omega_s - \omega_i) &= \cos(\omega_0) \text{ and} \\ \cos(\omega_s + \omega_i) &= \cos(2\omega_i \pm \omega_0),\end{aligned}\quad (2.17)$$

The latter term will be zero by cycle-averaging and equ. (2.16) reduces to:

$$I_{tot} = \frac{1}{2} \bar{E}_{0i}^2 + \frac{1}{2} \bar{E}_{0s}^2 + \langle \bar{E}_{0i} \bar{E}_{0s} \cos(\omega_s - \omega_i) t \rangle, \quad (2.18)$$

The last term in equ. (2.18) is the beating term. The intensity-intensity correlation function is given by

$$G(\tau) = \langle I_{tot}(t) I_{tot}(t + \tau) \rangle = (I_s + I_r)^2 + 2I_s I_r g^{(1)}(\tau) + I_s^2 [g^{(2)}(\tau) - 1], \quad (2.19)$$

where

$$g^{(1)}(\tau) = \frac{\langle E_s(t) E_s(t + \tau) \rangle}{I}, \quad (2.20)$$

is the scattered light normalized first order field autocorrelation function, and

$$g^{(2)}(\tau) = \frac{\langle I_s(t) I_s(t + \tau) \rangle}{I^2}. \quad (2.21)$$

is the second order intensity autocorrelation function. Since $I_r \gg I_s$, $I_s/I_r \sim 10^{-3}$ [45], where I_r and I_s are the intensities of the reference and the scattered light, respectively, the last term in equ. (2.19) is negligible.

2.3.6 The spectrum of the scattered light and its relation to the power spectrum of CW

Thermal fluctuation of a liquid surface from its equilibrium position caused by a disturbance of wave number q and amplitude ξ_q and propagating in the x direction is given by:

$$\xi_q(t, x) = \xi_q(0) \exp(i(qx + \omega t)), \quad (2.22)$$

where $\xi_q(0)$ is the amplitude at time = 0, $\omega = \omega_0 + i\kappa$ is the complex frequency of a CW, with ω_0 and κ as defined above. The amplitude-amplitude correlation function is

$$G_q(\tau) \equiv \langle \xi_q(t) \xi_q(t + \tau) \rangle = |\xi_q(0)|^2 \exp(-\kappa\tau) \exp(i\omega_0\tau) \propto \exp(-\kappa\tau) \cos \omega_0\tau, \quad (2.23)$$

where $\kappa = 1/\tau_0$ and τ_0 is the relaxation time associated with a surface displacement. The full derivation of $G_q(\tau)$ can be found in [44]. $\xi_q(0)$ is given by equ. (2.3). The power spectrum which describes the temporal evolution of capillary waves is the Fourier transform of $G_q(\tau)$ according to the Wiener-Khinchine theorem [55]:

$$P_q(\omega) = \frac{\xi_q^2(0)}{2\pi} \int_{-\infty}^{+\infty} \exp(i\omega\tau) G_q(\tau) d\tau = \frac{\xi_q^2(0)\kappa}{\pi((\omega - \omega_0)^2 + \kappa^2)}, \quad (2.24)$$

and according to equ. (2.23) is a Lorentzian. In surface light scattering the PMT signal (the PMT output current) is amplified and analysed either with a correlator that measures $G(\tau)$, equ. (2.19), directly or a spectrum analyser that measures its Fourier transform:

$$P(\omega) = \int_{-\infty}^{+\infty} \langle I(t)I(t+\tau) \rangle \exp(i\omega\tau) d\tau \propto P(q, \omega). \quad (2.25)$$

Thus the spectrum of the scattered light (power spectrum of the photocurrent) is just the power spectrum of capillary waves.

The spectrum in equ. (2.24) is a simple Lorentzian centred at $\omega = \omega_0$ with a half width κ . Deviations from this simple form have been experimentally found in the strongly damped regime ($y \sim 1$) of capillary wave propagation. This deviation was attributed to the surface-bulk coupling [44]. For large values of y (in the weakly damped regime) the experimental spectrum can be safely approximated by a Lorentzian shape provided that instrumental broadening corrections have been taken into account [44]. In practice, there is extra broadening in the experimental spectra due to finite instrumental resolution (finite size of the laser beam). Therefore one does not obtain a spectrum of light scattered by a single surface mode of wave number q but rather from a range in $q \pm \Delta q$ [44]. If the beam profile is Gaussian, which is the case for TEM₀₀ laser beam mode, then [51]:

$$\Delta q = \frac{4 \cos \theta_i}{D} 2\sqrt{2}, \quad (2.26)$$

where θ_i is the incident angle, D is the diameter of the laser beam taken at an intensity reduction by $\frac{1}{e^2}$ points of the beam profile. This corresponds to a standard deviation in frequency of:

$$\beta = \Delta q \frac{d\omega_0}{dq}. \quad (2.27)$$

This in turn can be evaluated *ab initio* using equ. (2.6) if σ is known. This procedure is applicable to simple liquids with known surface tensions. In our case the surface tension is treated as an unknown parameter. Therefore it is highly appreciable to extract β from the fit of the experimental spectra. The latter could have contributions due to mechanical vibrations or acoustical disturbances which would have effects on β . The point here is to include β in the theoretical spectrum. This is done by writing the spectrum in a form of convolution between a simple Lorentzian shape and a Gaussian beam profile having β as the standard deviation [57-58, 60]:

$$P(\omega) = \int_{-\infty}^{+\infty} \frac{\kappa / \beta \exp[-(\omega - \omega')^2 / \beta]}{(\omega' - \omega_0)^2 + \kappa^2} d\omega', \quad (2.28)$$

This integral can be evaluated in terms of a complementary error function of the complex argument:

$$P(\omega) = A \operatorname{Re} \left\{ \exp \left[- \left(\frac{i\kappa}{\beta} + \left(\frac{\omega - \omega_0}{\beta} \right) \right)^2 \right] \right\} \operatorname{erfc} \left[\frac{\kappa}{\beta} + \left(\frac{\omega - \omega_0}{\beta} \right) \right] + B. \quad (2.29)$$

Note that $\operatorname{erfc}(x) = 1 - \operatorname{erf}(x)$.

In equ. (2.29) A is an amplitude, B denotes a background contribution. It is this spectrum that will be used in this work to fit the experimental spectra to get the parameters in question: $(\omega_0, \kappa, \beta)$.

Chapter 3

Experiment

3.1 Experimental set-up for surface light scattering

The optical components of our surface light scattering spectrometer are comparable to those that exist in the literature, see e.g. [44]. The major set-up is as shown below:

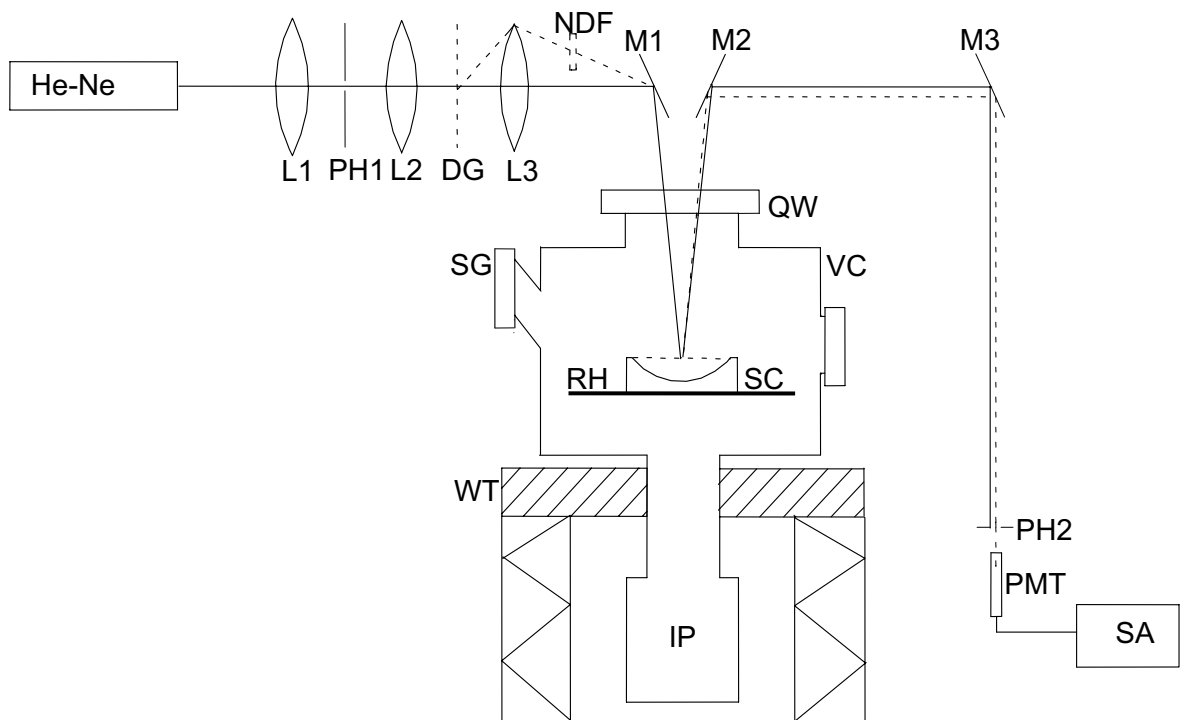


Figure 3.1. A schematic representation of our experimental set-up.

- He-Ne laser source (163 Baypointe Pkwy, Uniphase) with an output power of 7 mW. The wavelength of the laser beam is $\lambda_l = 633\text{nm}$ operating in the TEM_{00}
- L1 and L2: planeconvex lens
- P1: pinhole of $80\ \mu\text{m}$ diameter
- DG: diffraction grating
- L3: achromatic lens
- NDF: neutral density filter

- M1-3: elliptical mirrors with R-AL coating on SiO₂
- P2: pinhole with 0.9 mm diameter
- PMT: photomultiplier tube (C1053-01, Hamamatsu)
- SA: Fast Fourier transform spectrum analyzer model SR760 (Stanford research system).

All optical components are mounted on translational stages to allow good positioning and control. The L1 + PH1 combination serves as a spatial filter to get rid of the stray light from the laser beam. The neutral density filter is used to control the ratio $I_s/I_r \cong 10^{-3}$ by reducing the intensity of the reference beam I_r as the intensity of the scattered beam falls with the wave number, $I_s \sim q^{-2}$ [44]. As already described in chapter 2, the diffraction grating is the main element of heterodyne technique. L3 is used to image the grating on the liquid surface. It has a diameter of 6 cm, large enough to allow the passage of the higher orders diffracted from the grating. In this work, however, we only use the first three orders, so the lens coma or aberration which was reported in [61] at higher orders is irrelevant here. Pinhole 2 has 0.9 mm diameter to select only one order at the PMT.

The sample cell design is made suitable for studying liquid metals and alloys. It consists of a weldable high quality stainless steel vacuum chamber (VC) with a quartz window (QW) for optical passage, and has two side flanges with large diameter: one where a liquid nitrogen trap is installed, the other is used for sample introduction. The latter has a resistance furnace for heating (RH), a cooling plate and a manipulator attached to it. An Argon ion sputter gun (SG) (PU-IQE 11/35, SPECS) was installed for sample cleaning. The pumping system consists of a mechanical pump, a turbo pump and a 60 L/s ion pump (IP) (HV-Diode, RVA-60, DD/O, Omicron-Instruments). The former two serve as a prepumping system.

All components are mounted on a heavy vibration-isolated table (WT) (Melles Griot) with air pressurized cylindrical legs to remove adventitious high frequency vibrations.

3.2 Materials and sample preparation

Molybdenum is chemically inert against Gallium and Bismuth, also at elevated temperatures. Two molybdenum crucibles of different dimensions were used as sample reservoirs. One is 47 mm in inside diameter and has a flat bottom surface that has been used for preparation of pure components plus one alloy sample (81.18 at %

Bi). The other one is hemispherical in shape with 42 mm in diameter and 7.4 mm in depth, and is used for the rest of the sample alloys. With the hemispherical crucible a flat interface is obtained.

First, two separate measurements were carried out to check the difference in temperature between the resistance furnace (see Fig. 3.2) and the two crucibles mentioned above. The difference in temperature was recorded 40 minutes after the desired temperature at the furnace was reached. For these experiments, both the furnace and the crucible have to be machined in such a way that they are in optimum contact. If they are not flat and polished at the bottom heat transfer from the furnace to the crucible will not be optimised and the difference in temperature between them is high. Details on the thermocouple used in these measurements will be given later on. Fig. 3.2 shows results of these calibration experiments.

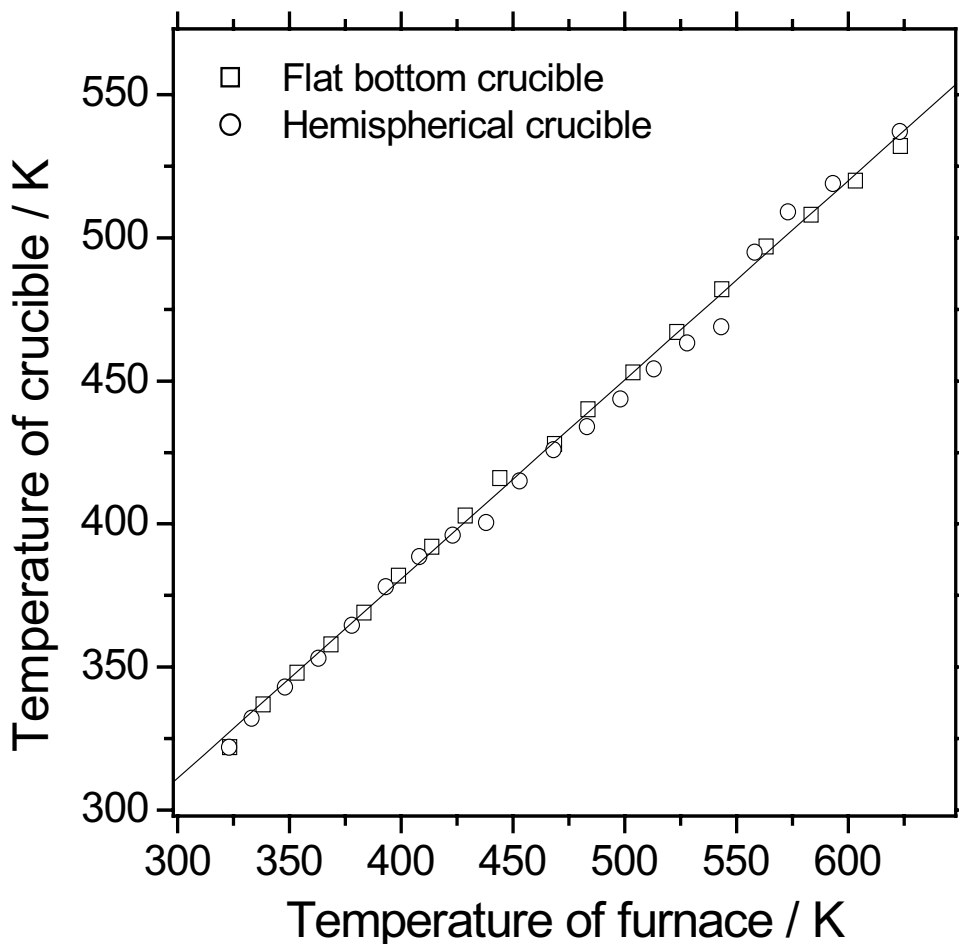


Figure 3.2. Difference in temperature between the furnace and the sample crucibles. Flat bottom (□), hemispherical (○), solid line is a linear fit.

As can be seen in Fig. 3.2 both crucibles show almost the same difference in temperature with respect to the furnace, all experimental points lie on the same line. These calibrations are important for later temperature control.

3.2.1 Preparation of the pure liquid Gallium sample

A prerequisite for surface light scattering measurement is a flat liquid surface. This is one of the main difficulties involved in this technique especially when working with liquid metals and alloys. Due to high surface energy of Ga (melting point $T_m = 302.77$ K) and the difficulty of obtaining an absolutely clean sample container, pure Ga does not spread easily on a molybdenum crucible heated under vacuum. In order to achieve wetting near room temperature between Ga and the Mo crucible, we have used a glow discharge technique in Argon atmosphere as described by Regan et al [36]. The Mo crucible was first cleaned mechanically and hanged in a quartz tube equipped with a high vacuum valve. It was then heated in an induction furnace at 1673 K under a residual pressure of $< 1 \times 10^{-5}$ mbar. After allowing it to cool down to room temperature it was transferred under Ar to a vacuum chamber especially designed for glow discharge. The chamber was mounted on a movable table for mechanical shaking. 30 g of pure Ga splatters of 2-4 mm in size (99.99999 % purity, from Alfa Chemicals) were placed in a glass syringe and hanged above the cleaned weighed crucible inside the vacuum chamber. After evacuating the chamber using a turbo pump for two days, a pressure of 10^{-6} mbar was achieved. The chamber was heated to 333 K and left overnight to drop Ga into the sample crucible. It was cooled to room temperature and filled with Ar. Upon Ar filling the pressure increased from 10^{-6} mbar to the desired pressure of 10^{-2} mbar of Argon. A voltage of about 4 kV was applied between the substrate and a needle-shaped electrode spaced 5 cm apart. After some time the anode-cathode voltage dropped to 1kV and the current rose to 1mA. Immediately hereafter the sample was gently shaken to spread Ga. In this way a nicely wetted layer of Ga with a flat surface was obtained. The layer thickness was about 2-2.5 mm. The sample was left to solidify and then transferred to another UHV chamber mounted on the light scattering table. The latter chamber was evacuated for a week using a turbo pump. During this evacuating procedure it was also baked at 333 K from time to time in order not to melt the Ga. The trap in the chamber was filled with liquid nitrogen and a pressure of 10^{-7} mbar was achieved. The temperature of the sample was

measured with a Ni-NiCr thermocouple inserted inside a hole made 1 mm above the bottom of the crucible. The thermocouple was calibrated by measuring the melting point of Ga. The absolute accuracy of the temperature measurements was found to be ± 1 K. After melting, thin oxide islands were present on the Ga surface. The latter were sputtered with an Ar ion gun having beam energy of 2 keV at 10^{-5} mbar for 15-20 min. Most of these oxide islands were removed completely while the remaining oxide stuck to the crucible edge. The laser beam was focused on the middle of the sample surface. It was completely invisible indicating a free oxide area on the surface. At this stage no surface energy measurements were done. This procedure was carried out only to clean the sample surface. Better judgment about the cleanness of the surface was made with help of the laser beam. The sample was then solidified and left overnight.

3.2.2 Preparation of the liquid Ga-Bi and Ga-Pb sample alloys

All sample alloys were prepared in Ar atmosphere inside a glove box ($O_2 < 1$ ppm, $H_2O < 1$ ppm). The preparation of low concentration Bi alloys < 1 at % was done as follows: First, 70 g of pure Bi (99.9999% purity, from Strem Chemicals, $T_m = 544.4$ K) were distilled in the induction furnace from a glass syringe placed 6 cm above the crucible to ensure that the latter remained cooled and the dropped Bi would not stick to it. The dropped Bi was allowed to solidify. It was then easily removed from the crucible and cut into pieces for sample alloys preparation.

Also here we had to achieve wetting between the sample alloys and the Mo crucible. For this purpose a thin film of pure Bi was deposited on the surface of the hemispherical crucible. A special double crucible holder was made from copper, which fits in the quartz tube. 20 g of distilled Bi were added in the glove box to the flat bottom crucible which was later fixed in the lower part of the crucible holder. The empty weighed hemispherical crucible (cleaned as mentioned before) was placed 7 cm above it in the upper part of the holder to ensure that it remained cooled. Fig. 3.3 below shows a schematic drawing of Bi deposition:

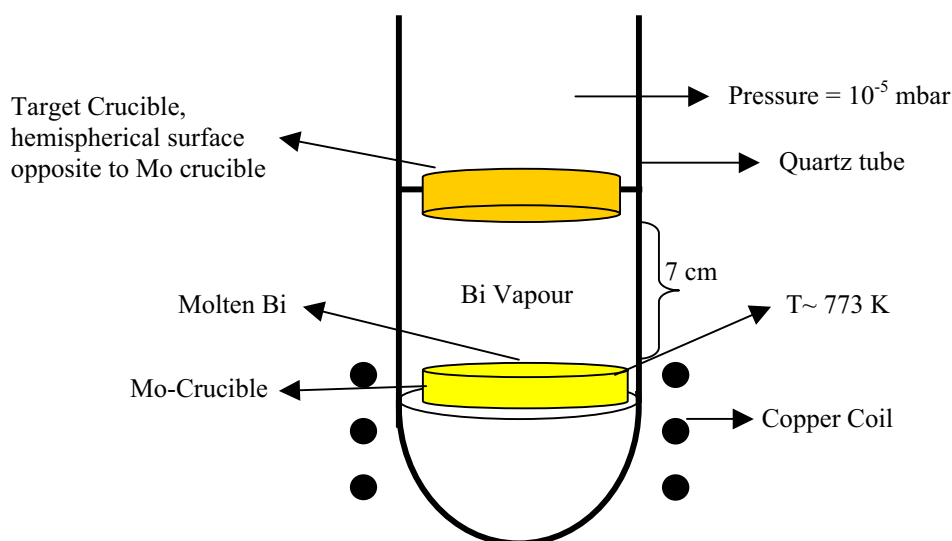


Figure 3.3. Schematic draw of Bi deposition.

After assembling, the valve on the top of the quartz tube was closed tightly. The whole tube was transferred to the induction furnace. The Bi in the lower crucible was heated to 773 K under a pressure of $< 1 \times 10^{-5}$. After about an hour a mirror was formed on the inner surface of the quartz tube from Bi vapour. The deposition was left for about three hours. It was found that this time was enough for a full coverage of the crucible surface. After this time the whole system was allowed to cool down to room temperature. Again under Ar the tube was transferred to the Ar box. A shiny thin deposited film was found on the surface of the crucible. The weight of the Bi film was found to be 25 mg. The inaccuracy in weighing did not exceed ± 0.001 g. The crucible with the Bi film was placed on a cooling plate in the box. 35.5 g of the same quality Ga were put in the glass syringe and attached to a heating plate above the crucible. After about two hours Ga flew into the crucible forming a perfect shiny surface. It is worth noting here that Ga should not be forced to flow out of the syringe by any means, otherwise some oxide will be forced to flow with it. Upon contact between the molten Ga and the Bi film on the crucible partial wetting was achieved. The Ga in the crucible solidified within 5 minutes and the crucible was weighted again. To get the composition in question the Ga was heated once more and the desired amount of distilled Bi was added. The crucible with the sample alloy was then shaken manually to attain complete wetting. The attainability of wetting in this way gave a remarkable result as was judged by eyes and later on by surface light scattering.

Some of the other sample alloys were prepared by further addition of pure distilled Bi. The addition was stopped when the liquid depth in the crucible reached 4 mm. Higher liquid depth samples were found to be very sensitive to mechanical vibrations.

For high Bi content samples > 3 at % wetting was achieved by heating the liquid sample alloy to 573 K for 3-4 hours in a newly built UHV chamber (under a residual pressure of 10^{-8} - 10^{-9} mbar) other than the one used in the case of pure Ga. This procedure was applied prior to surface energy measurements. The sample was solidified and left clean for light scattering experiments. The newly built UHV chamber was used for surface energy measurements of all sample alloys. It was built for the following reasons:

- It was improved to achieve ultra high vacuum.
- It was made suitable to install a 60 L/s ion pump not only to achieve good vacuum but also because the ion pump is a vibration-free pump. Thus vibrations at the liquid surface caused by a turbo pump were gotten rid of.

For pure Bi, wetting was easily achieved (due to its lower surface energy) in the induction furnace. The same procedure of sample preparation was also applied to the Ga-Pb system.

3.3 Measuring procedure

Before each measurement the following steps were carried out:

- All optical components were cleaned with a standard optical cleaning agent.
- The legs of the vibration-isolated table were pumped up with air until the table became horizontal. The latter was checked by means of a spirit level.

Surface light scattering measurements were performed in the following way: For pure Ga, after obtaining the minimum pressure (10^{-7} mbar) the sample was heated to the melting point of pure Ga and kept at this temperature. Then sputtering was carried out. During this time the required optical alignment was made, which is a very important step and has to be made very carefully.

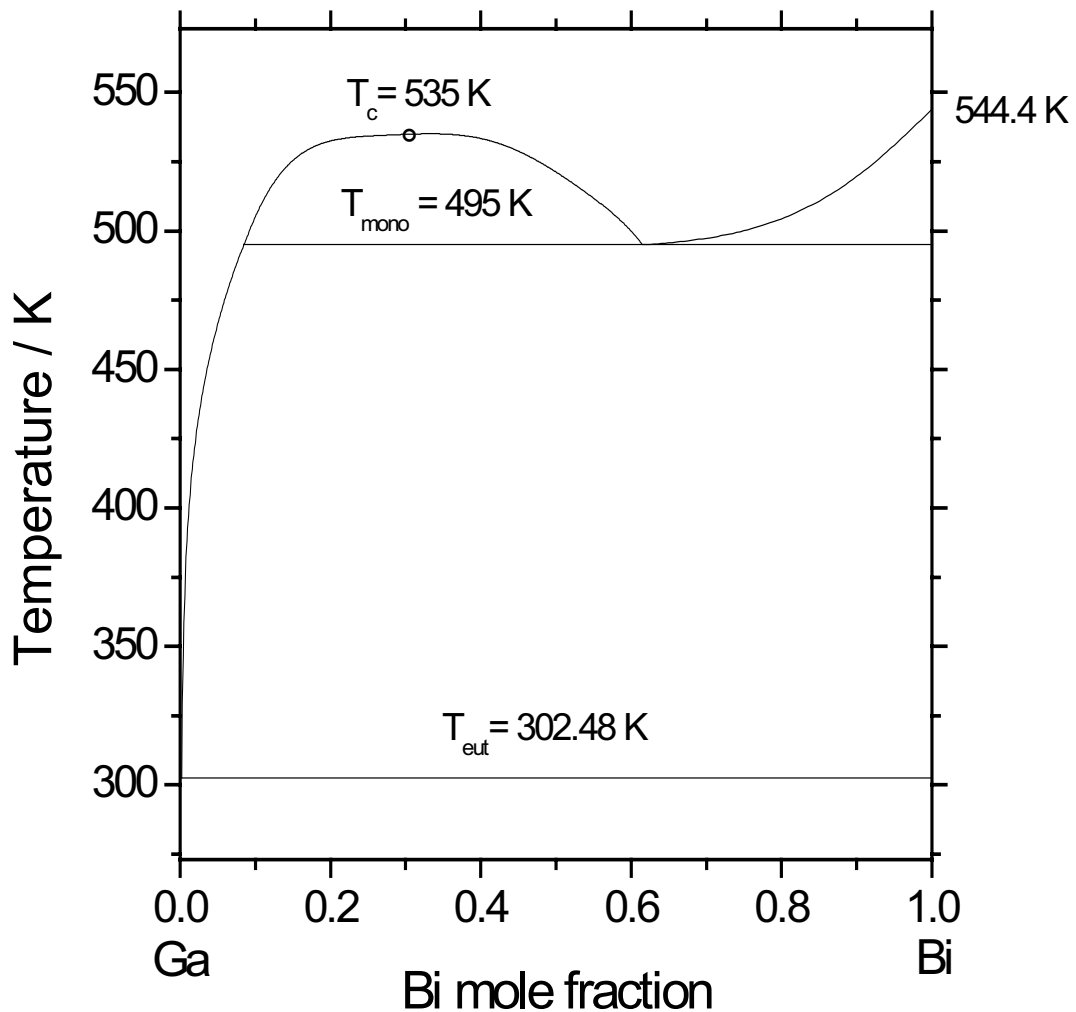
The major steps in the optical alignment are: The main beam should be made to travel parallel to the optical table. This was done by exposing the laser beam to a screen at two different positions, one close to the sample and the other close to the PMT tube. If the laser beam hits the same point on the screen at the two different positions then it is travelling parallel, otherwise the required adjustment has to be made.

A second major step in the alignment is that the circular shape of the diffracted beams of different orders has to be confirmed by focusing the beam on e.g. a piece of paper. If their shape was e.g. elliptical instead of circular, L3 (see Fig. 3.1) was moved relative to the diffraction grating until they became circular. It was found that this procedure was different from one sample to the other especially for liquid metals where this is strongly dependent on the wetting between the sample and the crucible, and on a corresponding curvature of the sample surface. After the alignment was successfully made, the laser beam was focused in the middle of the sample surface where it was slightly visible. After about 10 min of sputtering the beams on the liquid surface became completely invisible. At this stage the sputter gun was switched off and three spectra of the scattered light were recorded at that temperature. The sample was heated further under the same conditions in small temperature steps up to 373 K with a heating rate of 25 K/h. At each step the sample was left for about one hour before the spectra were recorded. The sputter gun was switched on from time to time in cases when the visibility of the beam had increased.

Upon heating the sample to above 373 K, q changed due to different wetting patterns between the liquid Ga and the crucible, probably caused by changes in surface tension of Ga. So it was not possible to keep q constant. During this measurement on pure Ga, q changed two times, in the temperature interval 303-373 K and 373-503 K. The measurement was stopped in each interval and q was measured. However above 503 K it was necessary to measure q at every temperature step, which is a time consuming procedure.

For liquid alloys the measurements were carried out in the following way. For sample alloys with a liquidus temperature less than 373 K, the sample was located in the UHV chamber on a cooling plate to keep the sample solid. When the pressure in the chamber was in the range of 10^{-8} - 10^{-9} mbar obtained by means of the ion pump and the liquid nitrogen trap, the sample was moved by a manipulator from the plate to the resistance furnace. Then it was heated again to 573 K for 3-4 hours to re-attain the thermodynamic equilibrium distribution of Bi or Pb in Ga. It was then cooled down in steps of about ~ 10 K with a cooling rate of 20 K/h. At each step the sample was left for about one hour and a trial was made to collect the spectra of the scattered light. In most sample alloys the first temperature where a spectrum could be collected was around 533 K. We tried to collect as much points as we could at the same q . In principle we could measure at higher temperatures than 533 K but each would be at a

different value of q . For samples with liquidus temperatures above 533 K we were forced to do that. Optical alignment, cleaning of the samples and collection of the spectra were done in the same way like for pure Ga. However, close to the liquidus temperature of the sample, as inferred from the phase diagrams [15, 62], see Fig. 3.4, the cooling rate was lowered to 10 K/h to see at what temperature the sample would solidify. The measurements were reproduced on heating at a heating rate of 10 K/h. Two cooling cycles were then carried out using different cooling rates, one with 35 K/h and the other with 10 K/h. As reported in [12] the temperature at which a sample alloy solidifies is cooling rate dependent. All temperature measurements were done as before.



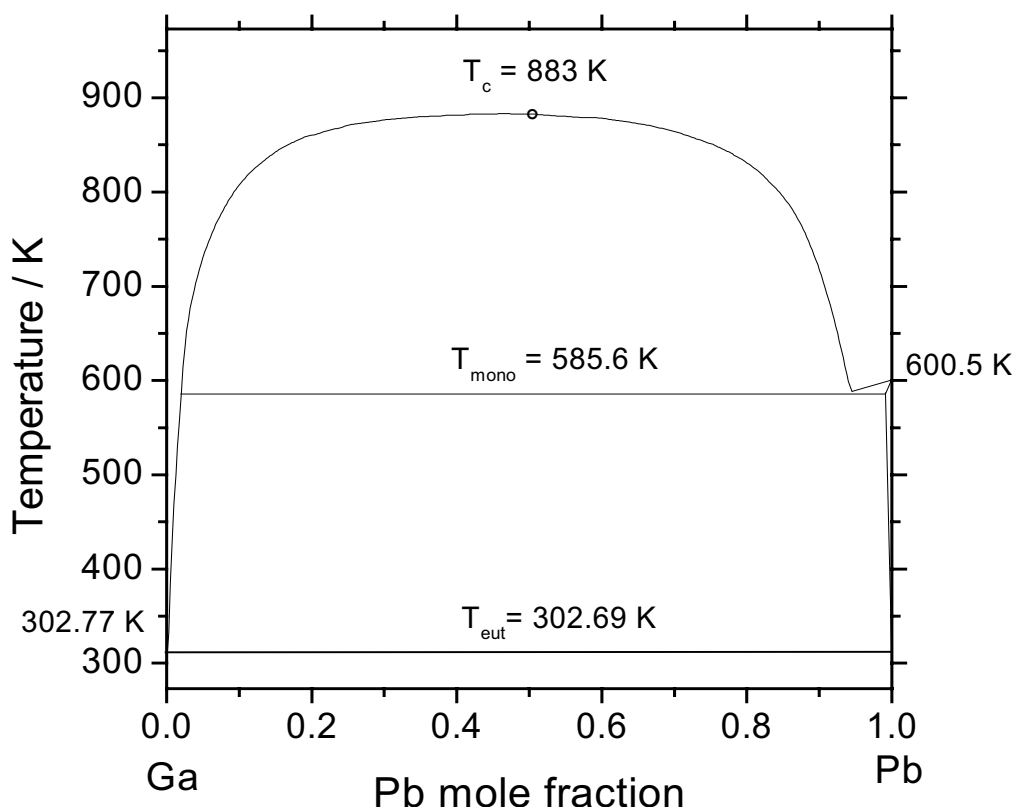


Figure 3.4. Phase diagrams of Ga-Bi (upper graph, page before) and Ga-Pb (lower graph) alloys showing the critical (T_c), monotectic (T_{mono}) and eutectic (T_{eut}) temperatures and the melting points of pure components.

The difference in temperature between the thermocouple in the bottom of the crucible and the sample surface was estimated earlier in our laboratory to be less than 3 K for surface temperatures in the range 500 – 600 K. The temperature gradient across the liquid sample alone is estimated to be below 1 K for temperatures ≤ 500 K [8]. During all measurements the optical alignment was kept constant. This is an important point here because if any optical component is moved, q is no longer corresponding to the measured parameters. All measurements were performed after normal working hours to ensure low vibration conditions.

For surface freezing measurements on Ga-Bi and Ga-Pb liquid alloys, sample preparation and cleaning was done in the same way as described before. Measurements were performed at different q , unlike the previous measurements in which q was fixed and temperature was the only variable. In each measurement the sample was also heated above the monotectic temperature for several hours to achieve

the thermodynamic equilibrium distribution of Bi or Pb in liquid Ga. The sample was then cooled down to about 30 K above the liquidus point according to the corresponding phase diagrams. Cooling was further carried out in steps of 2 K each at a cooling rate of 8 K/h. At each temperature the sample was left for about one hour and spectra were recorded for different values of q .

In some measurements it was not possible to collect spectra for a sequence of q 's in the same diffraction pattern. So under certain circumstances it was necessary to reduce the separation between the diffraction orders due to the fact that the scattered intensity decreases rapidly with q as already mentioned before. Measurements on cooling were carried out until the point where no spectra could be obtained anymore. This is when the liquid surface is completely frozen and as a consequence capillary waves are completely damped. As could be seen with naked eye surface freezing starts in a form of thin solid islands of Bi or Pb on the surface of the liquid alloys. In the beginning these islands are little apart from each other. After a short time they are enlarged and cover the liquid surface completely. An interesting observation in these measurements is that the diffraction orders as well as the main beam merge each other due to the increase of their shapes caused by the surface freezing films. This is not the case for example when one focuses the beams on a solid surface e.g. the surface of the Mo crucible. In the latter case the diffraction pattern is still in shape and the orders are still well defined. In the former case, this could be due to the presence of two interfaces upon the formation of a surface freezing film on top of the bulk liquid alloy. Measurements were reproduced in a different heating cycle with the same rate as on cooling. On heating, the sample was again heated to 573 K for several hours and then cooled down until surface freezing was observed. It was kept at the surface freezing temperature and was not cooled down to room temperature. As was recently reported in [12], the melting temperatures of these surface freezing films (Bi or Pb surface films) depend on how far the sample was cooled below the surface freezing temperatures. For example if the sample of the surface freezing film is kept at the surface freezing temperature and then heated, the temperature of surface melting will not be the same as if the sample was cooled down to room temperature. In other words the melting points of these surface freezing films depend on the cooling history of the sample as a whole. This was also observed in the present measurements.

3.4 Wave number measurements and data analysis

3.4.1 Measurements of the incident and the scattering angles

For measurements of the wave number q it is necessary that both the incident angle θ_i and the scattered angles $\Delta\theta$ are measured (see equ. 2.12). In our light scattering apparatus the optical geometry is made to work close to normal incidence. This geometry is recommended to avoid beam separation problems especially when working with liquids of large refractive index. In addition, the scattered intensity is slightly enhanced when working close to normal incident [44]. The incident angle of our geometry was measured as follows: Two right angle prisms (not shown in Fig. 3.1 for clarity) were used for beam direction, one is to direct the incident beam on the liquid surface and the other is to direct the scattered beam. Both were placed on a rotating stage graduated in a sub-degree precision. The prism before the liquid surface was rotated to retro-reflect the reflected beam from the liquid surface back to P1. In this way what one actually does is moving the prism from its tilted position to its horizontal position, see Fig 3.5. As the prism is rotated, the incident beam is moved from a position of making an angle with respect to the surface normal to a position of being parallel to the surface normal. The obtained reading in the rotation stage is just θ_i . The figure below demonstrates the rotation of the right angle prism with respect to the sample surface, where $\phi = \theta_i$.

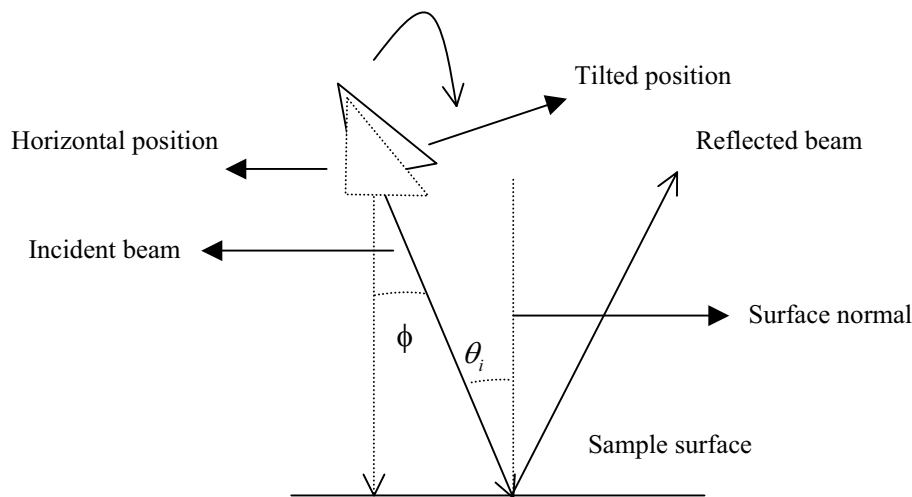


Figure 3.5. Rotation of the right angle prism with respect to the sample surface.

Another possible way of measuring θ_i in our apparatus is to measure the distance d between the two spots of the incident and the scattered beam at the quartz window of

our UHV chamber and the distance x between the quartz window and the sample surface (see Fig. 3.1). In this way $\theta_i = \tan^{-1}(d/2x)$. Both ways used to give the same results provided that x is accurately measured. θ_i in our geometry was in the range $1\sim 3^\circ$ depending on the required alignment.

The scattering angle $\Delta\theta$ was measured by exposing the diffracted beams on a screen at two different positions, one close to the PMT and the other close to the liquid sample. With a CCD camera connected to a computer, images of the scattered pattern were recorded at these two positions. The distance z between the two was measured. The images were then digitized and the maximum intensity in each diffraction order was evaluated assuming a Gaussian intensity distribution [58].

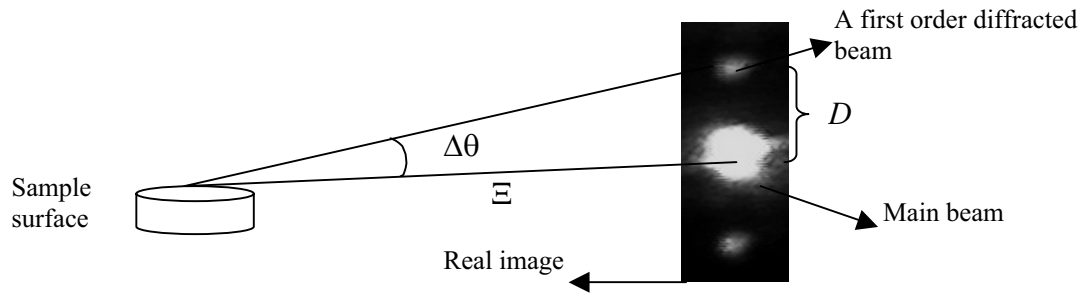


Figure 3.6. Geometry for $\Delta\theta$ measurement with a real image recorded from liquid $\text{Ga}_{0.9873}\text{Bi}_{0.0127}$ alloy surface as an example.

The digitised data were fitted with a function in the form [58], see Fig. 3.7,:

$$I(x_0) = A \exp(-((x - x_0)/C)^2) + B. \quad (3.1)$$

where A is an amplitude, B is a background. x_0 is the goal parameter reflecting the position of the maximum intensity in the diffraction order. The distance between two neighbouring diffraction spots D for each image was determined in sub-pixel precision. Another way to measure $\Delta\theta$ is simply to record one image near PMT and

measure the distance Ξ between the sample surface and the screen (see Fig. 3.6). Note that since $\Delta\theta \ll 1$, $\tan\Delta\theta = \Delta\theta$ and $\Delta\theta = D / \Xi$. The absolute inaccuracy in q measurements did not exceed 0.2%. One important point here when recording an image is that the screen has to be placed as far as possible from the sample in order to achieve high quality images.

The main difficulty when working close to normal incidence is that one can't have a large separation between the diffraction orders. If one wishes to have a large separation between the main beam and the first spot, which is recommended [44], then this would imply that the second and the subsequent orders will also be largely separated from one another and q will be large leading to a large reduction in the scattered intensity of the higher orders (e.g. third order).

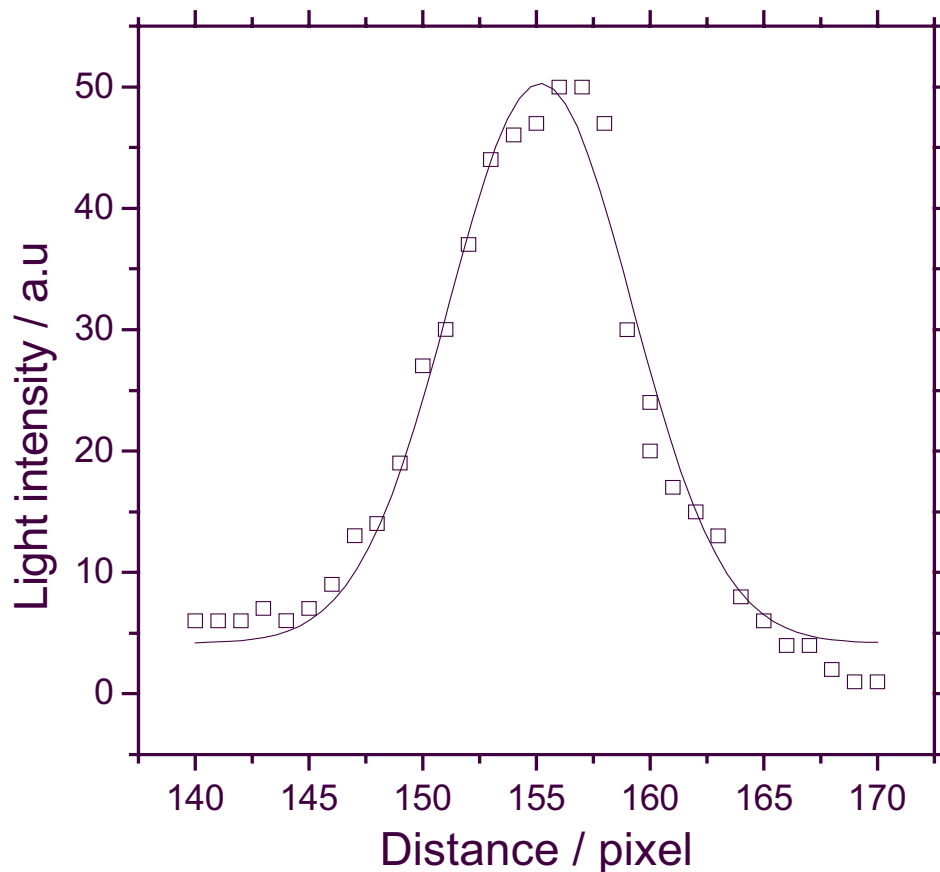


Figure 3.7. Fit of the light intensity in the first order (+1) beam of the real image in Fig. 3.6 to equ. (3.1). (\square) experimental data. The parameter reflecting the position of the maximum intensity was determined to be $x_0 = 155.4 \pm 0.16$.

The distance D between the main beam and the first order spot in Fig. 3.6 was found to be the optimum separation in our optical geometry. The distance between the

diffraction grating and L3 mainly determines this separation. A good separation between the diffraction orders is highly recommended for precise determination of q . It was found in our work that this separation is not constant even for the same sample and at constant temperature. For example if one performs a light scattering experiment with a sample alloy and cools it down to room temperature and then heat it again keeping a fixed distance between the diffraction grating and L3, one will find that another alignment is required, probably due to changing wetting characteristics between the sample and the crucible. It has to be stressed here that when working with liquid metals and alloys the optical measurements are highly dependent on the quality and geometry of the sample surface. A good sample preparation will lead to good measurements. By a good sample it is meant one in which the surface is flat and clean.

3.4.2 Data analysis, instrumental broadening corrections and error discussion

Our light scattering data were analysed as follows: As was mentioned before, three spectra were recorded at each temperature. The spectra were fitted with the theoretical spectrum in equ. (2.29), by means of a least square algorithm according to Lavenberg-Marquardt method.

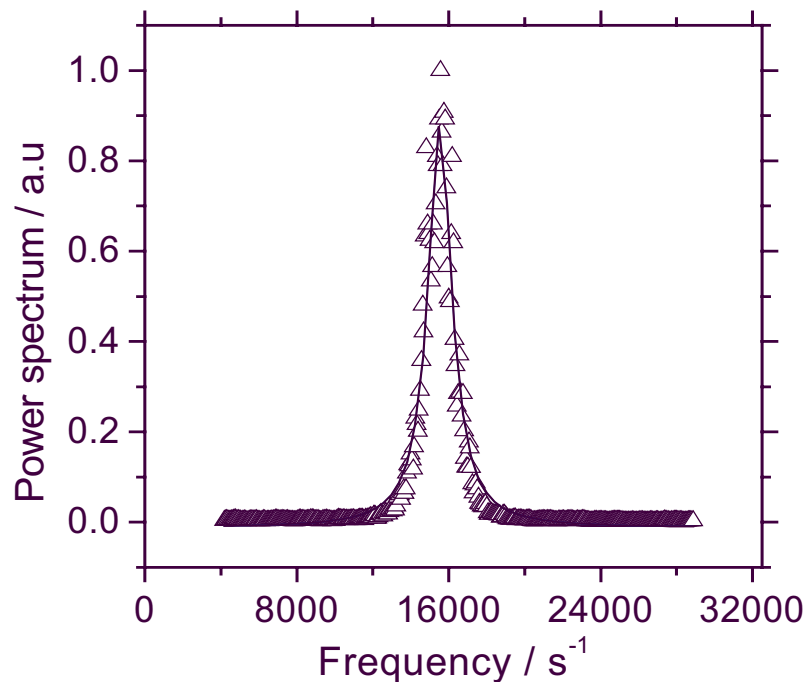


Figure 3.8. Power spectrum of light scattered from pure liquid Ga surface, (Δ) are experimental points, solid line is fit to result according to equ. (2.29).

Five parameters were extracted from each fit, the amplitude A , background B , peak frequency ν ($\omega = 2\pi\nu$), damping coefficient κ and instrumental broadening β . The one which gives the best fit parameters was used for σ and η evaluations.

Fig. 3.8 shows a power spectrum of light scattered from the surface of pure liquid Ga at the melting point, $q = 431.3 \text{ cm}^{-1}$. The main parameters obtained from the fit are:

$\nu = 15514 \pm 10.3 \text{ s}^{-1}$; $\kappa = 340 \pm 26 \text{ s}^{-1}$; $\beta = 200.2 \pm 9 \text{ s}^{-1}$. Note that each parameter should be multiplied by 2π to get angular quantities. Using equ. (2.6) and the literature value of the density of pure Ga $\rho = 6.0 \text{ g cm}^{-3}$ [63], the surface tension and viscosity of pure liquid Ga at the melting point from these data are:

$$\sigma = 710 \pm 5 \text{ mJm}^{-2}; \quad \eta = 3.44 \pm 0.27 \text{ mN}\cdot\text{s}\cdot\text{m}^{-2}$$

The error in both quantities was calculated according to Gauss' error formula:

$$\Delta f(x, y, z) = \left| \frac{\partial f}{\partial x} \right| \times |\Delta x| + \left| \frac{\partial f}{\partial y} \right| \times |\Delta y| + \left| \frac{\partial f}{\partial z} \right| \times |\Delta z|, \quad (3.2)$$

Since the error in the density is much smaller than one percent, it can be neglected and the errors in σ and η become:

$$\Delta \sigma = \sigma \left[2 \left| \frac{\Delta \omega}{\omega} \right| + 3 \left| \frac{\Delta q}{q} \right| \right]; \quad \Delta \eta = \eta \left[\left| \frac{\Delta \kappa}{\kappa} \right| + 2 \left| \frac{\Delta q}{q} \right| \right]. \quad (3.3)$$

Equs. (3.2) and (3.3) show that the accuracy of σ is twice the accuracy on ω plus three times the accuracy on q and the accuracy of η is one time the accuracy on κ plus two times the accuracy on q . As can be seen above the error in σ is 0.73%, whereas the error in η is $\sim 10\%$. Generally speaking the error in σ of all our measurements was always in the range 0.3-1% indicating a good accuracy of our measurements in case of σ . However the error in η was in the range 3-50%. The cause of the error in damping will be discussed in details later on in chapter 5.

The viscosity above is calculated with the experimentally determined spectral width. However due to finite size of the laser beam (see chapter 2) this width or more precisely the half width and half height of the spectrum are usually larger than the intrinsic width (without the extra broadening). At low q and in the weakly damped regime, as it is in this work, instrumental broadening corrections are important. In this

case β is not negligible in comparison to κ . A simple formula was suggested for damping correction [44, 64]:

$$\kappa_{in} \cong \kappa - \frac{\beta^2}{\kappa}. \quad (3.4)$$

where κ_{in} is the intrinsic width of the measured power spectrum. Applying this simple correction to our measured parameter above, the damping becomes $\kappa_{in} = 1395 \pm 144 \text{ s}^{-1}$ and $\eta = 2.25 \pm 0.22 \text{ mN}\cdot\text{s}\cdot\text{m}^{-2}$.

If $\kappa < \beta$, the observed damping is a measure of the resolution of the measurement and κ_{in} can not be determined with good accuracy [64]. If $\beta = \kappa$ this may be due to the assumption made that the instrumental function is Gaussian.

Chapter 4

Results

4.1 Surface tension of pure liquid Ga and its temperature dependence

The surface tension of pure liquid Ga σ_{Ga} has been measured from the melting point $T_m = 303$ K up to 503 K. Fig. 4.1 shows the temperature dependence of σ_{Ga} obtained here indicated by the solid symbols, which is an average of two separate measurements in comparison to recent measurements of Serre *et al* [15] (open symbols) using the sessile drop method. The surface tension was determined from equ. (2.6). The density of Ga at each temperature was taken from the literature [63]. As can be seen in Fig. 4.1 concerning our data, pure Ga exhibits an anomalous behaviour: a positive temperature derivative of σ_{Ga} ($d\sigma_{Ga}/dT$) up to about 325 K, and a negative temperature derivative for $T > 325$ K, $(-0.088 \pm 0.0074) \cdot 10^{-3} \text{ Jm}^{-2}\text{K}^{-1}$. Both of our measurements showed the same behaviour. A similar anomalous behaviour has been reported recently [65] and is also indicated in the measurements of Serre *et al* by the open triangles in Fig. 4.1.

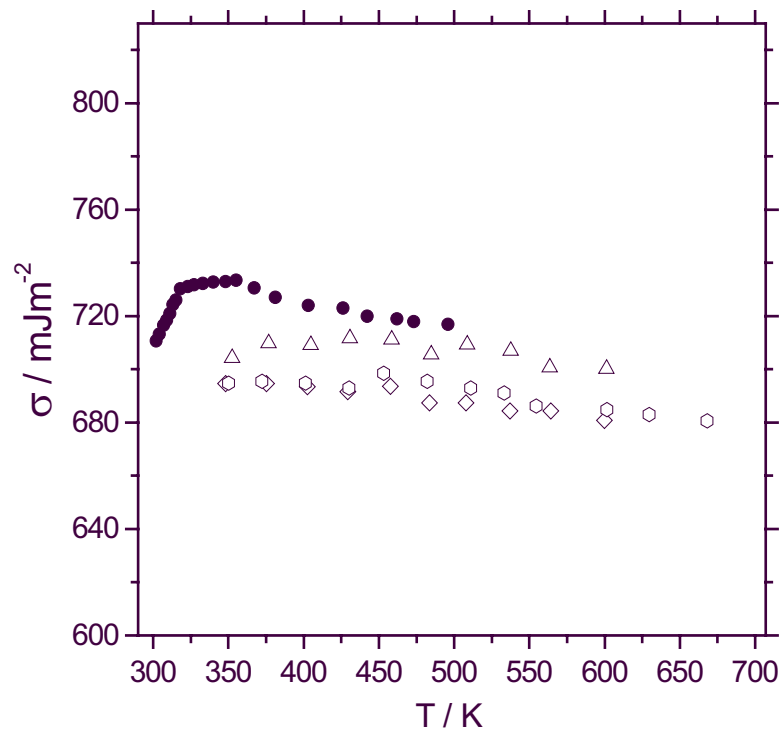


Figure 4.1. Temperature dependence of the surface tension of pure liquid Ga. Solid symbols represent our data, open symbols the data of Serre *et al* [15].

The surface tension of liquid Ga has been studied extensively [66-72]. These studies have been carried out with invasive methods (e.g. sessile drop, bubble pressure etc). Only one study has been carried out so far with the non-invasive method of capillary wave spectroscopy, that of reference [65]. However, in the latter study measurements were carried out during sputtering and up to ~ 423 K. In addition, the reported values of the temperature coefficients of the surface tension are extremely high ($d\sigma/dT = 4.18 \pm 0.2$ for $373 \leq T \leq 423$ K and $d\sigma/dT = -0.57 \pm 0.09$ for $303 \leq T \leq 373$ K). Going back to Fig. 4.1, agreement is found at higher temperatures between our measurements and that of Serre *et al* within experimental errors. General agreement is also found with other reported measurements [66-72]. Table 4a summarizes the results of the surface tension of Ga and its temperature coefficient of references [66-72] in addition to that of ref. [15].

Reference	σ_{Ga} (mJm ⁻²)	$d\sigma_{Ga}/dT$ (mJm ⁻² K ⁻¹)	Method
[15]	708	-0.064	Sessile drop
[66]	708	-0.066	Sessile drop
[67]	712	-0.0606	Sessile drop
[68]	715	-0.088	Sessile drop
[69]	680	-0.091	Sessile drop
[70]	718	-0.101	Sessile drop
[71]	715	-0.0804	Sessile drop
[72]	860	-0.16	Big drop

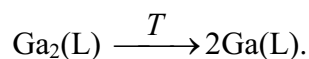
Table 4a. Summary of the results of the surface tension of liquid Ga and its temperature coefficient of references [66-72] and [15], for $T > 400$ K.

A linear fit of our data for $T > 325$ K yields the following relation:

$$\sigma_{Ga,T} = (733.5 \pm 3.3) \cdot 10^{-3} \text{ Jm}^{-2} - (0.088 \pm 0.007) \cdot 10^{-3} \text{ Jm}^{-2}\text{K}^{-1}(T - T_m).$$

where T_m is the melting point. However, as already mentioned in chapter 3, the surface tension of liquid Ga at the melting point is 710 mJm^{-2} . This value was calculated using the light scattering data at T_m only and should not be confused with the value obtained by the linear fit in equ. (4.1) since the surface tension of Ga shows a curved behaviour as a function of temperature. With exception of the results of [72],

in which σ_{Ga} is about 20%, and $d\sigma_{Ga}/dT$ 50% higher, our data show good agreement with those in table 4a. One interesting feature of our results is that σ_{Ga} goes through a distinguished maximum with temperature. The latter was not observed in the measurements of table 4a, though a slight curvature is observed in the measurement of Serre *et al.* Hardy [66] made a profound study and detailed comparison of his own results on σ_{Ga} and its temperature dependence with almost all the measurements carried out prior to his work. The majority of these studies are also stated in table 4a. He found that almost half of these studies report on a non-linear decreasing function of σ_{Ga} with temperature, while the others report a linear monotonic decrease of σ_{Ga} . He attributed the non-linear decreasing behaviour to high surface coverages of solid impurities. One improvement in his measurements as he mentioned is the use of an Ar ion sputter gun in combination with an Auger spectrometer, which were not used in the other studies. In this work we have also used a sputter gun (see chapter 2). During our measurements on Ga we did not have high surface coverage of solid impurities since the laser beam focused on the Ga surface was invisible. In case of high surface coverage of solid impurities, the laser beam is strongly visible. Taking the whole temperature range of our study, our data do not show the same non-linear decrease of σ_{Ga} nor the linear one but rather as mentioned earlier an increasing behaviour up to 325 K and a decreasing behaviour above 325 K. We can not decide whether this anomalous behaviour of σ_{Ga} as a function of temperature is associated with light segregated impurities, which have not been removed completely by sputtering, or due to ordering of molecular Ga_2 -species at the surface, which dissociate with increasing temperature [73]:



If this anomalous behaviour of $\sigma_{Ga}(T)$ is real, it would imply an increase of the surface entropy of Ga $S^\sigma = -d\sigma_{Ga}/dT$ with T , from negative at low T to positive at high T . An increase in entropy is correlated with disordering of the surface at high temperatures [38].

4.2 Temperature and composition dependence of the surface energy of Ga-Bi and Ga-Pb liquid alloys

In this section we first present the results of surface light scattering measurements obtained on the liquid Ga-Bi alloys. Measurements of the surface tension as a function of temperature and Bi mole fraction, $\sigma(T; x_{Bi})$, ($0 \leq x_{Bi} \leq 1$) have been performed in the homogeneous liquid phase of the Ga-Bi alloy. The experimental studies have been concentrated on the Ga-rich composition range below the monotectic point ($x_{Bi} = 0.085$; $T_{mon} = 495$ K). Fig. 4.2 shows typical light scattering spectra of a $\text{Ga}_{0.9986}\text{Bi}_{0.00135}$ liquid alloy surface at 303 K (left) and 465 K (right) both collected at the same $q = 443.9 \text{ cm}^{-1}$. The shift in peak frequency and the changes in spectral width, amplitude are clearly visible.

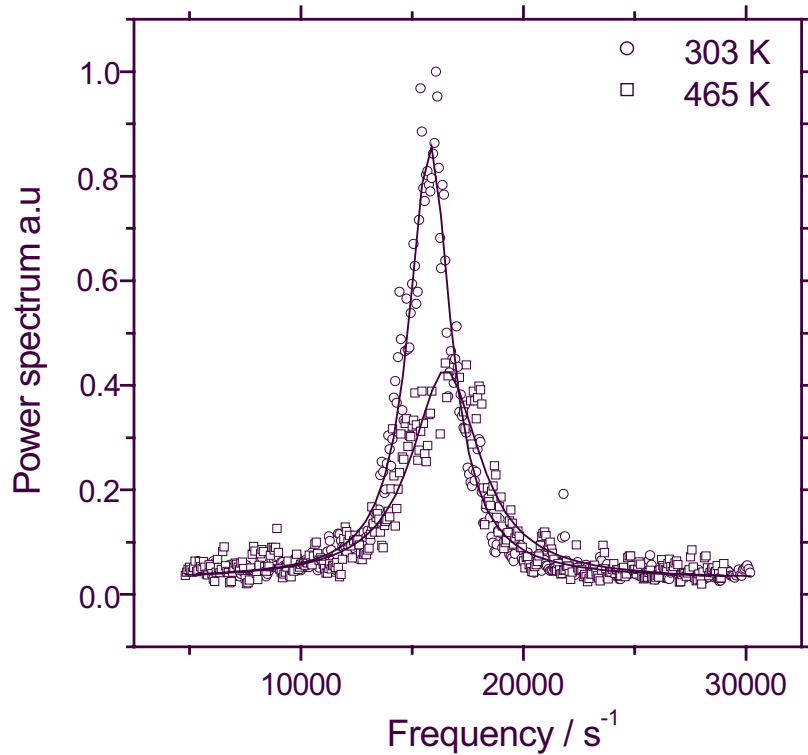


Figure 4.2. Typical light scattering spectra of a $\text{Ga}_{0.9986}\text{Bi}_{0.00135}$ alloy surface at 303 K (left) and 465 K (right); symbols correspond to experimental spectra, lines to Lorentzian fits. The change in peak width and centre frequency upon heating is clearly visible.

Fig. 4.3 below shows typical capillary wave spectra collected at 482 K of the free surfaces of pure Ga, the eutectic $\text{Ga}_{0.9978}\text{Bi}_{0.0022}$ and $\text{Ga}_{0.949}\text{Bi}_{0.051}$ liquid alloys surfaces at $q = 400.3$, 319.12 and 359.7 cm^{-1} , respectively.

Apparent is the increase in the peak width with Bi concentration. Distinct from spectra of light scattered by surfaces of dielectric liquids (e.g. water, acetone etc.), almost all spectra of the light scattered by surfaces of liquid metal alloys of this work show a higher scattering of data points, as can be seen in Figs. 4.2 and 4.3. This is due to different factors: the scattering intensity I_s is proportional to the mean square amplitude of capillary waves $\langle \xi_q^2(0) \rangle$ as [44]:

$$dI_s / d\Omega \propto I_R \langle \xi_q^2(0) \rangle. \quad (4.1)$$

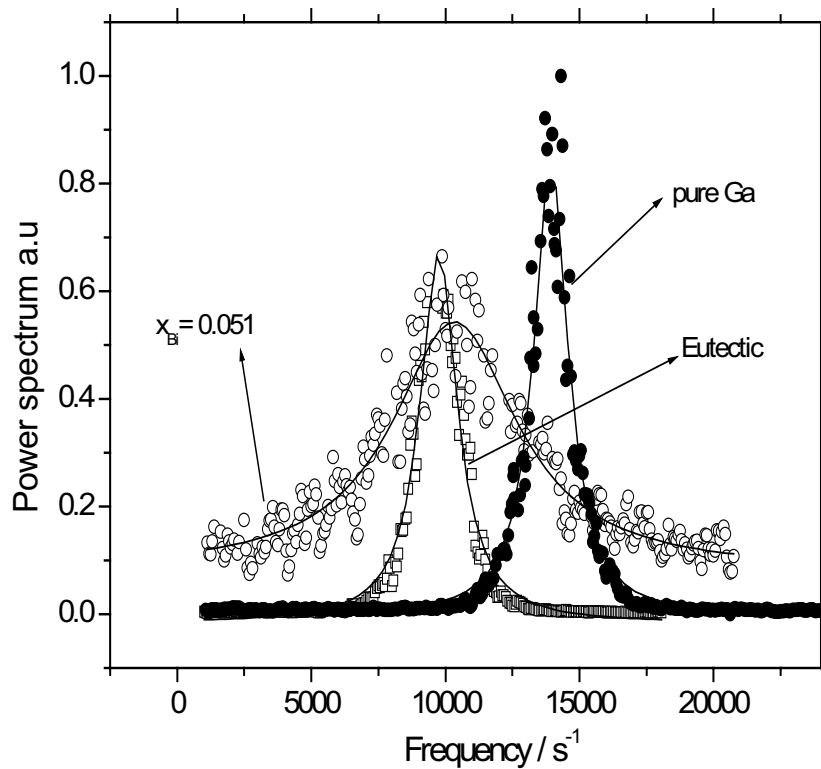


Figure 4.3. Spectra collected at 482 K of the light scattered by pure Ga and the eutectic $\text{Ga}_{0.9978}\text{Bi}_{0.0022}$ and $\text{Ga}_{0.949}\text{Bi}_{0.051}$ liquid alloys surfaces at $q = 400.3, 319.12$ and 359.7 cm^{-1} , respectively.

where I_R is the reflected intensity, $d\Omega$ is a solid angle of scattering and $\langle \xi_q^2(0) \rangle$ is given by equ. (2.3) (see chapter 2). From equ. (2.3), the capillary wave amplitude is inversely proportional to the surface tension and density of the liquid. Since in general liquid metals and alloys have an order of magnitude higher surface tension $\sigma_{\text{Ga-Bi}} \sim 10\sigma_{\text{H}_2\text{O}}$ and a factor of ~ 6 higher density than dielectric liquids, the

amplitude of capillary wave is smaller for the former and thus the scattering intensity is less, which leads to the domination of the reflected intensity over the scattered one. We have also found that liquid metals and alloys surfaces are more sensitive to mechanical vibrations than dielectric liquids, which is also due to higher surface tension of liquid metals and alloys as mentioned above. The effect is greater at high temperatures, both density and viscosity decrease with increasing temperature and samples were found to be much more sensitive. The relatively high scattering of data points in the spectra was found not to affect the peak frequency.

Surface tension measurements on the Ga-Bi alloys are summarized in Fig. 4.4. These values have been calculated using equ. (2.6). The density of the alloys at each temperature is taken from the literature [63].

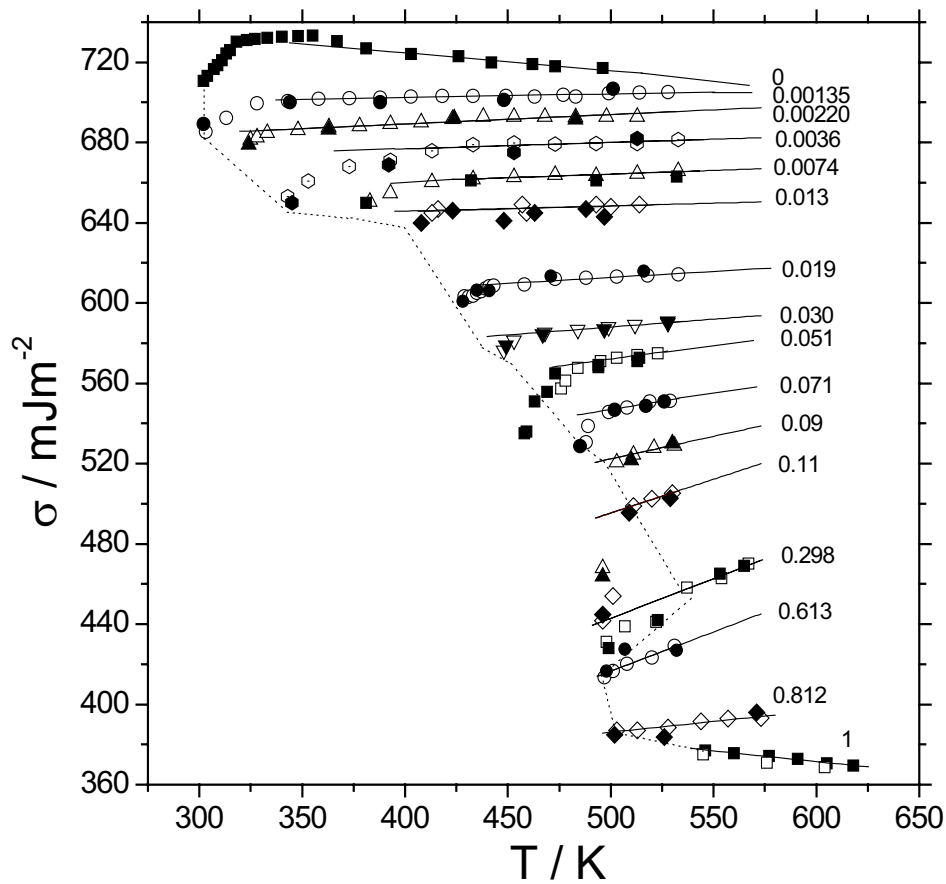


Figure 4.4. Temperature dependence of the surface tension of liquid Ga-Bi alloys determined from capillary wave spectra with $x_{Bi} = 0.00135$ to 0.812 from top to bottom in the graph and pure Bi. Solid symbols are taken on heating and open symbols are on cooling. The solid lines are the linear fits to the data in the homogeneous phase region extrapolated to 573 K. The dashed line connects points near the coexistence curve for the respective σ -isopleths.

Included in the σ versus T plot are the respective (T, x_{Bi}) -coordinates where the σ -isopleths cross the homogeneous liquid phase boundary which are connected by dashed lines to guide the eye. Measurements have been performed on heating and cooling which is indicated by full and open symbols in Fig. 4.4. It can be seen with exception of pure Bi, that all alloys exhibit a positive temperature dependence of σ , which in principle is explained by two opposite effects: reduction of σ with T due to an increase of the surface entropy with temperature and a reduction of surface segregation of the low-tension Bi-component with T .

A remarkable temperature effect is indicated in some of the $\sigma(T; x_{Bi})$ -curves approaching the liquidus curve for $x_{Bi} < x_m$. At a distance of 10 - 20 K above the phase boundary - dashed line in Fig. 4.4, kinks are visible in the slope of $\sigma(T; x_{Bi})$. The existing data e.g. for $x_{Bi} = 0.0126, 0.051$ or 0.0709 indicate a jump in the surface excess entropy density:

$$\Delta S^\sigma = \partial\sigma / \partial T(T < T_k) - \partial\sigma / \partial T(T > T_k) > 0.$$

which is the signature of a first order surface phase transition. This issue will be demonstrated in details in a subsequent section on surface freezing in Ga-Bi alloys. It is interesting to note that the temperature dependence of σ of pure Bi does not exhibit anomalous behaviour like in the case of pure liquid Ga. Rather a normal monotonic decreasing behaviour is obtained. This indicates a difference in the surface properties of liquid Ga and Bi. A linear fit to the data of pure Bi yields the following relation:

$$\sigma_{Bi}(T) = (379 \pm 5) \cdot 10^{-3} \text{ Jm}^{-2} - (0.106 \pm 0.005) \cdot 10^{-3} \text{ Jm}^{-2}\text{K}^{-1} (T - T_m).$$

The obtained values of the surface tension and its temperature coefficient are in good agreement with those obtained by Arsamikov *et al* [71]:

$$\sigma_{Bi} = 375 \text{ mJm}^{-2} (T = T_m); d\sigma_{Bi} / dT = -0.07 \cdot 10^{-3} \text{ Jm}^{-2}\text{K}^{-1}.$$

which have been measured by the sessile drop method. The concentration dependence of the surface tension of the Ga-Bi alloys at 573 K, where data exist in the literature [71-72], is shown in Fig. 4.5.

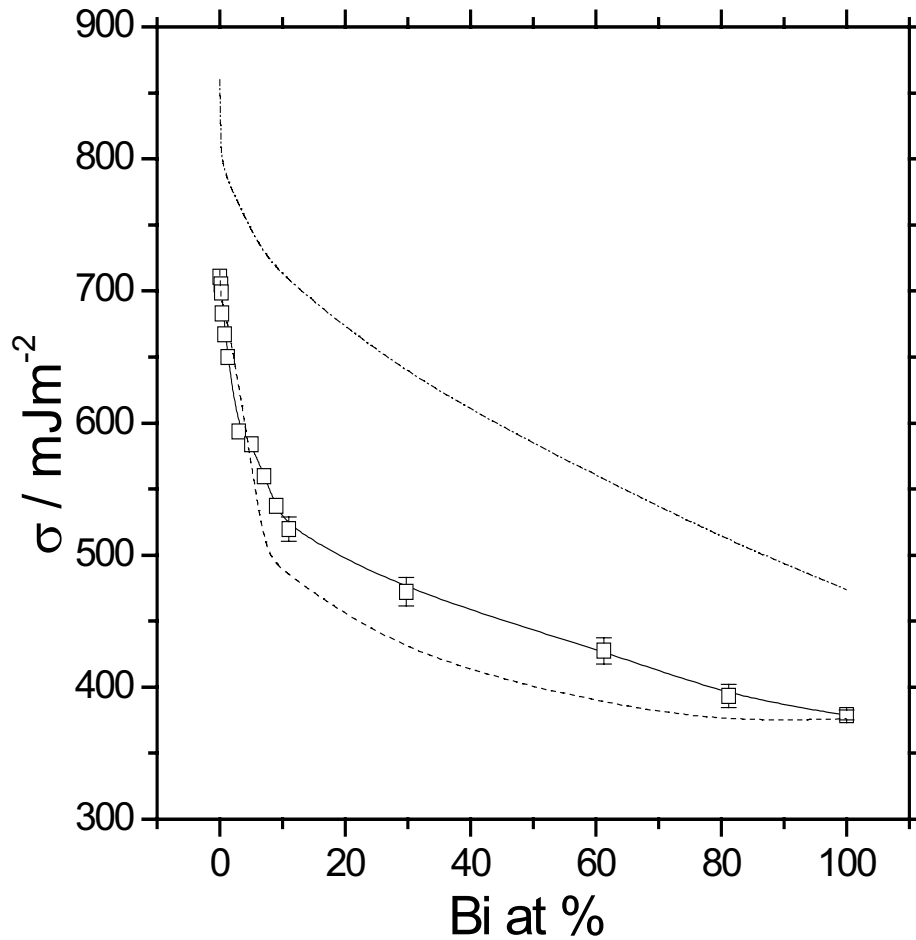


Figure 4.5. Surface tension σ of liquid Ga-Bi alloys versus composition in at % Bi at a constant temperature of 573 K; comparison of σ -data of this work (\square) with literature data: dashed line (---) represents the data of ref. [71], dashed-dotted line (-.-.) of ref. [72].

As clearly seen in Fig. 4.5, σ decreases with increasing Bi content, an indication of Bi segregation on the intrinsic liquid-vapour interface. Within experimental errors our results agree quantitatively with those of Arsamikov *et al* [71] up to about $x_{Bi} = 0.1$, whereas there is a slight difference at higher Bi-concentrations. There is a clear discrepancy with the data of Ashkhotov *et al* [72]. One source of this discrepancy could be the purity of the alloy surface. In what follows we present results on the Ga-Pb liquid alloys. Fig. 4.6 shows light scattering spectra at the surface of $\text{Ga}_{0.999102}\text{Pb}_{0.000898}$ (upper graph) and $\text{Ga}_{0.9958}\text{Pb}_{0.0042}$ (lower graph) alloys surface at $T = 358, 568$ K and at $q = 392, 453.4 \text{ cm}^{-1}$, respectively.

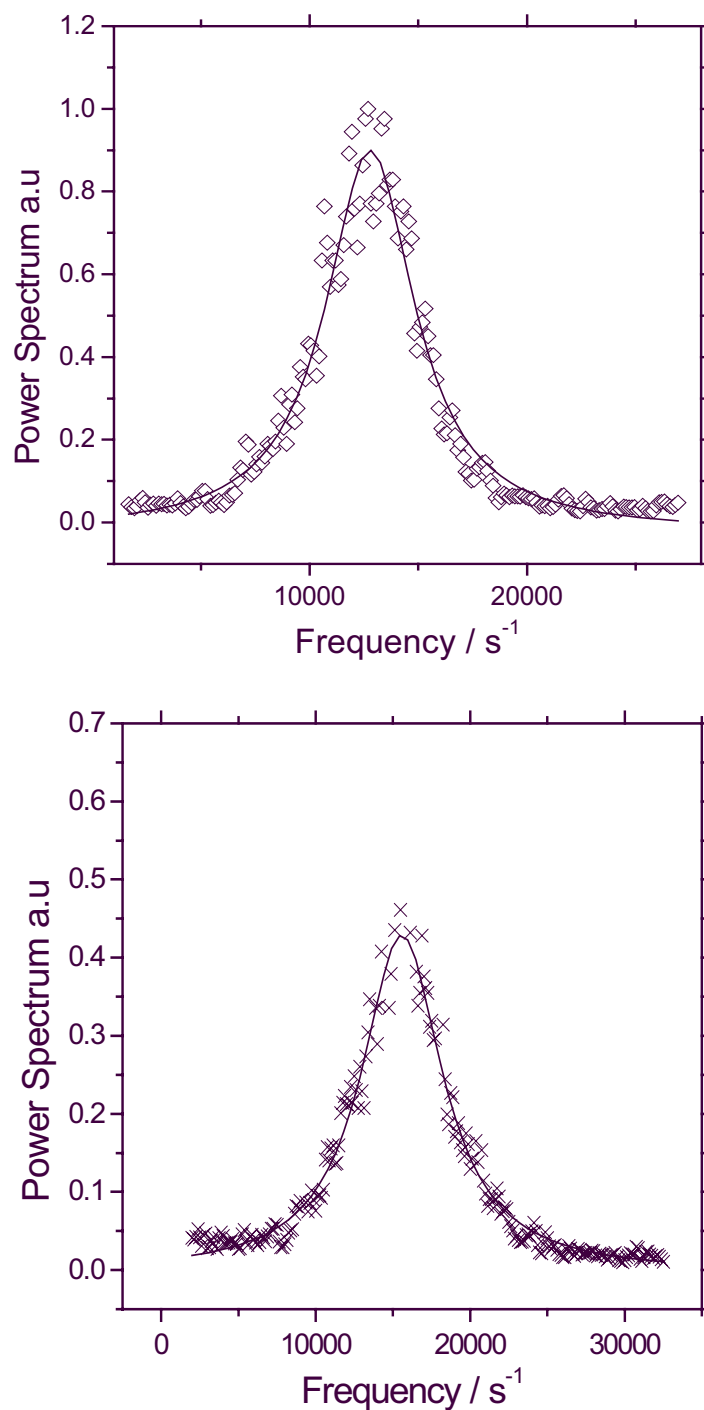


Figure 4.6. Light scattering spectra of a $\text{Ga}_{0.999102}\text{Pb}_{0.000898}$ (upper graph) and $\text{Ga}_{0.9958}\text{Pb}_{0.0042}$ (lower graph) alloy surfaces at $T = 358, 568$ K and at $q = 392, 453.4$ cm⁻¹, respectively; symbols correspond to experimental spectra, lines to Lorentzian fits.

Surprisingly the spectrum at high temperature and q (568 K, 453.4 cm⁻¹) is less noisy and the fit with the theoretical spectrum (equ. 2.29) is better. This is one of the rare cases found in this work. The general trend as mentioned before is the opposite. See

e.g. Fig. 4.7 below, which shows a light scattering spectrum of the same Pb alloy concentration as in the upper graph of Fig. 4.6 but at higher temperature.

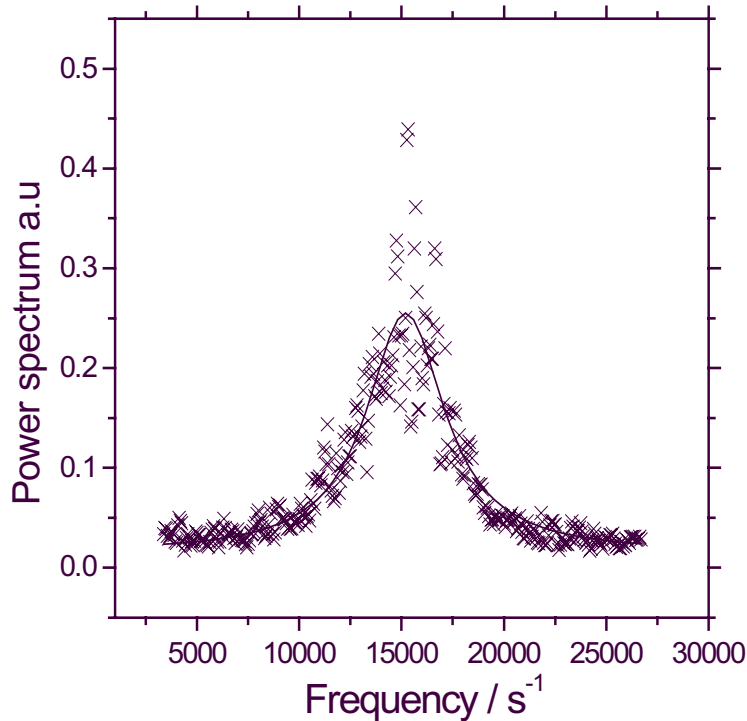


Figure 4.7. Spectrum of light scattered by a $\text{Ga}_{0.999102}\text{Pb}_{0.000898}$ alloy surface at $T = 582$ K, $q = 436$ cm^{-1} .

Measurements on the liquid Ga-Pb alloys have been performed in the composition range $0 \leq x_{\text{Pb}} \leq 0.012$, well below the monotectic point ($x_m = 0.024$; $T_{\text{mon}} = 585.6$ K), on the Ga-rich side of the phase diagram. Interest in this regime is high, where wetting and prewetting related adsorption transitions are discussed [15]. Measurements here are carried out in the homogeneous liquid phase.

Fig. 4.8 summarizes the results of the surface free energy as determined from the capillary wave spectra (see chapter 2). Measurements have been performed on heating and cooling, indicated by full and open symbols, respectively. The surface tension of the alloys at each temperature was calculated using equ. (2.6). The density was taken from the literature [74]. The results in Fig. 4.8 show that for $x_{\text{Pb}} < x_{\text{eut}} = 0.0006$, the alloys exhibit a somewhat similar behaviour to that of Ga: a positive temperature dependence of σ at low temperatures and a negative one at high temperatures. Above x_{eut} they all exhibit a positive temperature dependence. Within experimental errors, the

data for $x_{Pb} = 0.00089$ do not exhibit a negative temperature coefficient of σ at high temperatures. Whereas they change to positive values at lower temperatures.

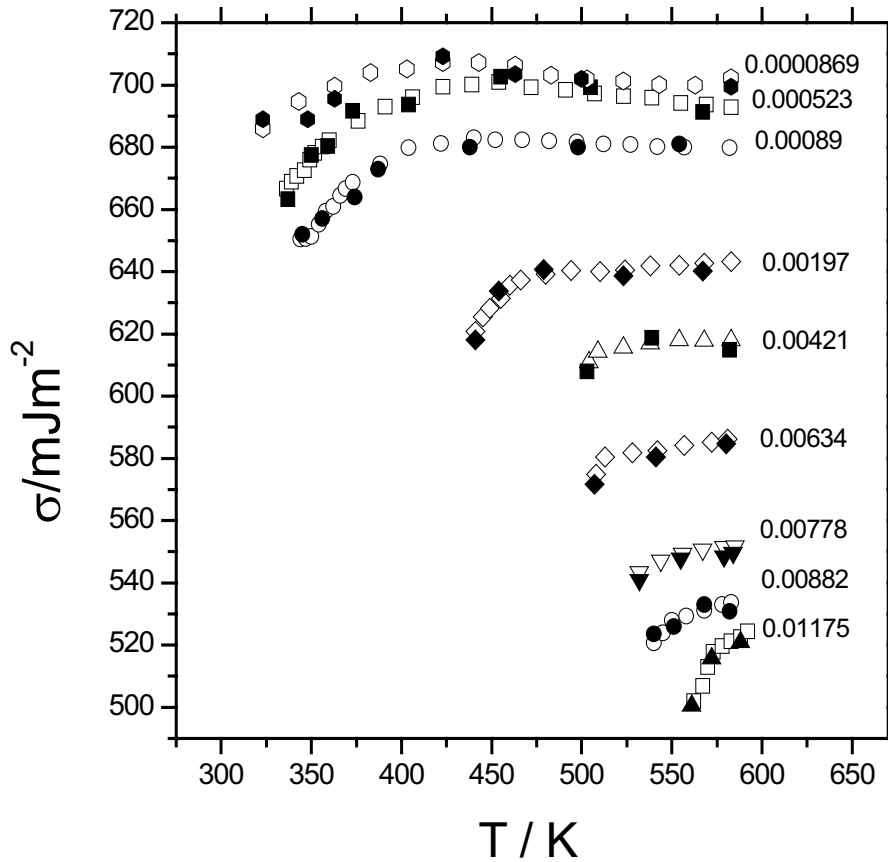


Figure 4.8. Temperature dependence of the surface tension of Ga-Pb alloys with $x_{Pb} = 0.0000869$ to 0.01175 from top to bottom in the graph. Solid symbols are taken on heating and open ones on cooling.

For $x_{Pb} \geq 0.00197$ in Ga-Pb alloys, slightly positive temperature coefficients of σ are found at high T . At a distance of 10-20 K above the phase boundary, kinks prevail in the slope of $\sigma(T; x_{Pb})$. This effect is visible e.g. for $x_{Pb} = 0.00197, 0.00421, 0.00634$ and 0.01175 , which indicates a jump in the surface excess entropy. This is a sign of a first order surface phase transition in the Ga-Pb system. An additional study on the temperature dependence of σ of the eutectic Ga-Pb liquid alloy approaching the liquidus line has been carried out to shed more light on the presence of a first order surface phase transition. It will be presented in a coming section.

A comparison of our data of the concentration dependence of σ with those available in the literature [15] is shown in Fig. 4.9 for three selected temperatures $T = 600, 550$ and 500 K. Solid symbols represent our data and open ones represent those of ref. [15]. The x-axis is plotted in a logarithmic scale. The solid line is to guide the eye. As

can be seen in Fig. 4.9, the agreement is poor at low temperatures (550 and 500 K). A difference of $\sim 40 \text{ mJm}^{-2}$ in σ is found for the same x_{Pb} . At 600 K there is a better agreement and the difference is only 20-25 mJm^{-2} . The data of this work exhibit a systematic deviation towards higher σ -values. Both data at 600 K are plotted in a separate figure for clarity, Fig. 4.10.

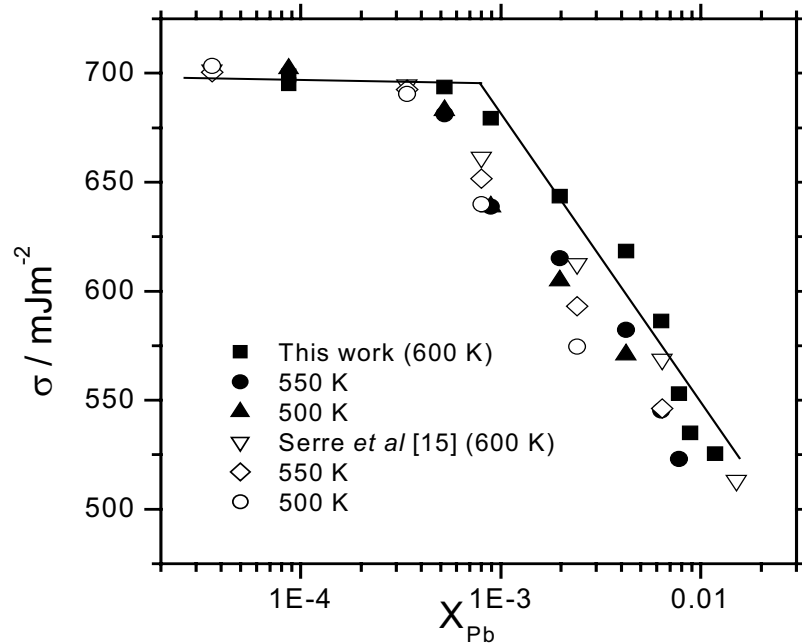


Figure 4.9. Surface tension σ of liquid Ga-Pb alloys vs Pb composition in mole fraction x_{Pb} plotted on a logarithmic scale at different temperatures, $T = 600, 550, 500 \text{ K}$; comparison of this work (solid symbols) with literature data (open symbols) of ref. [15]. The solid line is drawn to guide the eye.

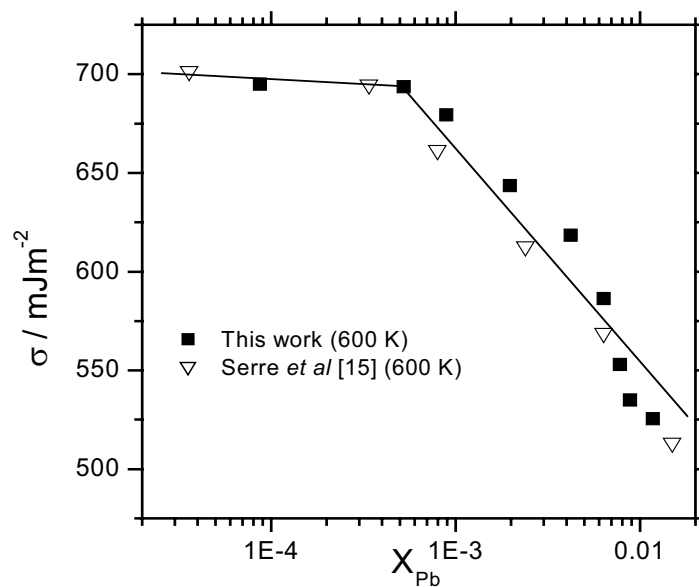


Figure 4.10. Surface tension vs Pb composition as in Fig. 4.9 at $T = 600 \text{ K}$, plotted separately for clarity. Description of the figure is the same as in Fig. 4.9. The lines are drawn to guide the eye.

Concerning the disagreement of our data with those of ref. [15] at low temperatures. It is interesting to point out that Serre *et al* have used the sessile drop method, the vacuum in both experiments is comparable of the order of $10^{-8} - 10^{-9}$ mbar (see chapter 3). Furthermore the same nominal metal purity of both Ga and Pb has been employed. However we have used an Ar-ion sputter gun for in situ sample surface cleaning, while this is not possible with the sessile drop method. We are not sure whether cleaning of the sample surface by sputtering is the only source of this discrepancy.

It is relevant here to say that from the phase diagram of Pb-PbO which is shown below in Fig. 4.11 [75], the PbO is a stable compound up to 599 K and it has a relatively high solubility of $\sim 10^{-4}$ in liquid Pb at the eutectic temperature of 599 K. This is almost an order of magnitude higher than in the corresponding Bi-system. Upon melting PbO dissolves in bulk Pb and since the surface tension of PbO is presumably less than that of pure Pb, it may segregate on the surface of Ga-Pb alloys leading to a lower surface tension. Upon heating a reduction of surface segregation of PbO is expected. This may explain the agreement found at higher temperature of our surface tension data with those of ref. [15].

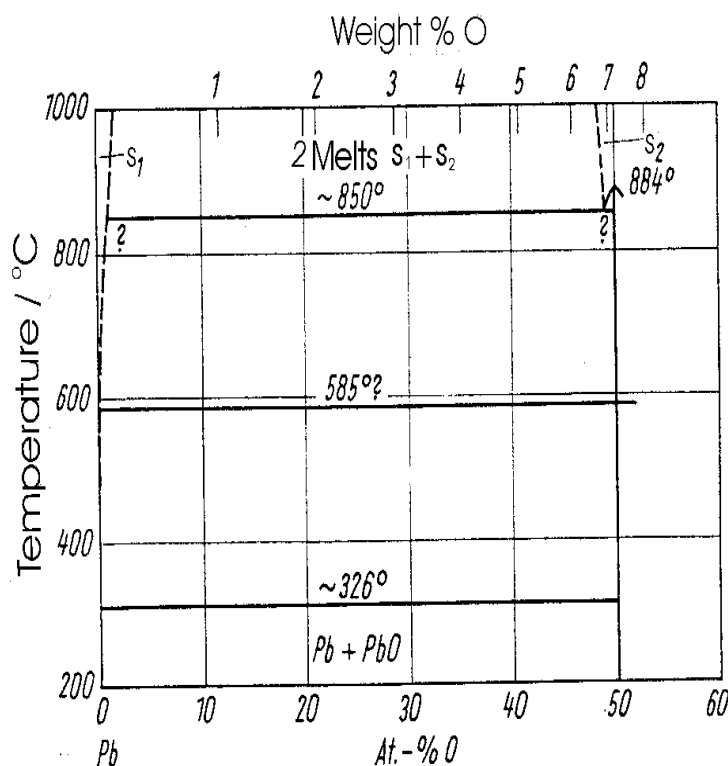


Figure 4.11. Temperature versus composition phase diagram of Pb-PbO taken from ref. [75]. Note the finite solubility of PbO in Pb at the eutectic temperature of 599 K.

4.3 Estimate of the viscosity of pure Ga, pure Bi, Ga-Bi and Ga-Pb liquid alloys

Capillary wave spectroscopy gives access to the viscosity of the liquid being studied (see equ. 2.6). In table 4b we give values of the viscosity at different compositions x_{Bi} and temperatures T determined from the half width of the spectra, where the latter was obtained with a relatively high confidence limit in the fits.

x_{Bi}	(T/K)	$\eta / \cdot 10^{-3} \text{N} \cdot \text{s} \cdot \text{m}^{-2}$
0	(303)	2.25 ± 0.22
0.0022	(303)	1.84 ± 0.16
0.03	(325)	1.95 ± 0.31
0.0505	(500)	1.98 ± 0.11
0.09	(500)	1.76 ± 0.4
0.612	(497)	1.89 ± 0.36
0.811	(545)	2.17 ± 0.2
1	(545)	2.3 ± 0.18

Table 4b Viscosity of liquid Ga-Bi alloys

Comparison of these data with results of the components from the literature is within the error bars satisfactory. The value of liquid Ga given in the literature [76] is: $2.1 \cdot 10^{-3} \text{N} \cdot \text{s} \cdot \text{m}^{-2}$ at the melting point, that for Bi is $2.07 \cdot 10^{-3} \text{N} \cdot \text{s} \cdot \text{m}^{-2}$. Within the experimental errors of our measurements for Ga-Bi, which range from 10% up to 20%, the viscosity exhibits no significant change. The error in the damping constant which is determined from the half width of the spectra showed in the worst cases an error in the range from 50% up to 70%, which is essentially due to the fact that the instrumental line broadening strongly influences the half width of the spectra. It can change with varying the alignment at different spectra recording.

Table 4c shows an estimate of the viscosity of some Ga-Pb liquid alloys at temperatures where the spectral half width could be determined with reasonable accuracy.

x_{Pb}	(T/K)	$\eta / \cdot 10^{-3} \text{N}\cdot\text{s}\cdot\text{m}^{-2}$
0.000523	(400)	3.31 ± 0.42
0.00089	(370)	2.52 ± 0.31
0.00197	(500)	1.44 ± 0.15
0.00421	(550)	3.1 ± 0.55
0.00634	(580)	2.58 ± 0.37
0.00778	(525)	4.2 ± 0.6
0.00882	(550)	4.64 ± 0.52
0.0175	(570)	3.8 ± 1.1

Table 4c. Viscosity of liquid Ga-Pb alloys

In the case of Ga-Pb liquid alloys there are no literature data on viscosity to compare with. However Earnshaw [77] made a capillary wave spectroscopic study on pure mercury and found a viscosity of $5.3 \cdot 10^{-3} \text{N}\cdot\text{s}\cdot\text{m}^{-2}$ about 3.5 times higher than the accepted value of $1.55 \cdot 10^{-3} \text{N}\cdot\text{s}\cdot\text{m}^{-2}$. Within the experimental errors of table 4c (10% up to 30%) the viscosity exhibits no significant change like in the case of the Ga-Bi liquid alloys. It was pointed out by Langevin [44] that the measured viscosity in a surface light scattering experiment is an average one over a distance comparable to the damping depth of the waves. The latter is of the order of q^{-1} .

4.4 Surface freezing in Ga-Bi and Ga-Pb liquid alloys

We start with presenting our results of light scattering measurements of surface freezing on Ga-Bi liquid alloys. Next, results will be presented for the eutectic Ga-Pb alloy. Measurements on the Ga-Bi alloys have been performed for $x_{Bi} = 0.0022$, 0.0073 and 0.0127 and at various wave numbers q ($200 \text{ cm}^{-1} \leq q \leq 660 \text{ cm}^{-1}$). Spectra of light scattered by interfacial waves have been recorded during various heating and cooling cycles at a constant rate of 8 K/h in the temperature range of the surface freezing transitions.

The liquid eutectic Ga-Bi alloy

Fig. 4.12 shows spectra of light scattered from the eutectic $\text{Ga}_{0.9978}\text{Bi}_{0.0022}$ liquid alloy surface at 343 K upon cooling for a sequence of wave vectors $q = 198.16$, 398.15 and 596.42 cm^{-1} in the same scattering pattern from left to right in the figure.

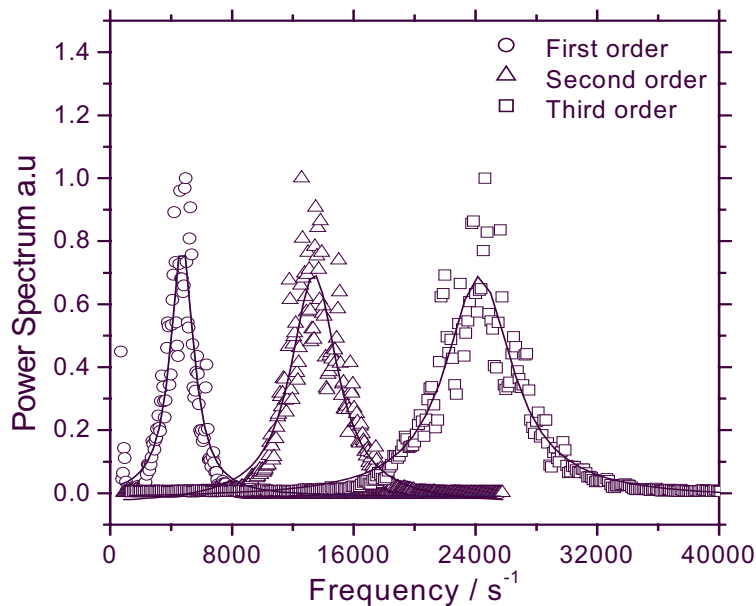


Figure 4.12. Quasi-elastic light scattering spectra of the eutectic Ga-Bi liquid alloy surface at $T = 343 \text{ K}$ recorded during cooling, $q = 198.16$, 398.15 and 596.42 cm^{-1} from left to right in the figure.

A sequence of spectra taken during heating is shown in Fig. 4.13 at $T = 318 \text{ K}$, $q = 214.9$, 430.2 and 645 cm^{-1} . Note the increase in the peak frequency and peak width with q . Fig. 4.14 shows the variation of the peak frequencies ω as a function of temperature at different q -values of the eutectic Ga-Bi alloy, $x_{eut} = 0.0022$. On cooling

ω drops at a temperature of $T_{sf} = 319 \pm 2$ K (T_{sf} refers to the temperature of surface freezing), an indication of structural changes at the surface. The transition temperature (T_{sf}) is directly comparable to the surface freezing temperatures reported in [12] determined previously in our laboratory by second harmonic generation. This jump in ω indicates that above T_{sf} we have a disordered bare liquid surface (liquid-

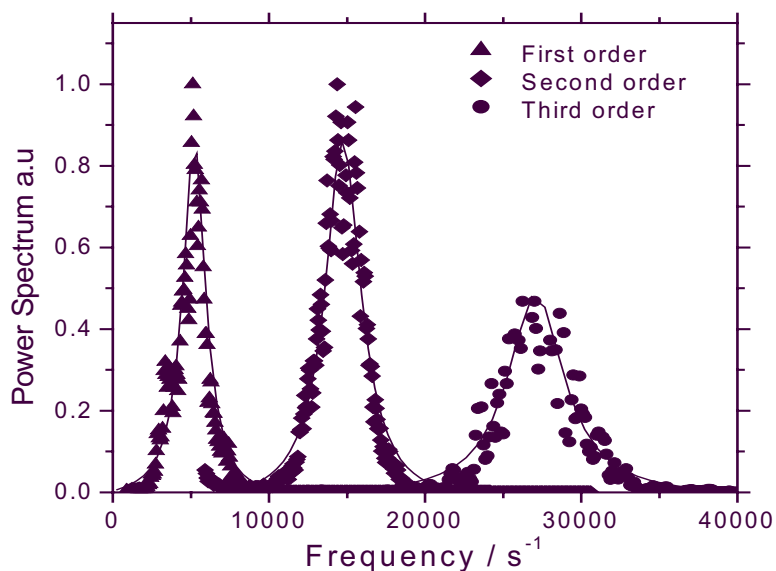


Figure 4.13. A sequence of spectra of light scattered from the eutectic Ga-Bi alloy surface at 318 K, $q = 214.9, 430.2$ and 645 cm^{-1} from left to right in the figure.

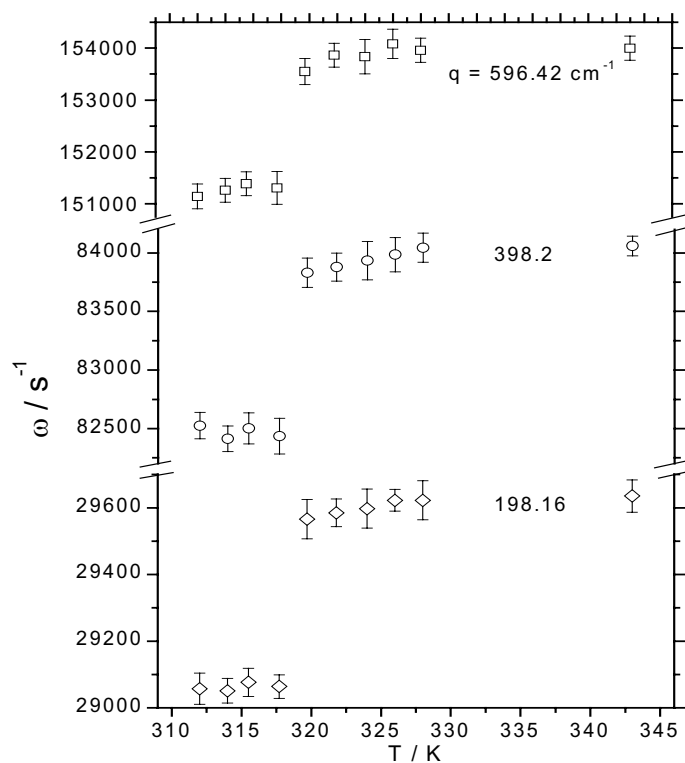


Figure 4.14. Temperature dependence of peak frequencies ω of thermally excited capillary waves in an eutectic liquid Ga-Bi alloy at various wave numbers q as shown in the figure.

like) while below it we have an ordered surface (solid-like) or surface freezing film of Bi on top of the bulk liquid alloy. Within experimental errors, ω stays constant as a function of temperature below T_{sf} . Above T_{sf} it increases slightly with T showing a similar behaviour to that in Fig. 4.4. The measurements above were reproduced in several heating and cooling cycles at the same heating or cooling rate as before but at different values of q . Unfortunately we could not reproduce the measurements above for the same x_{Bi} at the same values of q due to the fact that different optical alignments were required upon heating the sample to above the monotectic temperature after it was cooled down to a value near room temperature (see chapter 3). As a consequence each graph will be presented separately, except for Fig. 4.15 below which presents the outcome of the reproduction measurements during heating (solid symbols) and

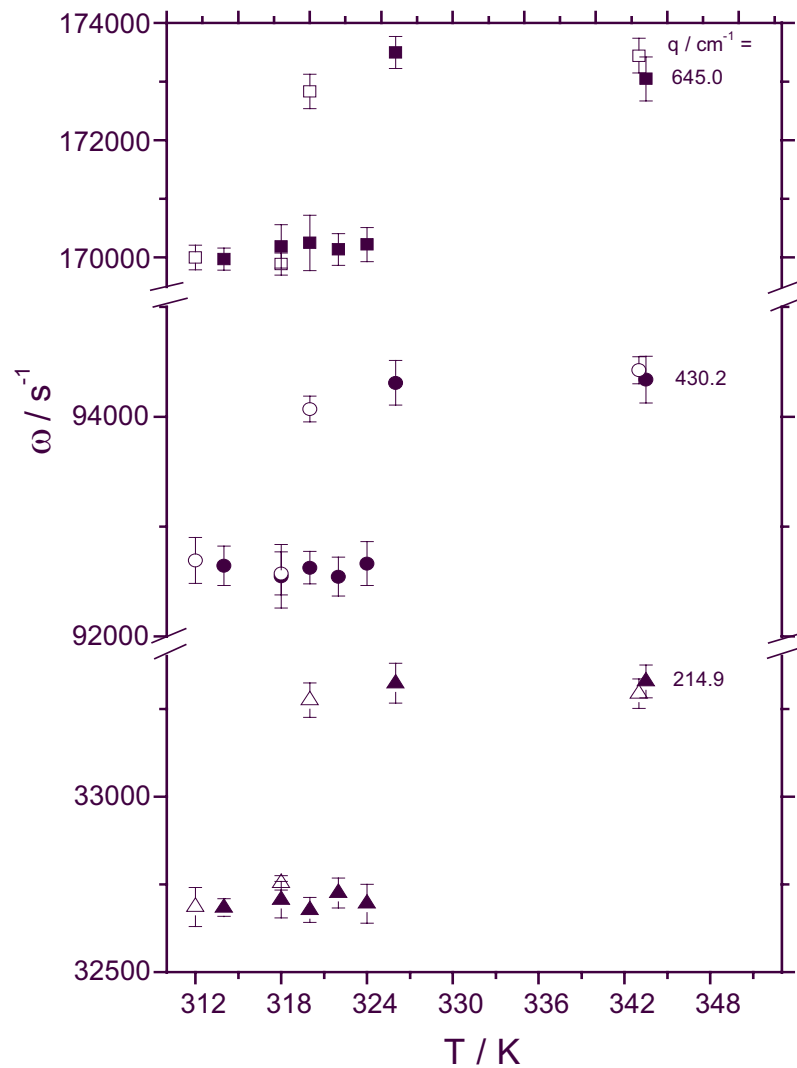


Figure 4.15. Temperature dependence of the peak frequencies ω of capillary waves in an eutectic liquid Ga-Bi alloy at various wave numbers q ; the open symbols correspond to measurements on cooling, full ones to heating.

cooling (open symbols) cycles simultaneously. As can be seen in Fig. 4.15, the same behaviour in Fig. 4.14 is retained where ω drops on cooling at the same temperature of $T_{sf} = 319 \pm 2$ K. Melting of the surface freezing film is signalled by a jump in ω near $T_{sm} = 325$ K (T_{sm} refers to the temperature of surface melting), which is again in agreement with that of ref. [12]. A remarkable hysteresis behaviour is clearly visible in the $\omega(T)$ -dependence. In both figures, Figs. 4.15 and 4.14, a simple $\omega \propto q^{3/2}$ obeys as expected according to equ. (2.6). The damping constant κ exhibits a similar discontinuous change as a function of temperature which is shown in Fig. 4.16. Solid symbols refer to heating and open symbols to cooling. The error bars are not shown for all data points for clarity. Although errors in κ are large, discontinuous changes across T_{sf} upon heating and cooling, are present.

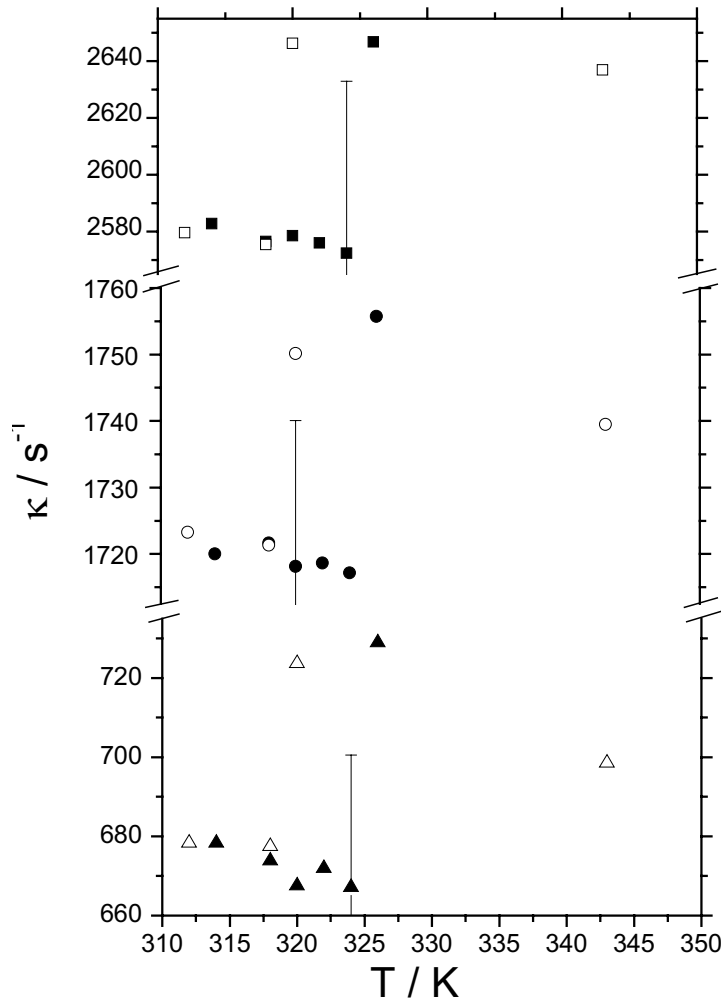


Figure 4.16. Temperature dependence of the damping constant κ of capillary wave in an eutectic liquid Ga-Bi alloy for the same values of q as in Fig. 4.15; open symbols represent measured points on cooling, solid ones on heating.

Finally, an interesting observation is the following: below 312 K, which is about 10 K above the eutectic temperature, no capillary waves have been detected. This possibly indicates that with further cooling the thickness of the surface freezing film increases to such an extent that capillary waves at the liquid-film interface are completely damped.

The jumps in ω and κ around T_{sf} are not artifacts of the experiment or data analysis but are reflected directly in the observed power spectrum as shown in Fig. 4.17. Note the increase in the peak frequency and half width of the spectrum above T_{sf} relative to that below T_{sf} . The increase in ω is about 2% while that of κ is about 7% as determined from the fit. Surface energies as determined from the above measured peak frequencies (Figs. 4.14 and 4.15) according to equ. (2.6) are summarized in Fig. 4.18.

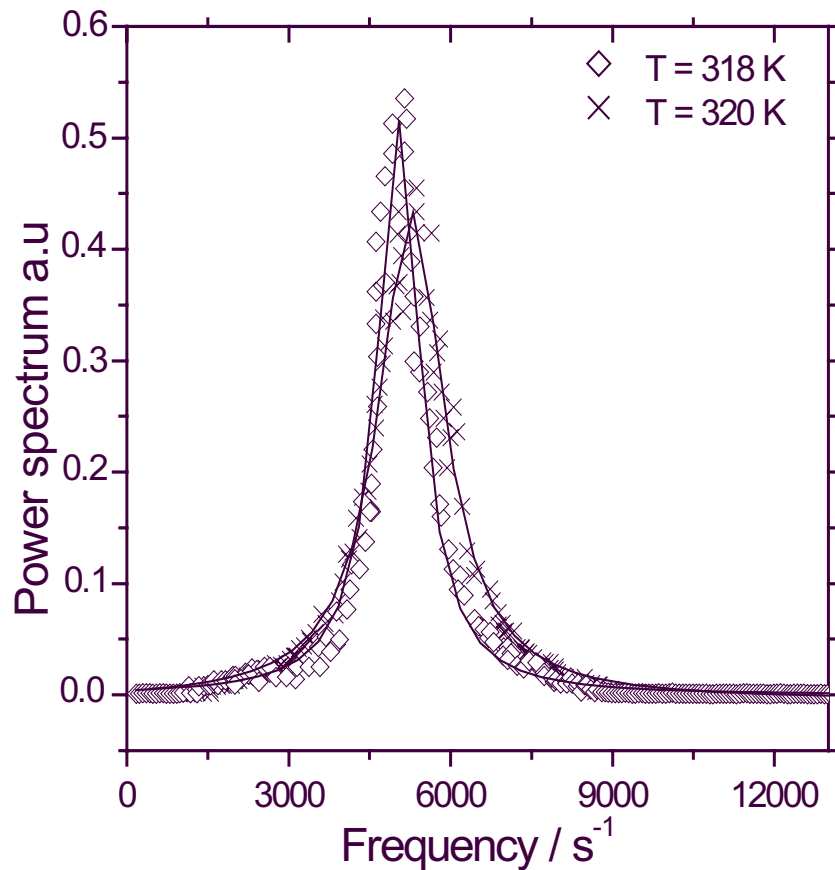


Figure 4.17. Power spectra of light scattered by a eutectic Ga-Bi liquid alloy surface, just below (left) and just above (right) T_{sf} as indicated in the figure. Both spectra were collected during a cooling cycle and $q = 214.9 \text{ cm}^{-1}$.

The surface tension values in Fig. 4.18 for $T > 323 \text{ K}$ agree with our previous measurements on the eutectic Ga-Bi alloy [78].

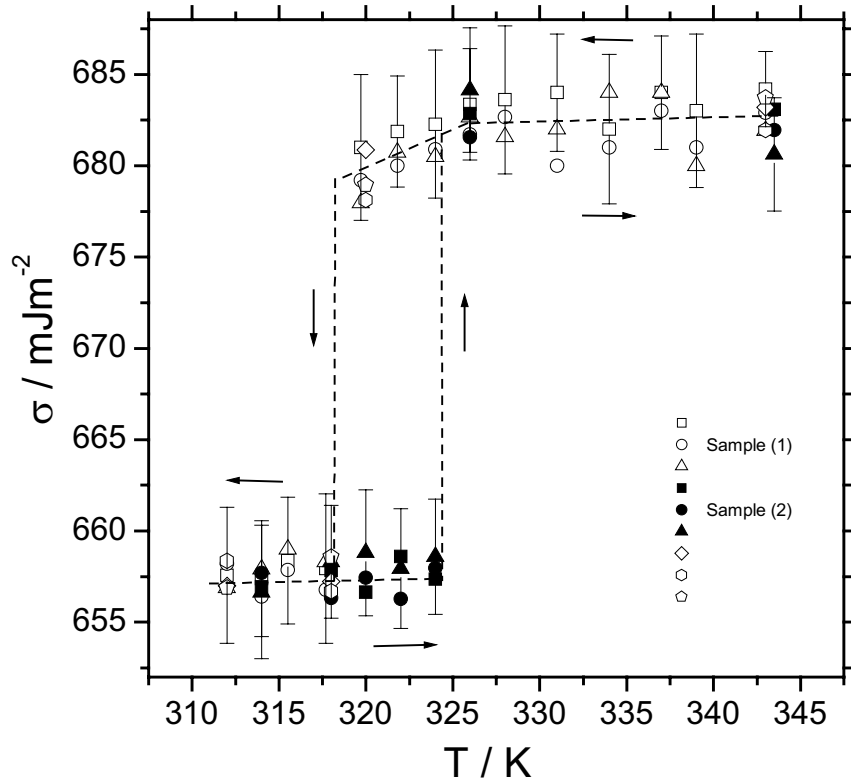


Figure 4.18. Temperature dependence and hysteresis behaviour of the surface tension of liquid eutectic Ga-Bi across the surface freezing temperature at 319 ± 2 K; open symbols refer to cooling, full ones to heating, the dashed lines are drawn to guide the eye; different symbols refer to separate measurements at different q -values.

The $Ga_{0.9927}Bi_{0.0073}$ liquid alloy

In order to study the composition dependence of the discontinuous changes and the hysteresis behaviour of ω and thus σ , measurements have been carried out at higher Bi concentrations relative to that of the eutectic composition. Fig. 4.19 shows the temperature dependence of the capillary wave frequencies in a liquid $Ga_{0.9927}Bi_{0.0073}$ alloy at different q -values as shown in the figure. Spectra were recorded during cooling at a cooling rate of 8 K/h. Reproduction of the data in Fig. 4.19 has been carried out during a heating cycle at the same heating rate as before but at different values of q and is shown in Fig. 4.20. It should be mentioned that the values of q shown in Fig. 4.20 are not a sequence of diffraction orders in the same diffraction pattern, e.g. $q_2 \neq 2q_1$. As can be seen in Figs. 4.19 and 4.20, ω drops on cooling at a temperature of $T_{sf} = 386 \pm 2$ K while on heating it jumps at $T_{sm} = 389 \pm 2$ K, again in agreement with the measurements in [12]. Spectra for this composition could not be

obtained below 383 K which is about 6 K above the liquidus temperature of 379 K according to the phase diagram (see Fig. 3.4).

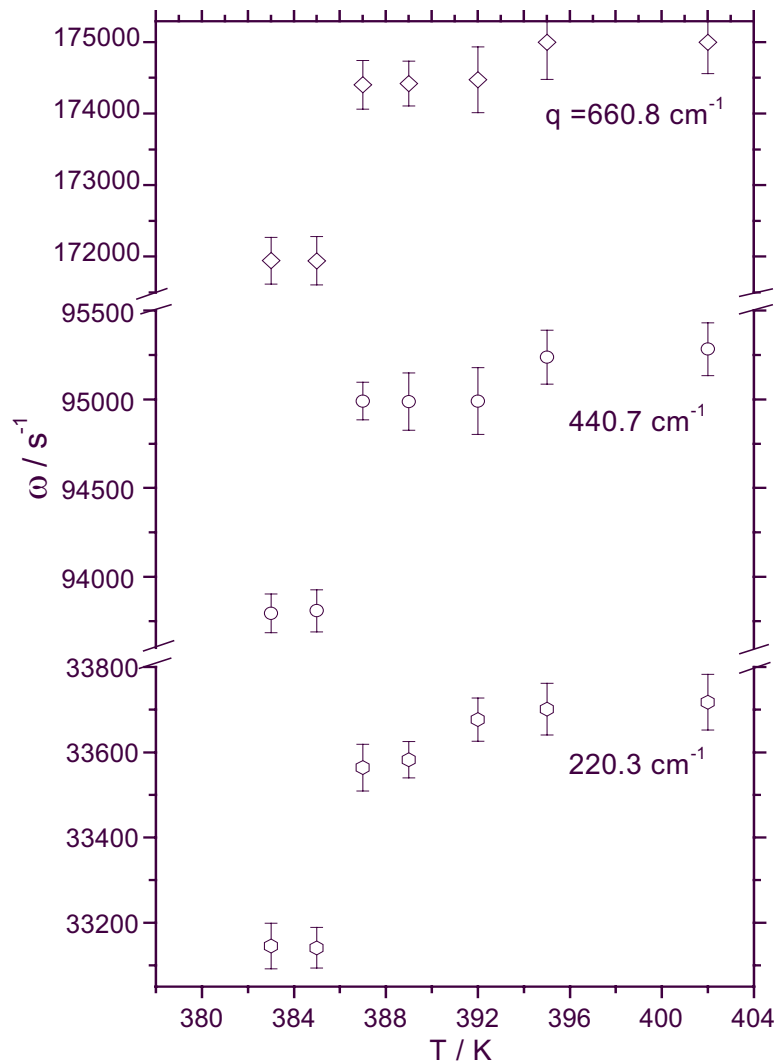


Figure 4.19. Temperature dependence of the capillary wave frequencies of the liquid $\text{Ga}_{0.9927}\text{Bi}_{0.0073}$ alloy at different q -values as shown in the figure. Measurements have been taken during cooling.

A hysteresis behaviour in the temperature dependence of the capillary wave frequencies is obvious in Figs. 4.19 and 4.20. The damping constants determined in the heating measurements (see Fig. 4.20) showed a similar hysteresis behaviour though not as clear as in the case of ω . This is shown in Fig. 4.21. The damping constants of the measurements on cooling did not show a similar behaviour but rather a large scattering in data points. In general the behaviour of the capillary wave damping is complex and many system parameters influence its behaviour e.g. surface

viscoelastic parameters [58, 79]. In addition, the thermal and mechanical instability of the liquid surface have been shown to have large influence on the damping constant [80].

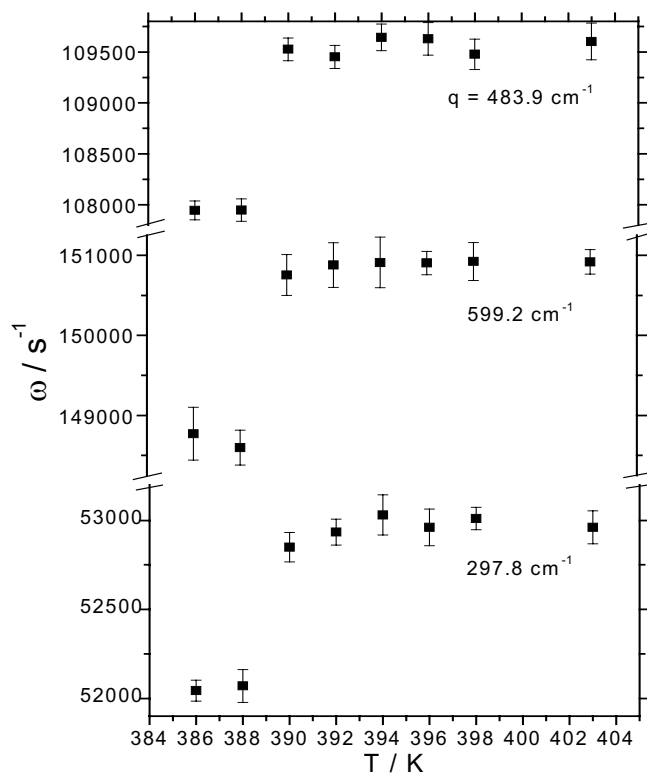


Figure 4.20. Temperature dependence of capillary wave propagation frequencies at the liquid $\text{Ga}_{0.9927}\text{Bi}_{0.0073}$ alloy surface. Measurements were taken during heating and for different values of q as shown in the figure.

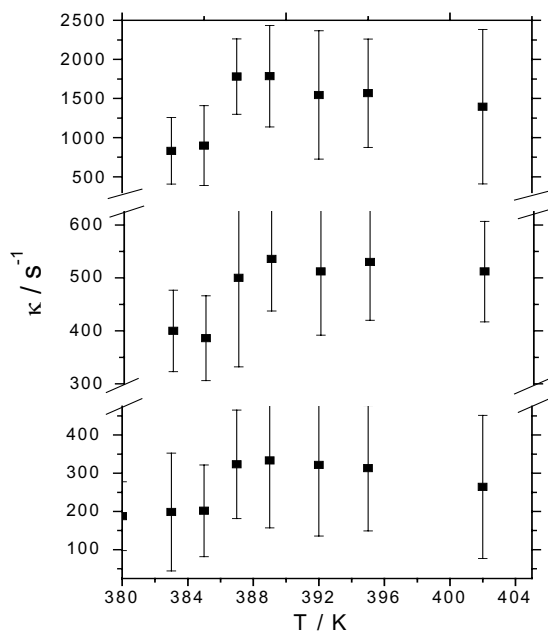


Figure 4.21. Temperature dependence of the capillary wave damping constant of the same measurements as in Fig. 4.20.

Surface tensions inferred from $\omega(T)$ measurements are shown in Fig. 4.22. In general the $\sigma(T)$ behaviour is similar to that in the previous measurements on the eutectic Ga-Bi alloy (see above).

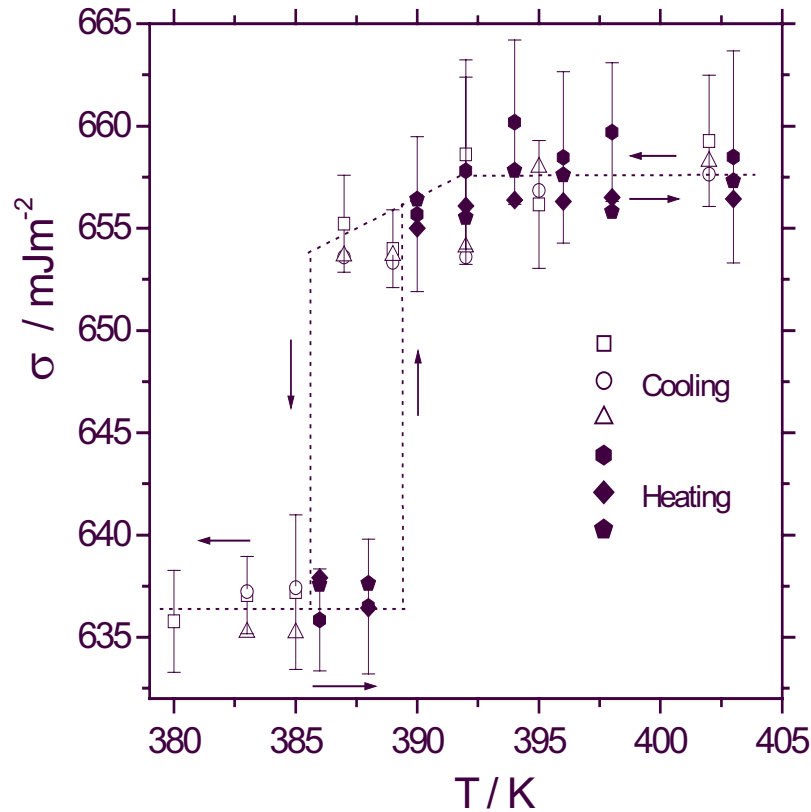


Figure 4.22. Temperature dependence and hysteresis behaviour of the surface tension of the liquid $\text{Ga}_{0.9927}\text{Bi}_{0.0073}$ across the surface freezing temperature at 386 ± 2 K; open symbols refer to cooling, full ones to heating. The dashed line is to guide the eye.

Ga_{0.9873}Bi_{0.0127} liquid alloy

Figure 4.23 shows the temperature dependence of the capillary wave frequencies at the $\text{Ga}_{0.9873}\text{Bi}_{0.0127}$ liquid alloy surface for different values of q as indicated in the figure. Measurements have been taken during cooling at a cooling rate of 8 K/h.

The outcome of measurements on heating at different values of q is shown in Fig. 4.24 below. Again the values of q shown in both Figs. (4.23 and 4.24) are not for the same sequence of diffraction orders in the same pattern. The distance between the diffraction grating and lens L3 (see chapter 3) could not be kept constant. On cooling ω drops at a temperature of 413 ± 2 K, in consistence with the surface freezing temperature of ref. [12]. In this case spectra could not be obtained below 410 K, which is about 7 K above the liquidus temperature according to the phase diagram.

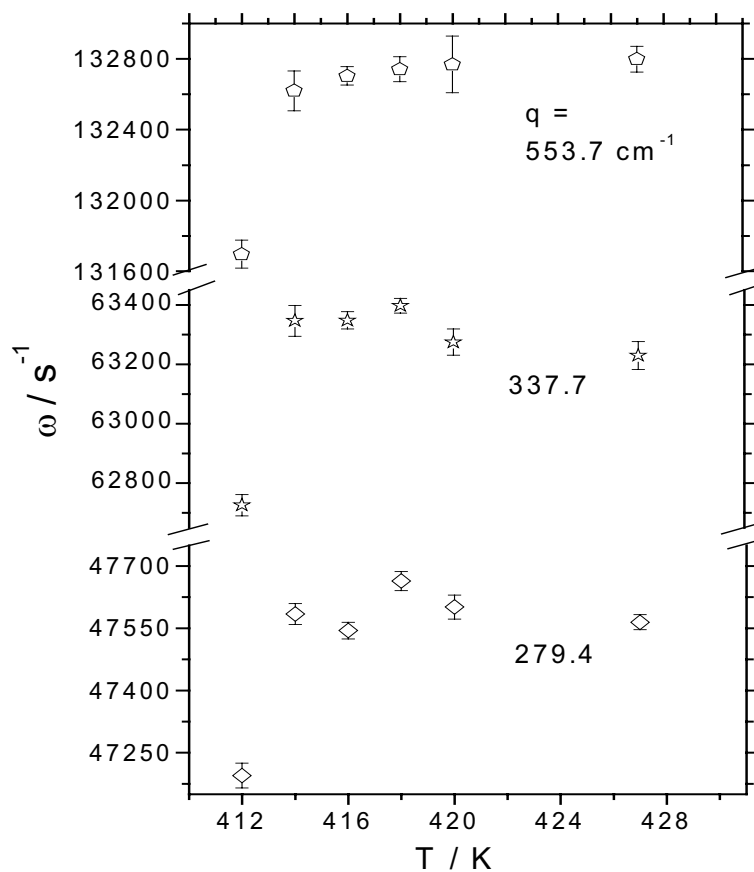


Figure 4.23. Temperature dependence of the capillary wave frequencies at the $\text{Ga}_{0.9873}\text{Bi}_{0.0127}$ liquid alloy surface for different values of q . Measurements were taken upon cooling at a cooling rate of 8 K/h.

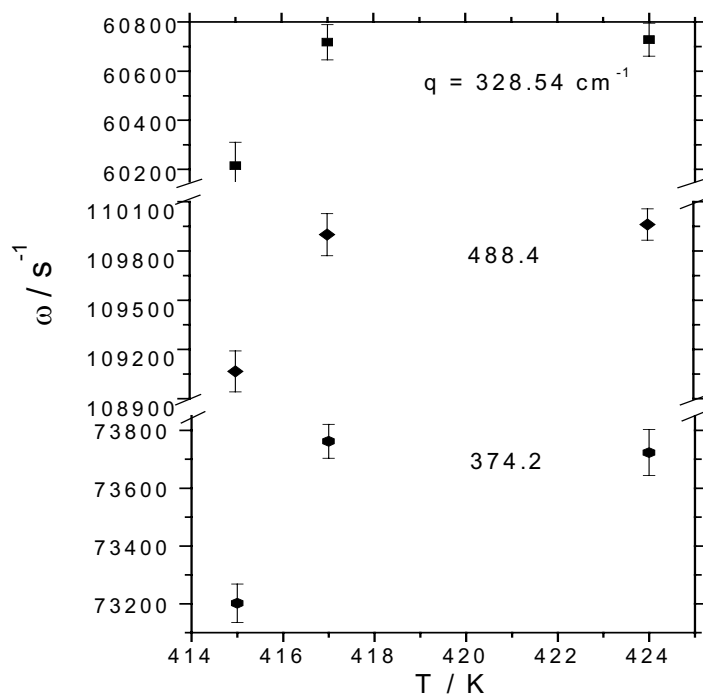


Figure 4.24. Temperature dependence of capillary wave frequencies at the $\text{Ga}_{0.9873}\text{Bi}_{0.0127}$ liquid alloy surface for different values of q . Measurements were taken during heating.

Upon heating ω jumps at a temperature of 415 ± 2 K, clearly exhibiting hysteresis behaviour. In the figures above, on cooling and heating, a simple $\omega \propto q^{3/2}$ dependence is obeyed as in the other measurements. In all our measurements on the temperature dependence of the capillary wave frequencies at temperatures below the surface freezing, ω stays constant within experimental errors. Above the surface freezing temperatures it increases slightly and reaches constant values. As for the temperature dependence of the capillary wave damping in the last measurements on the $\text{Ga}_{0.9873}\text{Bi}_{0.0127}$ liquid alloy, no clear conclusion can be drawn since there is too much scattering in the obtained data. The surface tensions as calculated from equ. (2.6) are shown in Fig. 4.25 below.

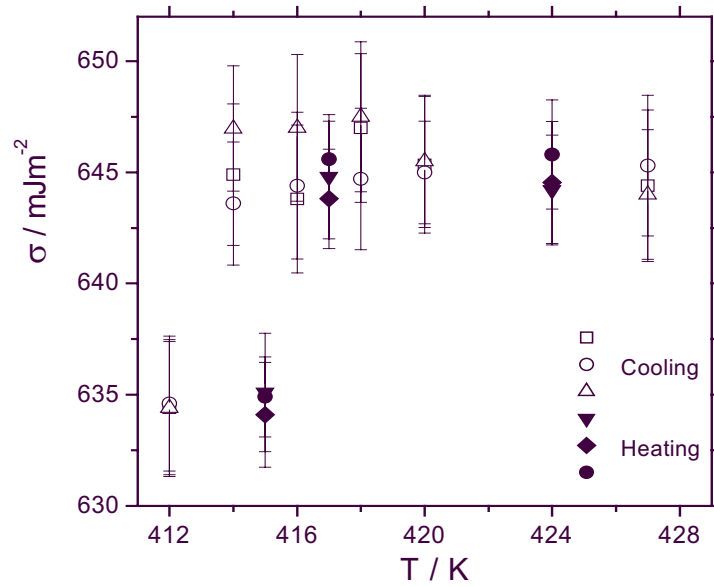


Figure 4.25. Temperature dependence and hysteresis behaviour of the surface tension σ of the liquid $\text{Ga}_{0.9873}\text{Bi}_{0.0127}$ alloy across the surface freezing temperature of 313 ± 2 K; open symbols refer to cooling, full ones to heating.

A summary of the observed drops and jumps in $\sigma(T)$ of the different Ga-Bi liquid alloys and the corresponding temperatures is given in table 4d:

x_{Bi}	Drop in σ / mJm^{-2}	$T_{sf} \pm 2/ \text{K}$	$T_{sm} \pm 2/ \text{K}$
0.0022	25.1	318	324
0.0073	17.4	386	390
0.0127	10.6	413	416

Table 4d. Summary of the observed drops and jumps in σ of the studied Ga-Bi liquid alloys and the corresponding temperatures, where T_{sf} is the surface freezing temperature and T_{sm} is the surface melting temperature.

Surface freezing in a eutectic Ga-Pb liquid alloy

Measurements on a eutectic Ga-Pb liquid alloy ($x_{eut} = 0.0006$) have been performed at various values of q and during different heating and cooling cycles in the same manner as in the case of the Ga-Bi liquid alloys. Fig. 4.26 shows the temperature dependence of the peak frequencies of capillary wave in a eutectic Ga-Pb liquid alloy. Measurements in Fig. 4.26 have been taken during a cooling cycle and at $q = 232.2$, 424.6 and 644.4 cm^{-1} from bottom to top in the figure. In Fig. 4.26 ω drops on cooling at a temperature of $T_{sf} = 357 \pm 2$ K.

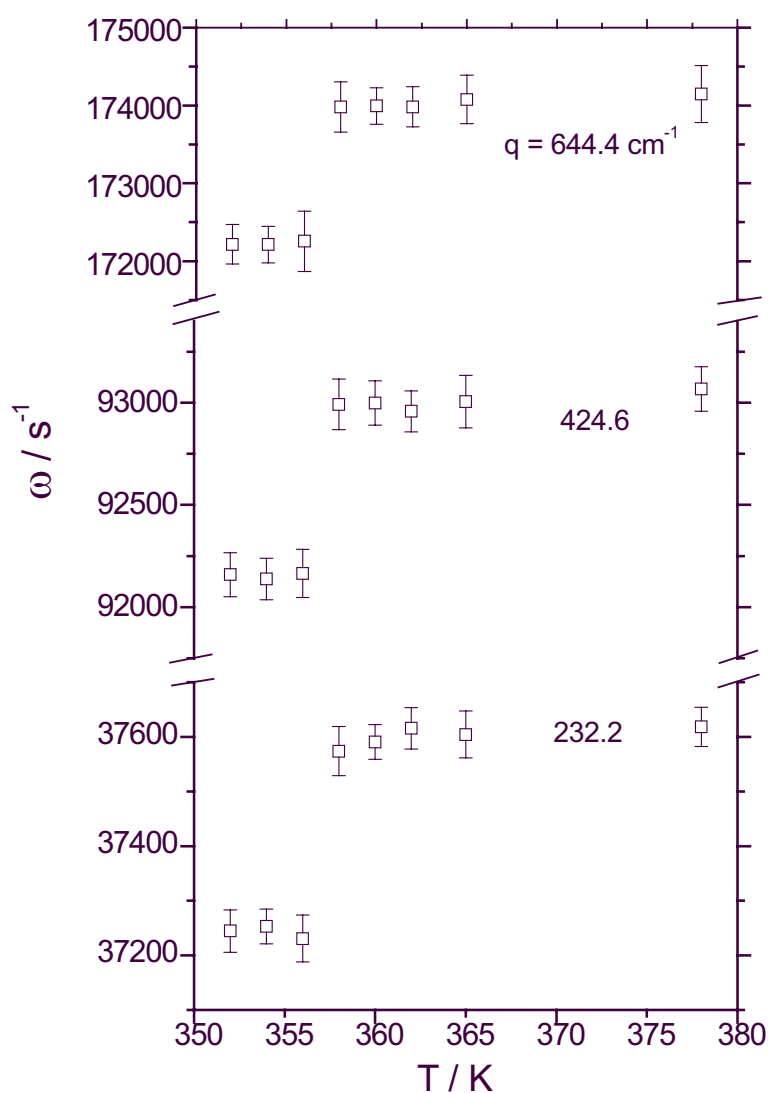


Figure 4.26. Temperature dependence of the peak frequencies ω of capillary waves in a eutectic Ga-Pb liquid alloy at various wave numbers $q = 232.2$, 424.6 and 644.4 cm^{-1} from bottom to top in the figure.

Spectra could not be obtained below 352 K, which is about 49 K above the eutectic temperature inferred from the phase diagram (see chapter 3). Measurements have been performed under the same conditions at different q -values during a heating cycle, the results are presented in Fig. 4.27. Melting of the surface freezing film is signalled by a jump in ω near $T_{sm} = 361 \pm 2$ K.

The surface free energy resulting from these $\omega(T)$ measurements is presented in Fig. 4.28. The magnitude of the drop in σ of the liquid eutectic Ga-Pb alloy is ~ 13 mJm $^{-2}$.

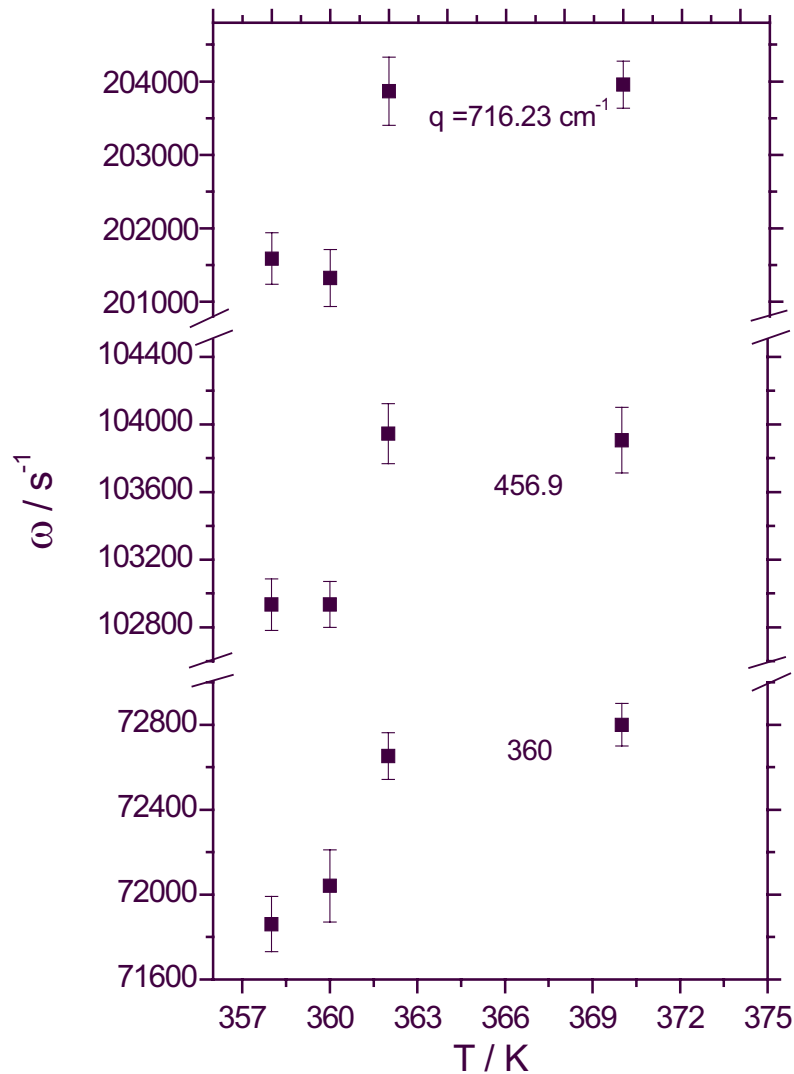


Figure 4.27. Temperature dependence of the peak frequencies ω of capillary waves in a eutectic Ga-Pb liquid alloy at $q = 360$, 456.9 and 716.23 cm $^{-1}$ as indicated in the figure. Measurements have been taken during heating.

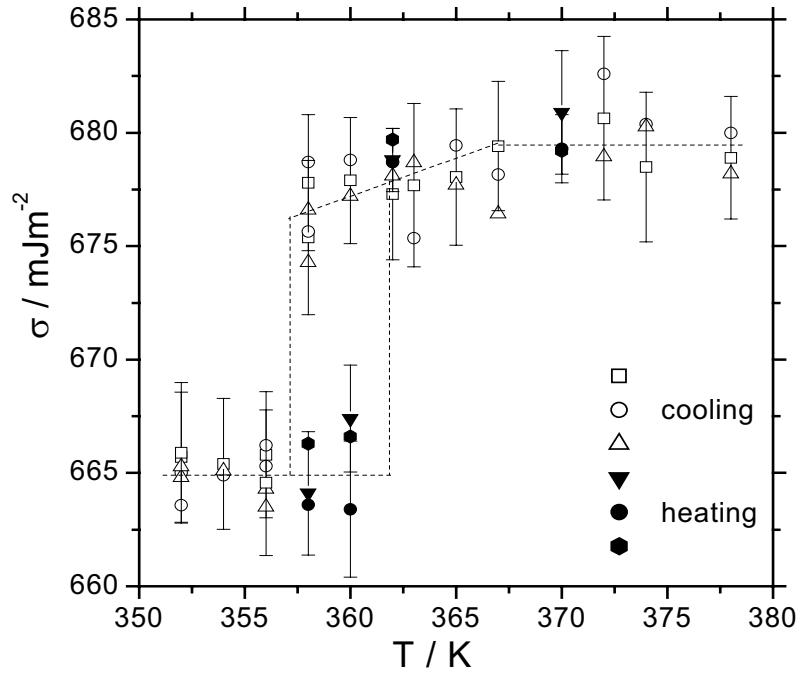


Figure 4.28. Temperature dependence and hysteresis behaviour of the surface tension of the liquid eutectic Ga-Pb alloy across the surface freezing temperature $T_{sf} = 356 \pm 2$ K; open symbols refer to cooling, full ones to heating.

The outcome of these difficult measurements on surface freezing in liquid Ga-Bi and Ga-Pb alloys show remarkable effects concerning the temperature dependence of the peak frequencies and the surface energy. These effects can be summarised as follows: approaching the surface freezing temperature from above, σ slightly decreases with temperature and drops at the transition by a value well outside the error of σ of ± 3 mJm⁻². The magnitude of the drop in σ depends on the composition of the low-tension component Bi or Pb as shown in table 4d. A negative surface entropy is indicated above the transition temperature e.g. for the eutectic Ga-Bi alloy a negative entropy is indicated in the temperature interval $318 \leq T / K \leq 325$. In a liquid mixture this can be due to the interplay of two effects, a reduction of surface segregation of the low-tension component Bi or Pb with increasing temperature and a decrease of σ of the pure component Bi or Pb with temperature [81]. On the other hand, the discontinuous change of the surface entropy is indicative of a first order surface phase transition from a bare liquid surface to an ordered surface layer, comparable to the hexatic phase discussed in Ga-Pb alloys [17]. A clear hysteresis is observed in the temperature dependence of σ around the transition temperature. The width of the hysteresis decreases with increasing Bi or Pb composition.

Chapter 5

Discussion

5.1 Anomalous behaviour of capillary wave damping in liquid metals and alloys

Our surface light scattering experiments on pure Ga, pure Bi and Ga-based alloys (Ga-Bi, Ga-Pb) show that capillary wave damping κ on the surface of these liquid metals and alloys exhibits anomalous behaviour. By anomalous behaviour it is meant that the experimentally determined damping constants are inconsistent with the predictions of the dispersion equation (see equ. 2.4). Fig. 5.1 shows the wave number q dependence of the capillary wave damping on the surface of pure liquid Ga, the full symbols refer to experimentally determined κ , the dashed line represents the theoretical predictions according to the dispersion equation using accepted values of the viscosity [76] and density [63] of pure Ga.

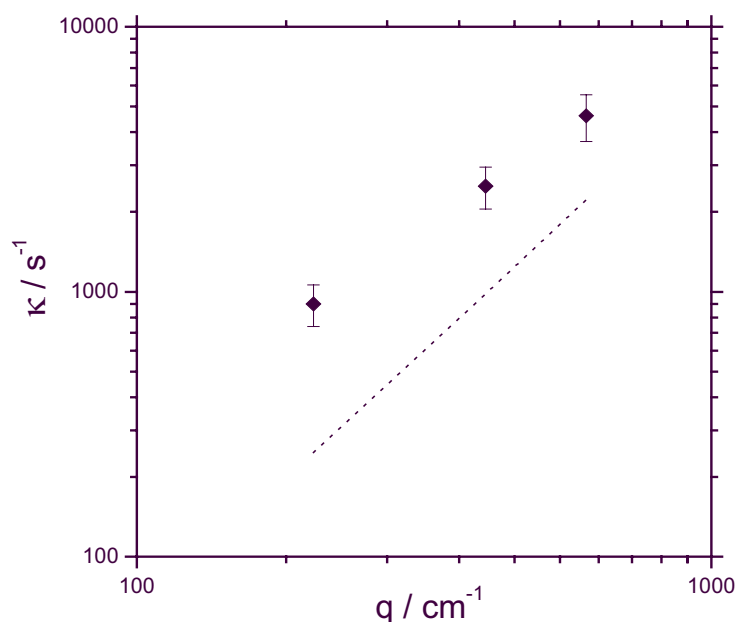


Figure 5.1. Wave number dependence of the capillary wave damping on the surface of pure liquid Ga, for description of the data see text.

As can be seen in Fig. 5.1, the observed damping constants including errors (20% - 25%), deviate largely from the prediction of the dispersion equation for a bare liquid

surface. Surface light scattering experiments on liquid metals, so far only on liquid Ga and Hg [58, 77, 79, 80], have shown that capillary wave damping exhibits anomalous behaviour both as a function of wave number and temperature. Fig. 5.2 shows the temperature dependence of the capillary wave damping on the surface of pure Ga at $q = 431.3 \text{ cm}^{-1}$ determined in this work.

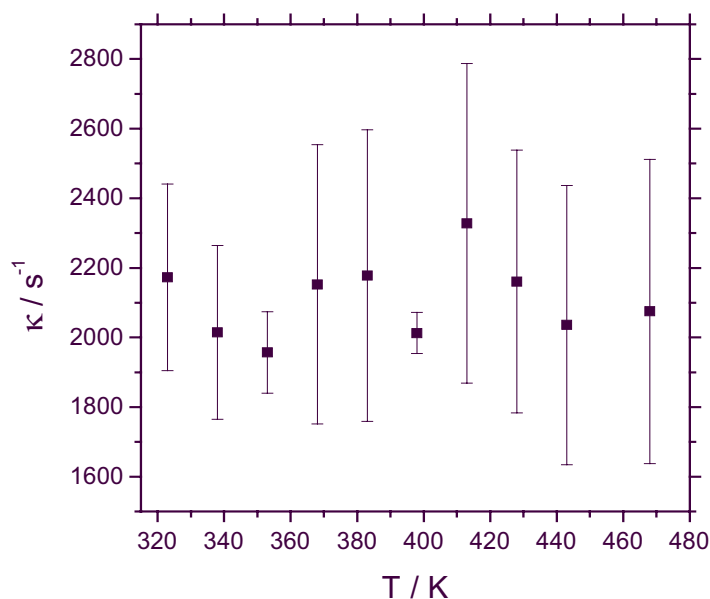


Figure 5.2. Temperature dependence of capillary wave damping on the surface of pure liquid Ga.

To our knowledge no surface light scattering experiments have been carried out on the temperature dependence of capillary wave frequency and damping constant in liquid metal alloys. Earnshaw [77] studied the wave number dependence of capillary wave frequency and damping constant on the surface of pure mercury by capillary wave spectroscopy. He found out that while the capillary wave frequency exhibits usual behaviour, the damping constant behaves anomalously. Earnshaw has pointed out that attempts have been made to explain the observed anomalous behaviour in case of the damping constant in terms of the interfacial viscosities (see chapter 2) possessed by a fluid interface. These interfacial viscosities have been shown to modify the propagation of capillary waves upon the interface [77]. He mentioned that the great anomaly of the capillary wave damping on the mercury interface cannot be explained only in terms of these interfacial viscosities, but that other effects are significant for liquid metals. These effects arise from the suggestion [82-83] that a layering structure

exists in the surface density profile and a partial monolayer of metal atoms forms at the surface. These atoms are neither metallic nor vapour like. Their existence is due to the effective confinement of the ions by the conduction electrons. Earnshaw suggested that this monolayer would be compressible and thus may be expected to possess elasticity different from zero. In his analysis, he compared the measured damping constants to the theoretical predictions based on the modified dispersion equation, which takes into account the mentioned interfacial viscosities, and found that neither of these viscosities can account for the observed anomalous behaviour. However, incorporation of a non-zero surface elasticity in the hydrodynamic theory effects κ dramatically. It has to be mentioned that incorporation of the surface viscoelasticity in the hydrodynamic theory complicates the dispersion equation, making it difficult to be solved analytically. This was also pointed out by Earnshaw. Therefore his analysis was based on the numerical solution of the dispersion equation.

Another study [80] on the wave number dependence of capillary wave damping on the surface of pure liquid Ga showed that κ exhibits anomalous behaviour as in the case of Hg. A numerical solution of the modified dispersion equation yielded better consistency with the measured damping constants. The author explained the observed anomalous behaviour and the drastic changes in κ upon inclusion of the surface viscoelastic parameters by the same reasoning as in [77].

An independent study [58] on the temperature dependence of κ on the surface of Hg has shown the same behaviour as mentioned above, again the same interpretation was adapted. However, in [58] it was found out that mechanical vibrations could be one of the sources of the observed large errors in κ . This is understandable since vibrations can shift the wings of the light scattering spectra producing large errors when fitting to the theoretical spectrum is made.

Another factor influencing the capillary wave damping is the instrumental broadening, which depends inter alia on the optical alignment. It has been mentioned in chapter 3 that the optical alignment could not be kept constant due to a change in the surface curvature of the liquid metals and alloys surfaces upon heating or cooling, which leads to a change in q . This influences the instrumental broadening drastically and as a consequence changes the capillary wave damping. Finally, it should be stressed here that in all the studies mentioned above the viscoelasticity of the surface has had small effects on the peak frequency.

5.2 Wetting and prewetting transitions in liquid Ga_xBi_{1-x} and Ga_xPb_{1-x}

The measured surface tension and its temperature coefficient give direct information on the surface thermodynamic properties of the system: the surface energy σ and the surface entropy $S^\sigma = -d\sigma/dT$, where the values of these quantities are taken per unit area of the surface. In what follows we discuss these quantities as a function of composition and temperature, but will focus on the Ga-rich alloys. We first consider the phenomenological surface thermodynamic aspects and subsequently, in order to link up with the X-ray structural investigations, discuss the monolayer and the multilayer models (will be introduced in sections 5.2.3 & 5.2.4) in relation with the surface thermodynamic functions. Finally, we will give an estimate of the thickness of the interfacial region from the change of the relative surface entropy.

5.2.1 Surface excess entropy and its dependence on x_{Bi} or x_{Pb}

We first discuss the surface excess entropy for the Ga-Bi system and subsequently for the Ga-Pb system. From the linear fits of the temperature dependence of the surface tension in the homogeneous phase region (see Fig. 4.4), the temperature coefficients $(d\sigma/dT)_{Bi}$, together with the error bars are shown in Fig. 5.3.

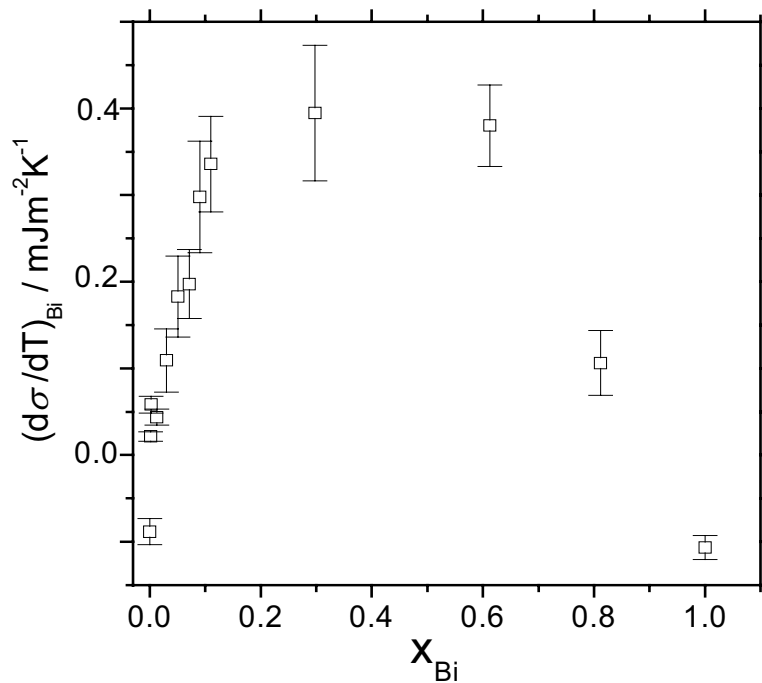


Figure 5.3. Temperature coefficients of the surface tension of Ga-Bi alloys taken from the linear fits in Fig. 4.4 plotted as a function of bulk Bi mole fraction. The error bars represent the errors from the linear fits and the errors in the surface tension.

The error bars shown in Fig. 5.3 represent the errors from the linear fits and the errors in the surface tension. The composition range in the figure starts with pure Ga and ends at pure Bi. An interesting observation is that the temperature coefficient of the surface tension increases nearly linearly with x_{Bi} between the eutectic and monotectic point. Above the monotectic composition it flattens near a value of $(d\sigma/dT) \sim (0.35 \pm 0.06) \cdot 10^{-3} \text{ Jm}^{-2}\text{K}^{-1}$. This gives an interesting insight into the structural changes of the liquid-vapour interface. The temperature coefficient of the pure components (Ga and Bi), as briefly mentioned in chapter 4, is negative, implying a positive relative entropy. While the $d\sigma/dT$ of all studied liquid Ga-Bi alloys is positive as is seen in Fig. 5.3, this implies a negative relative entropy. Concerning the positive entropy of the pure components, generally speaking, according to the lattice model a positive entropy can be accounted for by considering the decrease in the frequency of vibration along the direction normal to the surface. In other words the surface atoms have greater freedom of movement than the atoms in the bulk [38]. In case of the liquid Ga-Bi alloys, the observed negative entropy indicates structural changes at the bare liquid-vapour interface. These structural changes are due to segregation of the low tension component Bi at the liquid-vapour interface. If the latter remained free of Bi, meaning that no segregation has taken place, then the observed entropy would be positive as it is for pure liquid Ga at $T \sim 70 \text{ K} > T_m$.

Although a number of studies on the temperature dependence of the surface tension of liquid metal alloys Ga-Bi and Ga-Pb, measured by the sessile drop method, do exist [15, 71], no attempt was made to extract information on the surface excess entropy of these alloys. In fact a positive $d\sigma/dT$ is clearly visible in these measurements for both Ga-Bi and Ga-Pb. A negative surface excess entropy and a linear dependence on chain length has been reported for liquid normal alkanes [22]. The authors studied the temperature dependence of the surface tension of a series of n-alkanes ranging from pentadecane to octadecane. An inversion of the surface tension with temperature near some temperature which the authors called T_k has been observed. Below T_k the surface tension increases linearly with temperature while above T_k it decreases with temperature. As a consequence a negative surface excess entropy is indicated below T_k and a positive one above it. The authors interpret the observed negative entropy by the presence of a thicker surface layer below T_k relative to conditions above T_k . So the layer thickness has decreased with increasing temperature. The surface layer thickness

was roughly estimated from the surface excess entropy of a liquid alkane surface above T_k . We are aware of the fact that our system considered here (Ga-Bi liquid alloy) is different in the type of bonding and interatomic interactions. Nevertheless the correlation made between the changes in surface excess entropy on one hand and interfacial structural changes and thus surface layer thickness changes on the other hand in alkane systems, can also be applied here. From what is mentioned above, it can be concluded that the surface layer thickness has increased upon Bi segregation at the bare liquid-vapour interface, which explains the negative surface entropy of the Ga-Bi liquid alloys. This point will become even more evident when we give an estimate of the thickness of the surface region and its dependence on x_{Bi} from the measured $d\sigma/dT$ and the entropy per unit area of the surface region calculated using a multilayer model in a subsequent section.

Concerning the Ga-Pb liquid alloys, the temperature coefficients of the surface tension were extracted in the same way as for the Ga-Bi alloys and are shown in Fig. 5.4 including the error bars. As already mentioned in chapter 4 the measurements have been concentrated in the Ga-rich region of the phase diagram, where wetting and prewetting transitions prevail. The error bars are due to errors from the linear fits of the temperature dependence of the surface tension in the homogenous phase region in Fig. 4.8 and the error in the surface tension.

As it is clear from Fig. 5.4, $(d\sigma/dT)_{x_{Pb}}$ increases nearly linearly within errors with Pb concentration in the bulk. For $x_{Pb} < x_{eut}$, $(d\sigma/dT)_{x_{Pb}}$ is negative while for $x_{Pb} > x_{eut}$ it is positive. A positive surface excess entropy is found in the former case and a negative one in the latter case. It was mentioned in chapter 4 that for $x_{Pb} < x_{eut}$, $\sigma(T)$ exhibits a somewhat similar behaviour to that of pure liquid Ga, meaning a positive temperature coefficient at low temperatures and a negative one at high temperatures (see Fig. 4.8), distinct from Ga-Bi liquid alloys, where all $d\sigma/dT$ are positive. It is worth mentioning that the eutectic composition of the Ga-Bi is about 3.5 times higher than the eutectic composition of the Ga-Pb liquid alloy.

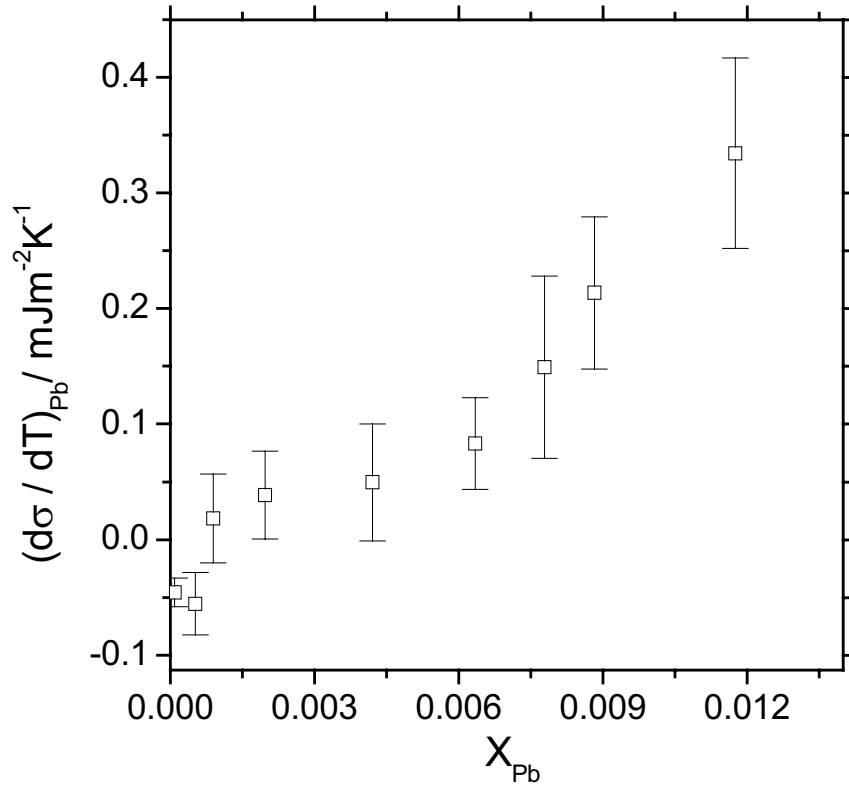


Figure 5.4. Temperature coefficients of the surface tension of Ga-Pb alloys extracted from linear fits to the data in Fig 4.4 in the homogenous phase region plotted as a function of bulk Pb mole fraction. The error bars represent the errors from the linear fits and the errors in the surface tension.

If we take into account that the adsorption of the more dense low surface tension component at the bare surface of the less dense high surface tension component decreases with increasing temperature [15], then it can be anticipated that at high temperatures in the case of the Ga-Pb liquid alloys for $x_{Pb} < x_{eut}$, the surface layer thickness decreases by a larger amount in comparison to Ga-Bi liquid alloys for $x_{Bi} < x_{eut}$ due to the lower amount of Pb in the bulk of the alloy and therefore at the surface. Unfortunately there is no simple direct relation between bulk and surface concentration to tell how much of Bi or Pb is present at the surface for a certain bulk concentration of each. Based on the monolayer model [84], which will be introduced in a subsequent section:

$$\sigma_{alloy} = \sigma_{PC} + \left(\frac{RT}{A} \right) \ln \frac{x^m}{x_b}. \quad (5.1)$$

where σ_{alloy} is the surface energy of the liquid alloy, σ_{PC} is the surface tension of the pure component Bi or Pb, A is the molar area, x^m denotes the mole fraction of the

segregated component in the monolayer, x_b that in the bulk and R is the gas constant. One can roughly estimate that at $T = 500$ K and for $x_{Bi} = 0.00135 < x_{eut}$, $x_{Bi}^m = 0.194$ in the case of Ga-Bi alloy while for $x_{Pb} = 0.000523 < x_{eut}$, $x_{Pb}^m = 0.022$ for the Ga-Pb alloy. These values were obtained using the measured surface energies of the alloys and pure Bi at 500 K (see Figs 4.4 and 4.8). The surface tension of pure Pb was taken from the literature [15], $A_{Bi} = 6.6 \cdot 10^4 \text{ m}^2 \text{ mol}^{-1}$, $A_{Pb} = 5.93 \cdot 10^4 \text{ m}^2 \text{ mol}^{-1}$. From these simple estimates it can be seen that at high temperatures e.g. 500 K, the amount of adsorbed Bi at the liquid-vapour interface largely exceeds that of Pb and since the surface layer thickness is proportional to surface coverage, this may explain the observed negative slopes for $x_{Pb} < x_{eut}$ at high temperatures. It is said above that the monolayer model gives rough estimates of the surface relative adsorption from the bulk concentration. This is because, as we will show later on, the monolayer model is inconsistent with Gibbs adsorption equation.

5.2.2 Analysis of the concentration dependence of σ according to the Gibbs adsorption equation

We start with the Gibbs adsorption isotherm of the Ga-Bi liquid alloys. For a plane surface of the liquid Ga-Bi alloy at equilibrium the surface energy σ is governed by the Gibbs equation (see also equ. 2.2):

$$d\sigma = -s_r^\sigma dT - \Gamma_{Bi} d\mu_{Bi}. \quad (5.2)$$

Here $s_r^\sigma = -(\partial\sigma/\partial T)_{\mu_{Bi}}$ is the relative surface entropy and $\Gamma_{Bi} = -(\partial\sigma/\partial\mu_{Bi})_T$ is the relative adsorption or surface excess of Bi. In equ. (5.2) all quantities are independent of the choice of the Gibbs dividing surface and so we may choose $\Gamma_{Ga} = 0$. In order to determine Γ_{Bi} from equ. (5.2) at $T = const$, we need the chemical potential μ_{Bi} . Since measurements at different concentrations in the Ga-rich melts are not known, we use an approximation by the regular solution model:

$$\mu_{Bi}^r = \mu_{Bi}^o + RT \ln x_{Bi} + 2RT_C (1 - x_{Bi})^2. \quad (5.3)$$

where μ_{Bi}^o is the chemical potential of the pure component Bi and $T_c = 535$ K is the critical temperature of the Ga-Bi system – see Fig. 3.4. A plot of the Gibbs adsorption isotherms is given in Fig. 5.5 with $\Delta\mu_{Bi}^r = \mu_{Bi}^r - \mu_{Bi}^o$.

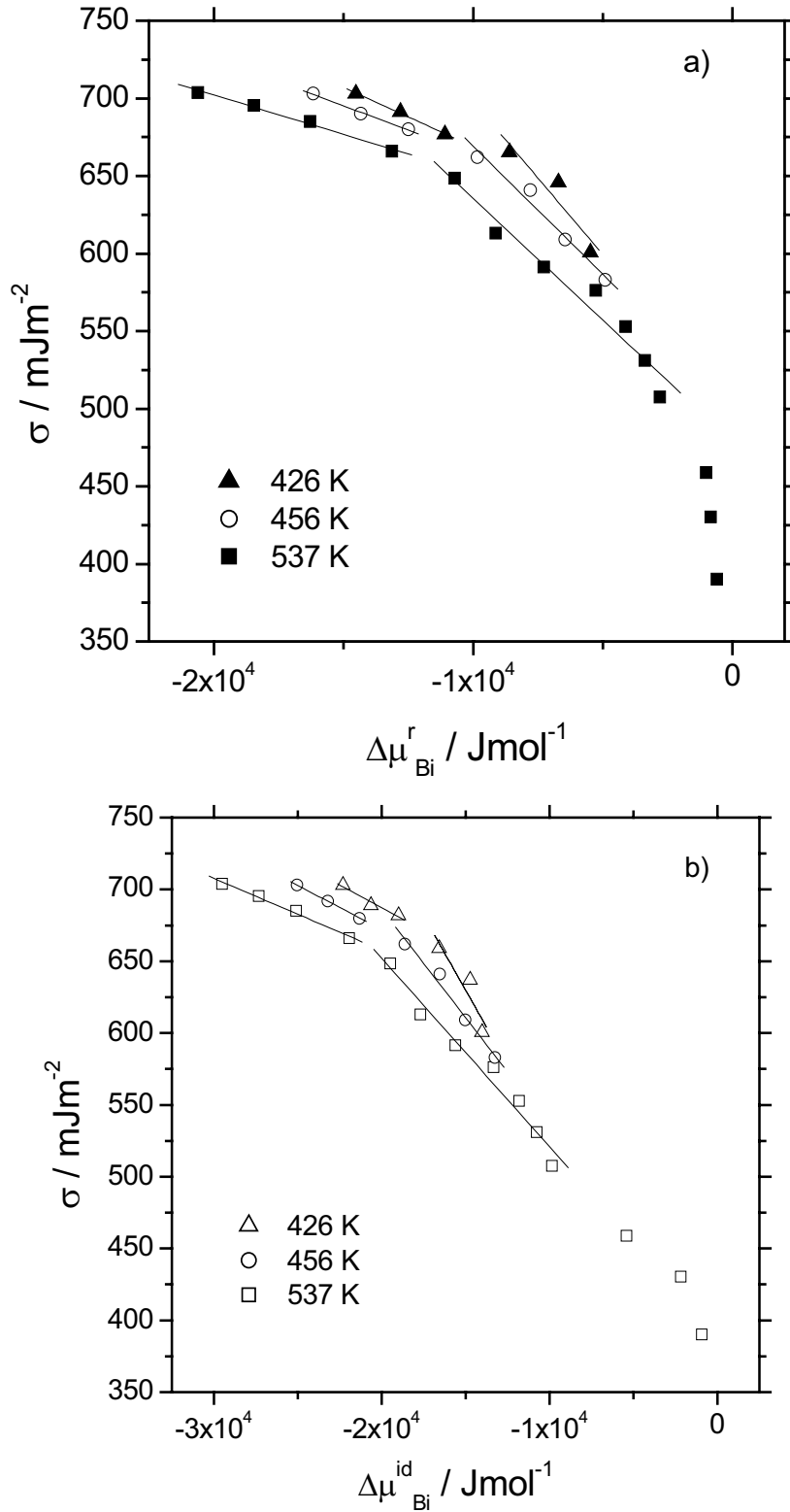


Figure 5.5. a) Gibbs adsorption isotherms of liquid Ga-Bi alloys: plotted is the surface energy vs the chemical potential according to the regular solution model approximation. b) shows a corresponding plot with $\Delta\mu_{\text{Bi}}^{\text{id}}$ for the ideal solution model. The solid lines are linear fits to the data for $0.00135 \leq x_{\text{Bi}} \leq 0.00734$ and for $0.0126 \leq x_{\text{Bi}} \leq 0.11$ at $T = 537, 456, 426$ K.

It contains several interesting observations. First, at a constant temperature near T_c and 80 K and 109 K below, the surface energy decreases linearly with $\Delta\mu_{Bi}^r$ over a concentration range of about $10^{-2} \leq x_{Bi} \leq 10^{-1}$. The same dependence is found for $0.00135 \leq x_{Bi} \leq 0.00734$. Above $x_{Bi} \sim 0.1$ deviations from the linear dependence are indicated. Second, Fig. 5.5 shows that there are changes in the slopes of the Gibbs adsorption isotherms for the three temperatures. For 426 K the slope changes at $x_{Bi} \sim 0.0047$ from $\Gamma_{Bi} = 0.63 \cdot 10^{-5} \text{ mol m}^{-2}$ to $\Gamma_{Bi} = 1.65 \cdot 10^{-5} \text{ mol m}^{-2}$, so to say from low to high Bi adsorption. We are aware of the limited number of data points at this particular temperature, especially for $x_{Bi} > 0.0047$. This is due to the fact that for $x_{Bi} > 0.019$ the surface freezing temperature $T_{sf} \sim 426 \text{ K}$ is met. At $x_{Bi} \sim 0.0054$ and for $T = 456 \text{ K}$, Γ_{Bi} changes from $0.61 \cdot 10^{-5} \text{ mol m}^{-2}$ to $1.46 \cdot 10^{-5} \text{ mol m}^{-2}$, while at $x_{Bi} \sim 0.009$ and for $T = 537 \text{ K}$, it changes from $0.47 \cdot 10^{-5} \text{ mol m}^{-2}$ to $1.32 \cdot 10^{-5} \text{ mol m}^{-2}$. In table 5a we give a summary of the observed breaks in the slopes of the Gibbs adsorption isotherms of Fig. 5.5. The errors in columns 3 and 4 are due to the linear fits to the data for the three indicated temperatures.

T / K	x_{break}	$\Gamma_{low} / 10^{-5} \text{ mol m}^{-2}$	$\Gamma_{high} / 10^{-5} \text{ mol m}^{-2}$	$n_{Bi,Low}^\sigma$	$n_{Bi,high}^\sigma$
426	0.0047	0.63 ± 0.05	1.65 ± 0.22	0.42	~ 1
456	0.0054	0.61 ± 0.010	1.46 ± 0.12	0.4	0.96
537	0.0090	0.47 ± 0.036	1.32 ± 0.1	0.31	0.86

Table 5a. Summary of the observed breaks in the slopes of the Gibbs adsorption isotherms of the Ga-Bi system. For definitions of the columns see the text below.

In table 5a, x_{break} refers to the composition at which the break in the slope occurs. The subscripts low and high in column 3 and 4 refer to low and high Γ_{Bi} , or low and high Bi adsorption. The number of moles of Bi at the surface n_{Bi}^σ is given in the last two columns, again for low and high Bi adsorption using the definition $\Gamma_{Bi} = n_{Bi}^\sigma / A_{Bi}$, where A_{Bi} is the molar area of pure Bi, which is also given above- see equ. (5.1). It is clear from table 5a that for $x_{Bi} > x_{break}$ a surface excess of pure Bi exists at the liquid-vapour interface and that for $x_{Bi} < x_{break}$ a non-zero Bi adsorption exists at the liquid-

vapour interface. Above x_{break} the amount of Bi present at the surface increases by a factor of ~ 3 , again indicating a transition from low to high Bi adsorption. Concerning the temperature variation of Γ_{Bi} , it decreases with increasing temperature, so there is a reduction in Bi adsorption with temperature -see table 5a and Fig. 5.6 below which shows the temperature variation of Γ_{Bi} .

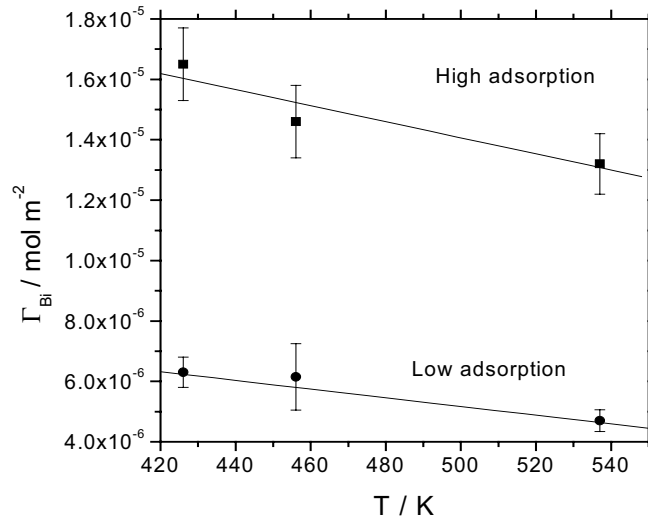


Figure 5.6. Temperature variation of Γ_{Bi} showing low and high Bi adsorption. The error bars are due to the linear fits of the data in Fig. 5.5.

As already mentioned above and shown in Fig. 5.6, Γ_{Bi} clearly decreases with temperature. Going back to Fig. 5.5, the locus of the observed breaks in the σ versus $\Delta\mu_{Bi}^r$ or $\Delta\mu_{Bi}^{id}$ plots is shifted towards higher Bi concentration with increasing temperature. In general, as Bi concentration increases, the transition between the low and high adsorption regimes is shifted towards higher temperatures and is expected to gradually vanish [15] on approaching the critical prewetting temperature (T_{cpw}), where the prewetting line ends- see Fig. 2.4(a). The adsorption is high in the close vicinity of the critical prewetting temperature and low (finite) far from it. From the loci in Fig. 5.5 we have constructed the prewetting line which is shown together with the Ga-rich side of the Ga-Bi phase diagram in Fig. 5.7. The solid line represents the Ga-rich side from the eutectic to the monotectic point. The dashed line represents the prewetting line. The values in parentheses refer to Bi mole fractions (x_{break} in table 5a) and temperature, respectively. As can be seen in Fig. 5.7, the gap between the extension of the prewetting line and the liquidus line gradually narrows with decreasing temperature and is in accord with the expected prewetting phenomena.

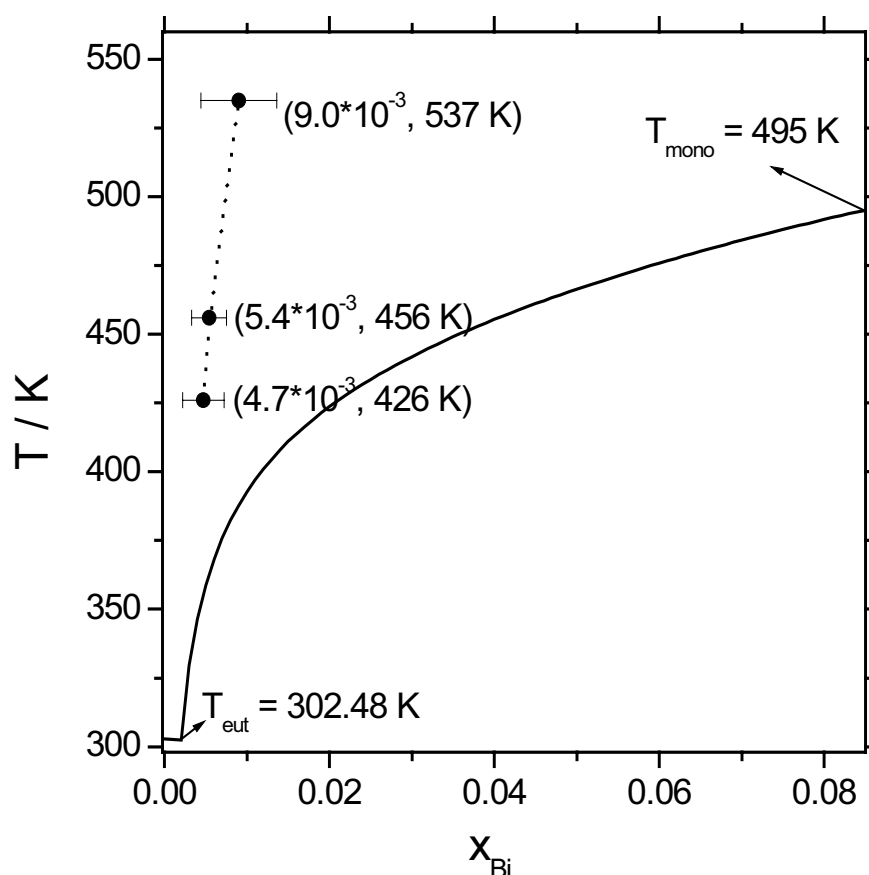


Figure 5.7. Ga-rich side of the Ga-Bi phase diagram (solid line) from the eutectic to the monotectic points with the constructed prewetting line (dashed line). The values in parentheses correspond to x_{Bi} and T , respectively.

Obviously, as is shown in Fig. 5.7, the wetting temperature must lie below 426 K, which is 69 K below the monotectic temperature of 495 K. In order to come to a value closer to the wetting temperature, we roughly extrapolate the prewetting line so that it merges tangentially with the liquidus line below 426 K, then T_w must even lie below ~ 310 K. Of course the precise location of the wetting temperature is difficult to determine. We have to say that the range of uncertainty of this estimate is rather large due to the uncertainty of the parameters used for this estimate, namely, the chemical potential, the surface tension and the linear best fits in Fig. 5.5.

Finally, we should mention that an evaluation of the surface tension data using the ideal solution model instead of the regular solution model gives similar results for Γ_{Bi} .

Gibbs adsorption isotherm of the Ga-Pb system

As was briefly mentioned in chapter 4, the Ga-Pb system is experimentally more difficult to deal with than the Ga-Bi system. Here we find it relevant to explain the reasons behind this difficulty:

1. The Ga-rich side of the Ga-Pb phase diagram, so to say the region between the eutectic and the monotectic point is relatively steep. This complicates the precise determination of the Pb composition and the corresponding temperature and makes this particular region of the phase diagram ill defined. In Fig. 5.8 we expand the Ga-rich side of the Ga-Pb phase diagram (see also Fig. 3.3) to show the differences found in Pb composition and the corresponding temperatures between the available literature data [15, 62]. The dashed line in Fig. 5.8 indicates the metastable limit of solubility of liquid Pb in liquid Ga, the symbols “ Δ ” indicate the solubility limit of solid Pb in liquid Ga. These lines are obtained from thermodynamic phase equilibria calculations by Ansara and Ajersch [85]. The solid circles are the measured data points according to Predel [62], the open circles are the measured eutectic and the monotectic points of Predel. According to Serre *et al* [15, 85]* the monotectic point is at $x_{Pb} = 0.016$, while that of Predel is at $x_{Pb} = 0.024$. The latter is $\sim 30\%$ higher than the former. Note also the difference between Predel’s measured points (solid circles) and that of the phase diagram used by Serre *et al* (dashed curve). For example, at $x_{Pb} = 0.0068$ the liquidus temperature according to Predel is 488 K, while that of Serre *et al* is 519 K. A 31 K difference is found. In order to perform precise measurements and be able to interpret the obtained experimental data to extract information in the presence of wetting and prewetting transitions in the Ga-Pb system one needs a more precise phase diagram.

* Serre *et al* [15] have used all the available thermodynamic data on the Ga-Pb system and expressions given in ref. [85] to construct the phase diagram of the Ga-Pb system.

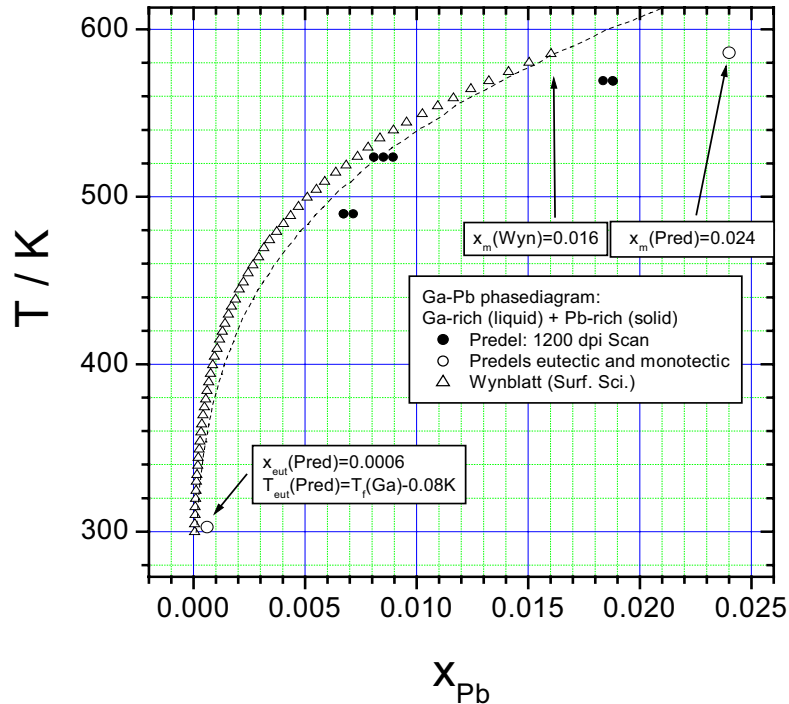


Figure 5.8. Ga-rich side of the Ga-Pb phase diagram showing two sets of literature data as indicated in the figure. The dashed line indicates the metastable limit of solubility of liquid Pb in liquid Ga, the symbols “ Δ ” indicate the solubility limit of the solid Pb in liquid Ga. The open circles are the experimental data, - see text.

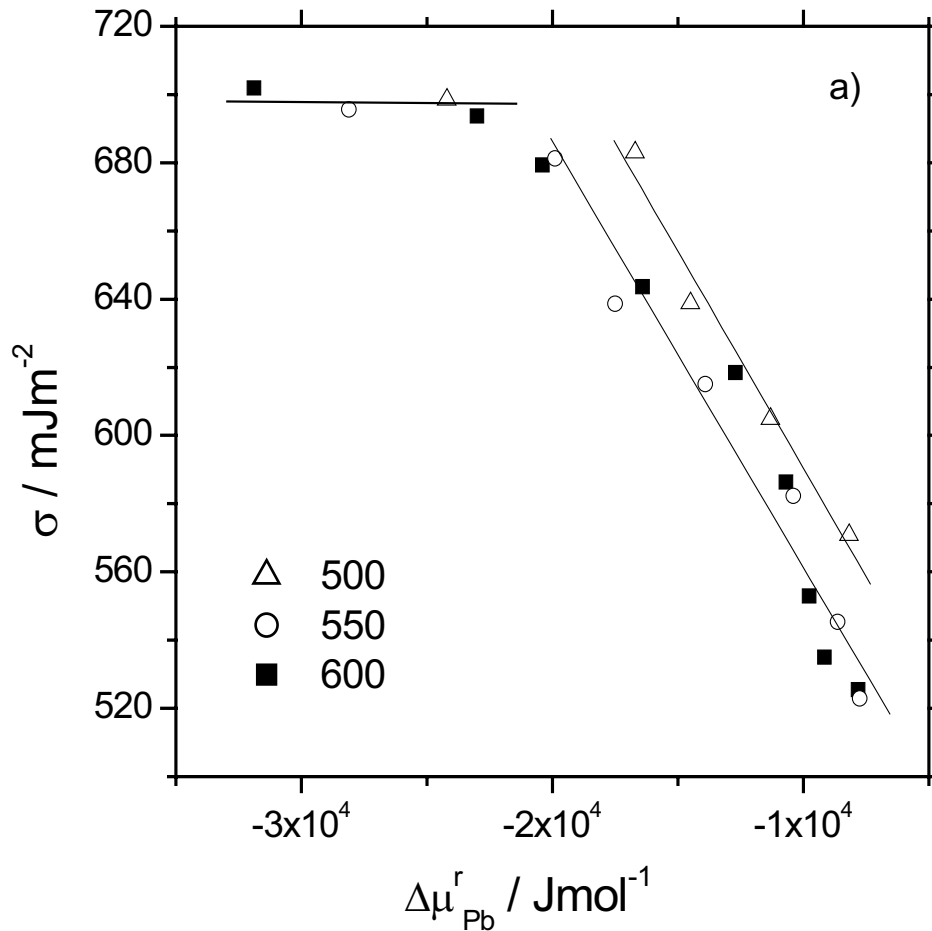
The above presentation of the available literature data concerning the Ga-Pb phase diagram shows the unreliability of the existing phase diagram. However, in this work we have used Predel’s data for the phase diagram.

2. In chapter 4, we have presented the Pb-PbO phase diagram and showed that the PbO is a stable compound up to 599 K with a relatively bulk solid solubility. This in turn complicates the situation further and may cause errors in the measured surface tension especially at low temperatures.
3. Finally, because of the steepness in the Ga-rich side of the phase diagram the corresponding liquidus temperatures at low Pb concentrations are high, e.g. for $x_{Pb} = 0.003$ the liquidus temperature is 473 K. This makes surface light scattering measurements at high Pb concentrations extremely difficult for reasons we have already mention in chapter 3.

In conclusion we have found that the Ga-Bi system is much easier to deal with than the Ga-Pb system, because of the absence of the above mentioned difficulties in case of the former system. This explains the broader range of studied concentrations and in general of data provided in this work for the Ga-Bi system.

Going back to Gibbs adsorption isotherms of the Ga-Pb system. These are shown in Fig. 5.9 for three selected temperatures, $T = 500, 550$ and 600 K. They are plotted vs $\Delta\mu_{Pb}^r$ of the regular solution model (5.9a) and $\Delta\mu_{Pb}^{id}$ of the ideal solution model (5.9b). The solid diagonal lines are the linear best fits to the data for $0.000523 \leq x_{Pb} \leq 0.00421$ at $T = 500$ K and for $0.000898 \leq x_{Pb} \leq 0.0117$ at $T = 600$ K, respectively. The solid horizontal line is drawn to aid the eye in identifying the two limiting regimes since all points at low concentration of Pb for the three selected temperatures fall in the same line- see also Fig. 6(b) of ref. [15].

A linear fit is not shown for the data at 550 K, because it coincides with the linear fit at 600 K. From the data in Fig. 5.9, two adsorption regimes can be distinguished. At low Pb bulk concentrations (horizontal line) the adsorption of Pb at the liquid-vapour interface is almost negligible. While at high Pb concentrations a downward sloping line (solid diagonal line) is indicated, which corresponds to a liquid-vapour interface covered by segregated Pb.



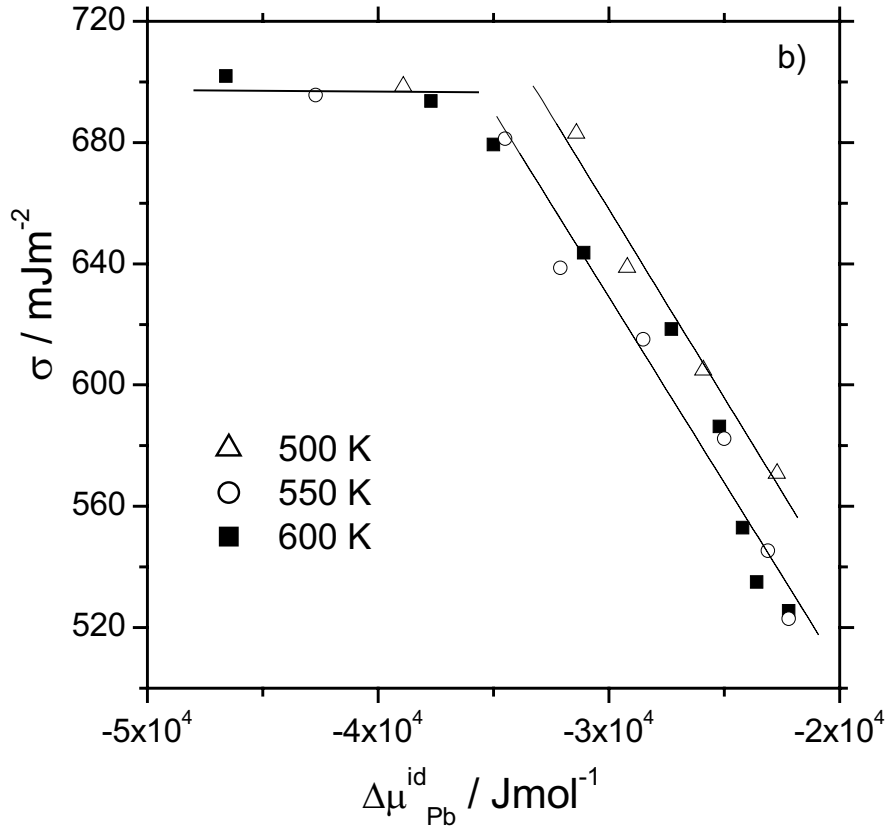


Figure 5.9. Gibbs adsorption isotherms of the Ga-Pb alloys: plotted is the surface energy vs the chemical potential according to the regular solution model, $\Delta\mu_{Pb}^r$ (5.9a) and the ideal solution model, $\Delta\mu_{Pb}^{id}$ (5.9b). For definitions of the solid lines see text.

In terms of numbers and from the linear fit to the data for $0.000523 \leq x_{Pb} \leq 0.00421$ at 500 K, the relative adsorption of Pb is $\Gamma_{Pb} = 1.2 \cdot 10^{-5} \text{ mol m}^{-2}$. Using the molar area of pure Pb of $5.93 \cdot 10^4 \text{ m}^2 \text{ mol}^{-1}$ we derive $n_{Pb}^\sigma = 0.712$. This leads to the conclusion that in this composition range a surface excess of Pb exists at the liquid-vapour interface yet lower than in the Bi-system. From the linear fit to the data at 600 K, $\Gamma_{Pb} = 1.12 \cdot 10^{-5} \text{ mol m}^{-2}$ and $n_{Pb}^\sigma = 0.66$, a reduction of Pb adsorption with increasing temperature is indicated. These values together with the drawn horizontal lines in Fig. 5.9 show clearly the existence of a adsorption transition from low to high adsorption with a break in the slope of the Gibbs adsorption isotherms. This behaviour is in accord with the presence of a first order surface phase transition in the Ga-Pb system. We have to mention that both the regular and the ideal solution models yield almost identical values for Γ_{Pb} . The obtained values for Γ_{Pb} at 500 and 600 K are close to the value $1.45 \cdot 10^{-5} \text{ mol m}^{-2}$, calculated for one monolayer of Pb in a close packed plane [15]. However our value at 600 K is lower than the value found experimentally

by Serre *et al* [15] of $\sim 2.0 \cdot 10^{-5} \text{ mol m}^{-2}$. Based on our data and the corresponding values of Γ_i , where i refers to Bi or Pb, first order wetting transition i.e. a transition from low to high adsorption at a given temperature in the Ga-Bi system prevails at higher bulk composition than in the Ga-Pb system. The transition from a nearly pure Ga surface to a Ga surface covered with Pb occurs over a fairly narrow Pb bulk concentration, whereas in the Ga-Bi system the transition is from a Ga surface covered with a low amount of Bi (non-zero) to a Ga surface highly enriched by Bi and occurs at a wider range of Bi bulk concentration.

5.2.3 *Inconsistency of the monolayer model with the Gibbs adsorption equation*

In this section we show with the help of our experimental data on the Ga-Bi system that the monolayer model is inconsistent with the Gibbs adsorption equation. This inconsistency is described in details in the book of Prigogine and Defay [84]. Here we just give a brief definition of the monolayer model. In this model the system is represented by two homogeneous bulk phases 1 and 2, which are separated by an interphase (or surface region, interface) consisting of a single layer of molecules. It is also assumed that the temperature and the pressure are fixed and that the area of the interface, the number of moles in the interface region and the number of moles in the two bulk phases are given. It has been pointed out by Prigogine and Defay that the advantage of the monolayer model is that it very rapidly yields useful results, though not exact. Perhaps this is why many research groups use the monolayer model to get information on the adsorption of species i on top of species j as will be shown below. Two independent X-ray reflectivity and scattering experiments have been performed to probe the microscopic structure at the surface of Ga-rich liquid Ga-Bi alloys, one at compositions near the eutectic point [10] and another at selected points along the liquidus curve up to the monotectic point [11]. Both investigations come to the conclusion that a nearly complete Bi monolayer segregates at the surface which has the structure of a supercooled liquid. In order to compare these observations with the surface thermodynamic quantities reported here, we discuss the surface energy and entropy in the framework of the monolayer model. In the simplest approximation of μ_{Bi} by the ideal solution model, σ is given by equ. (5.1) above. A plot of x_{Bi}^m versus x_{Bi} according to equ. (5.1) is given in Fig. 5.10 for two temperatures of 450 and 550

K. It can be seen that $x_{Bi}^m \ll 1$ for $x_{Bi} \leq 10^{-2}$ but it reaches values near 0.9 for higher x_{Bi} at 550 K, while at 450 K it reaches values above 1 which is unphysical.

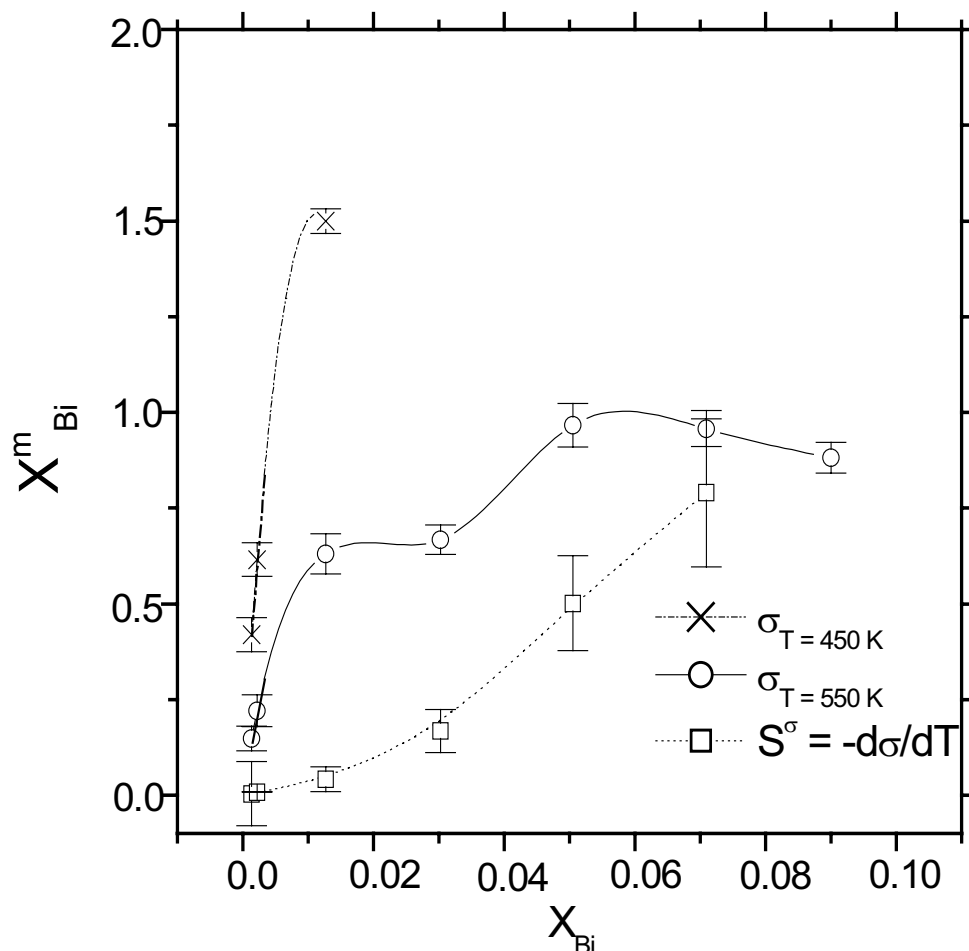


Figure 5.10. Analysis of the surface energy, σ , and surface entropy, $-d\sigma/dT$, by the monolayer model; the corresponding composition of the monolayer, x_{Bi}^m , is given as a function of the bulk Bi mole fraction (see text). The lines are drawn to guide the eye.

A similar calculation for conditions along the coexistence curve ($x_{eut} \leq x_{Bi} \leq x_m$) also yields unphysical values for x_{Bi}^m for $x_{Bi} \geq 10^{-2}$. Also included in Fig. 5.10 is the behaviour of x_{Bi}^m vs x_{Bi} as calculated from the surface entropy data, $-d\sigma/dT$ and $-d\sigma_{Bi}/dT$, respectively, taking the derivative of equ. (5.1) along the coexistence curve. Obviously these data sets are not consistent. They also show that at low x_{Bi} the composition x_{Bi}^m within the monolayer model cannot be approached by pure Bi, but that $x_{Bi}^m \ll 1$. This deficiency does not occur with multilayer models which at a large number n of layers become identical with the Gibbs equation [84].

5.2.4 Analysis of the characteristic change of the surface quantities by a multilayer model

The multilayer model is described in detail in chapter XX of ref. [84]. Here, as we did in the case of the monolayer model, we will give a brief introduction of the multilayer model in addition to recent development of this model by Wynblatt *et al* [14].

In this model the surface of a liquid is pictured as consisting of a series of thin layers placed one on the other. Each layer has its own uniform composition and no assumption is made for the thickness of these layers, they could be of monomolecular thickness. Fig. 5.11 shows a schematic drawing of a liquid surface pictured as a multilayer transition region.

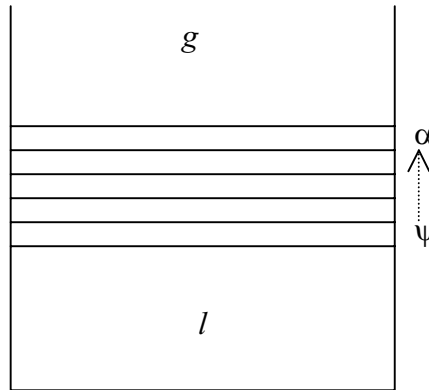


Figure 5.11. Schematic drawing of a liquid surface pictured as a multilayer transition region.

In Fig. 5.11, l refers to the liquid phase, g to the gas phase and the layers ψ, \dots, α etc represent the interfacial region. Layer ψ is in utmost contact with the liquid phase, while layer α is in contact to the gas phase. The liquid phase (l) is homogeneous right up to the interfacial layer ψ and the gas phase (g) is homogenous down to layer α . The inhomogeneity of the system is included in the interfacial region ψ to α , distinct from the monolayer model in which the interfacial region consists of only one layer of composition x^m . The free energy of the whole system can be written as [84]:

$$F = F^g + F^{g\alpha} + F^\alpha + F^{\alpha\beta} + F^\beta + \dots + F^{\psi l} + F^l . \quad (5.4)$$

Wynblatt *et al* have developed a multilayer model to describe the effects of prewetting and wetting transitions on the surface energy of the liquid binary alloys [14]. The inter and intra layer interactions are taken into account by the regular solution approximation. One attractive aspect of this analysis of the surface energy is that it

allows extrapolations for compositions and temperatures which are not easily accessible in the experiment. In [14], the atoms making up the liquid are taken to reside on lattice sites, with a coordination number $z = 12$ far from the surfaces, and a lateral coordination number in any given atom layer parallel to the surface of $z_l = 6$. The number of neighbours of an atom in an adjacent atom layer is $z_v = 3$. The surface energy in the multilayer formalism is given by [14]:

$$\sigma = U - TS, \quad (5.5a)$$

$$\sigma = -\frac{nz_v}{2}\Phi_{BB}x_1 - \frac{nz_v}{2}\Phi_{AA}(1-x_1) - nz_v w(x_1 - 2xx_1 + x^2) - 2nz_v w \sum_{j=1}^k (x_j - x)(x_{j+1} - x) - \sum_{j=1}^k (x_j - x)^2 + nRT \sum_{j=1}^k \left[x_j \ln\left(\frac{x_j}{x}\right) + (1+x_j) \ln\left(\frac{1-x_j}{1-x}\right) \right]. \quad (5.5b)$$

where x_1 is the composition of the first layer, $k = \Psi$; the first term in equ. (5.5b) gives the internal energy U , the last term the entropy S .

The equilibrium composition profile is obtained by minimizing the surface energy with respect to the composition of each layer. They obtained two expressions, one appropriate for layer $j = 1$, and one for any layer with $k \geq j > 1$;

$$RT \ln\left(\frac{x_1}{1-x_1}\right) = RT \ln\left(\frac{x}{1-x}\right) - \left\{ 2w \left[z_1(x-x_1) + z_v(2x-x_2-0.5) + \frac{z_v}{2}(\Phi_{AA} - \Phi_{BB}) \right] \right\}_{j=1},$$

$$RT \ln\left(\frac{x_j}{1-x_j}\right) = RT \ln\left(\frac{x}{1-x}\right) - \left\{ 2w \left[z_1(x-x_j) + z_v(2x-x_{j+1}-x_{j-1}) \right] \right\}, k \geq j > 1 \quad (5.6a, b)$$

where x_j is the composition of each layer, x is the bulk composition, w is the interaction parameter given by $w = 2RT_c$ (T_c is the critical temperature), Φ_{ij} is the nearest neighbour interaction energy given by:

$$\Phi_{ii} = \frac{-2A_i\sigma_i}{z_v}. \quad (5.7)$$

where A_i ($n = 1/A_i$) and σ_i are the area per mole and the surface energy of component i . We have applied this model to our surface energy results. Eqs. (5.5) and (5.6) can be simply solved by numerical iteration to obtain the composition in each layer (x_j) and thus the surface free energy. The procedure is as follows: at a given temperature and bulk composition of the segregated component, the component with a lower surface tension Bi or Pb, and from equ. (5.6a), x_2 can be found by assigning a value to

x_j . The obtained value of x_2 together with the given value of x_1 can be plugged in equ. (5.6b) as x_{j-1} and x_j to find x_{j+1} , hence for $j = 2$, $x_{j-1} = x_1$, $x_j = x_2$ and $x_{j+1} = x_3$. For $j = 3$, the value of x_2 and the obtained value of x_3 for $j = 2$ can be used to find x_4 . The procedure continues (numerical iteration) up to the desired layer. Using the values of $x_1 \dots x_{j+1}$, the surface energy at the same temperature and bulk composition can be found from equ. (5.5b).

Fig. 5.12 shows a comparison between multilayer model calculations and experimental results of the surface free energy of liquid Ga-Bi alloys as a function of bulk Bi mole fraction.

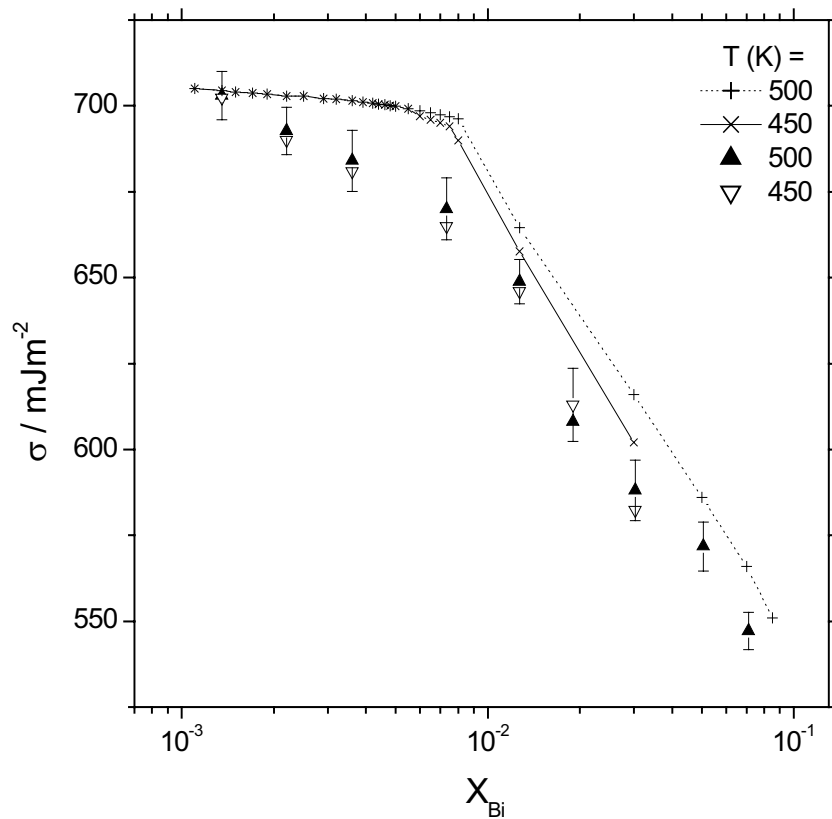


Figure 5.12. Comparison between multilayer model calculations (+), (×) and experimental results (▲, ▼) of the surface free energy of liquid Ga-Bi alloys as a function of bulk Bi mole fraction (in a logarithmic scale) at 500 K, 450 K, respectively and $x_{Bi} < x_m$.

It can be seen from the comparison in Fig. 5.12 that the model calculation qualitatively describes the experimental σ vs $\Delta\mu_{Bi}$ including the turnover of Γ_{Bi} from low to high values. In fact the model calculation predicts that $\Gamma_{Bi} \sim 0$ at low x_{Bi} , while the data in Fig. 5.12 within error bars show that Bi adsorption is finite and non-zero as was demonstrated above, - see Fig. 5.5. At high x_{Bi} a good agreement is clearly seen

between the model calculation and the experimental results. Both data sets show that the turnover to higher Bi adsorption occurs at Bi bulk mole fraction of $\sim 6 \cdot 10^{-3}$ in agreement with the model predictions. It is also interesting to know that σ decreases by only $\sim 30 \text{ mJm}^{-2}$ in the concentration range $0.00135 \leq x_{Bi} \leq 0.00734$, while it decreases by $\sim 130 \text{ mJm}^{-2}$ from the turnover to high Bi adsorption up to the Ga-rich edge of the miscibility gap reaching values close to the surface tension of pure Bi. This indicates the prevalence of a complete wetting of the liquid-vapour interface by Bi in the vicinity of the monotectic point.

We have also applied the multilayer model calculations to the Ga-Pb system and the result at 600 K is shown in Fig. 5.13. Wynblatt *et al* [14] have applied this model to the Ga-Pb system for a wide temperature and composition range, 400 K – 1100 K and $10^{-5} \leq x_{Pb} \leq 10^{-2}$, respectively. In this work we have used the same parameters as those in [14].

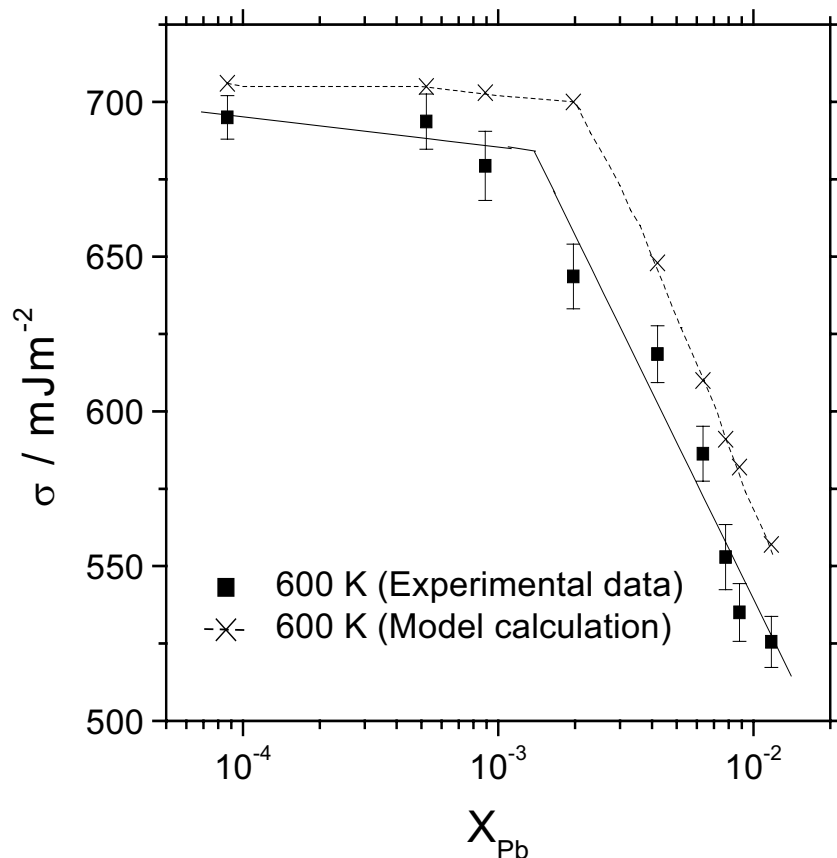


Figure 5.13. Comparison between multilayer model calculations (\times) and experimental results (\blacksquare) of the surface energy of liquid Ga-Pb alloys as a function of Pb mole fraction (in a logarithmic scale) at 600 K and $x_{Pb} < x_m$. The solid lines are linear fits to the data at low $x_{Pb} < 10^{-3}$ and high $x_{Pb} > 10^{-3}$.

As can be seen in Fig. 5.13, the model calculation qualitatively describes the experimental σ vs $\Delta\mu_{Pb}$ curve ($\Delta\mu_{Pb} \propto \ln x_{Pb}$) including the turnover to $\Gamma_{Pb} \sim 0$ at low x_{Pb} . Consistency with the Gibbs adsorption isotherm is approved by comparing the model prediction with Fig. 5.9 above. The experimental data in Fig. 5.13 show that an abrupt change in Pb adsorption at 600 K occurs for Pb bulk mole fraction of $\sim 10^{-3}$, the model calculation predicts a value close to $\sim 10^{-3}$ in agreement with experiment within errors.

From Figs. 5.12 and 5.13 it can be concluded that wetting and prewetting adsorption transitions prevail in the Ga-Bi and Ga-Pb systems, which support the conclusion drawn earlier. The data show that at low x_{Bi} , Bi adsorption is not negligible, which is somewhat similar in the case of Pb. Although in Fig. 5.9 we have drawn a horizontal line at low x_{Pb} through all data points at different temperatures, Fig. 5.13 shows clearly that Pb adsorption at low x_{Pb} is non-zero. A remarkable effect is found by comparing e.g. the surface energy of the eutectic Ga-Bi alloy at $x_{Bi} = 0.0022$ with that of $x_{Pb} = 0.00197$ (which is close to $x_{eut, Ga-Bi}$) at 600 K. The former is found to be ~ 690 mJm⁻² and the latter is ~ 650 mJm⁻², a difference of ~ 40 mJm⁻² is found. This indicates that at comparable compositions and temperature, segregation of Pb on top of the liquid-vapour interface is stronger than Bi segregation even though $\sigma_{Bi} < \sigma_{Pb}$. This effect can be explained by the higher interaction energy of Ga-Pb liquid alloys, $w \propto T_c$, in comparison to that of the Ga-Bi liquid alloy. In addition the nearest neighbour interaction energy Φ_{Pb-Pb} is higher than Φ_{Bi-Bi} since from equ. (5.7) Φ_{ii} is directly proportional to the surface tension. As a consequence the interfacial interaction energy or the interfacial nearest neighbour interaction energy is higher for the Ga-Pb system, which leads to stronger segregation of Pb. This conclusion seems to be in contradiction to the conclusion drawn from the surface energy measurements of Serre *et al* [30] by the sessile drop method on the ternary systems Ga-Pb-Sn and Ga-Pb-Tl. Sn has a surface tension of 550 mJm⁻², which is lower than the surface tension of pure Ga but higher than that of pure Pb. Tl on the other hand has a surface energy of 420 mJm⁻², lower than both pure Ga and Pb [30]. Based on experimental data and multilayer model calculations they have concluded that Pb tends to segregate more strongly than Sn, while Tl segregates more strongly than Sn and slightly more than Pb at the underlying bulk liquid surface. They have related the stronger segregation of Tl relative to that of Sn and to a much lower extent to Pb to two factors: the lower

surface tension of pure Tl, and the higher regular solution parameter of the Ga-Tl system ($w = 1603 \text{ Jmol}^{-1}$) than the Ga-Sn system ($w = 298 \text{ Jmol}^{-1}$), -see table (1) of ref. [30]. The regular solution parameter of the Ga-Pb system ($w = 1655 \text{ Jmol}^{-1}$) is slightly higher than that of the Ga-Tl system. In the case of the Ga-Bi and Ga-Pb systems, the surface energy difference between pure Pb and Pure Bi is only $\sim 50 \text{ mJm}^{-1}$ (higher for Pb). However, the regular solution parameter of the Ga-Pb is almost twice that of the Ga-Bi system. It seems that the second factor plays the dominant role in our case, where the regular solution parameter difference and thus the interaction energy difference overcomes the surface energy difference thus leading to a somewhat higher segregation of Pb in comparison to Bi. Taking what we have just explained into account, the provisional contradiction between our conclusion and that of Serre *et al* is removed.

5.2.5 Estimate of the thickness of the interfacial region

An independent test on the thickness of the surface region, d^σ , and thus on the number of surface layers n can be obtained from the surface entropy. For this aim we make use of the fact that for a plane surface in equilibrium the Gibbs dividing surface can be chosen arbitrarily. If we locate it at the interface between the bulk vapour and the surface region, i.e. at the first layer next to the vapour phase, then the surface entropy is [84]:

$$-\frac{\partial \sigma}{\partial T} \equiv s^\sigma = s^s + d^\sigma s^l, \quad (5.8)$$

Here s^s is the entropy of the surface region per unit area and s^l is the entropy of bulk liquid per unit volume. In the framework of the multilayer model s^s is given by [14]:

$$s^s = -nR \sum_{j=1}^k [x_j \ln(x_j) + (1-x_j) \ln(1-x_j) - x \ln(x) - (1-x) \ln(1-x)]. \quad (5.9)$$

where all terms in equ. (5.9) have been defined above. Taking for the entropy s^l of the alloy the approximation of the ideal solution model, we can estimate d^σ from equ. (5.8). The result of this approximation is shown in Fig. 5.14.

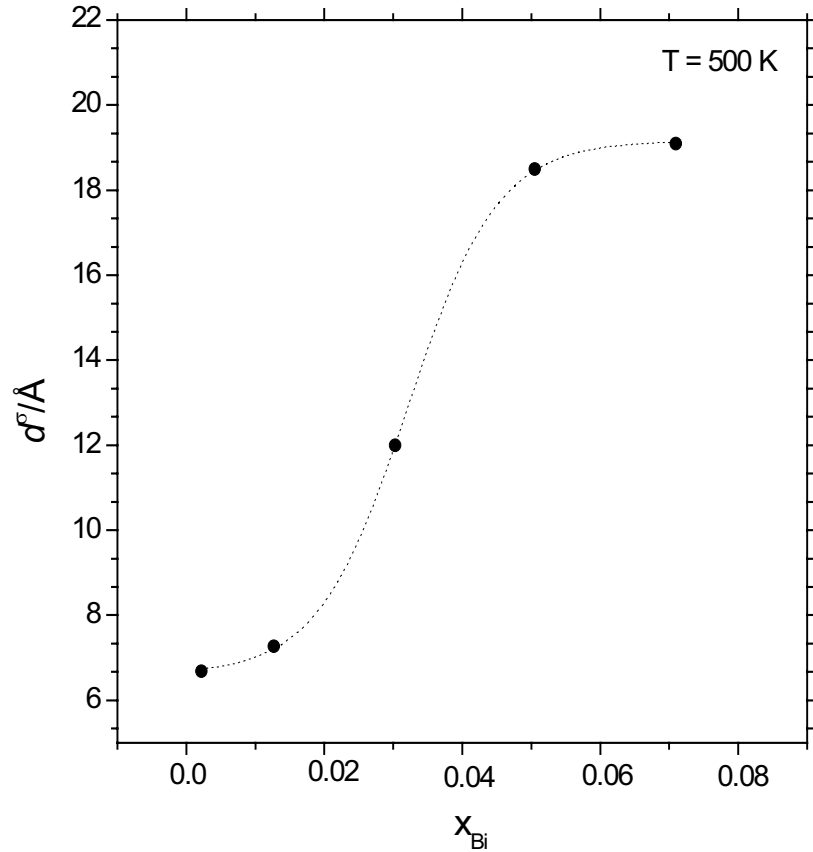


Figure 5.14. Estimate of the thickness, d^σ , of the multilayer surface region from the surface entropy of Ga-Bi alloys at different bulk Bi mole fractions at $T = 500$ K (see text). The dashed line is drawn to guide the eye.

As can be seen in Fig. 5.14, the thickness d^σ at low x_{Bi} is only a few \AA ($\sim 6 - 8 \text{\AA}$). It increases rapidly with increasing Bi concentration reaching a value of $\sim 20 \text{\AA}$ near the monotectic point. We have to say that this is a crude estimate and the uncertainty is rather high. This includes the uncertainty in the temperature derivative of the surface free energy, approximating the entropy of the alloy by the ideal solution model. Nevertheless it gives an order of magnitude estimate of thickness of the surface region.

An estimate of the thickness of the surface region from the surface entropy of the Ga-Pb alloys at different Pb bulk mole fractions and at $T = 500$ K is shown in Fig. 5.15.

From Figs. 5.14 and 5.15, the thickness of the interfacial region, at 500 K and for comparable concentrations of the low tension component, is higher for the Ga-Pb liquid alloys than for its counterparts Ga-Bi, see e.g. for $x \sim 10^{-2}$ the thickness is only $\sim 8 \text{\AA}$ in the case of the Ga-Bi system, while $\sim 12 \text{\AA}$ for the Ga-Pb system. The reason

behind this is the higher temperature coefficient of the surface energy of the Ga-Pb liquid alloys. The observed higher thickness of the interfacial region for the Ga-Pb alloys is another indication of the stronger segregation of Pb than of Bi.

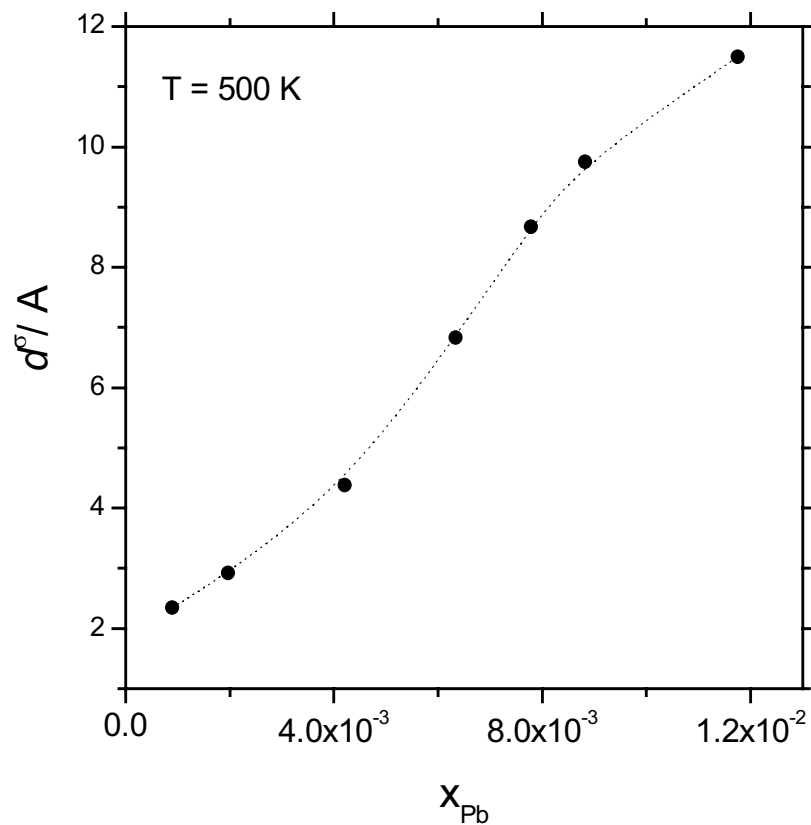


Figure 5.15. Estimate of the thickness of the multilayer surface region from the surface entropy of Ga-Pb alloys at different bulk Pb mole fraction and at $T = 500$ K. The dashed line is drawn to guide the eye.

5.3 Surface freezing and surface viscoelasticity of Ga-Bi and Ga-Pb liquid alloys

The results on surface freezing in Ga-Bi and Ga-Pb liquid alloys (chapter 4) have been obtained for the first time and deserve further consideration. Before we go on discussing these results it is relevant to briefly introduce some aspects of surface freezing (SF) phenomena.

The phenomenon of surface freezing or surface ordering at first sight poses a challenge to the traditional view of molecular or atomic disordering at surfaces and interfaces due to a weaker self-organizing field at the surface than in the bulk liquid [86]. It only has a recent history compared to the common phenomenon of surface melting [86], especially in metallic systems. Hence in chapter 1 we have given examples of systems where surface freezing has been observed, there is no need to repeat them here. SF involves the formation of a solid-like film on bulk liquids or on solid substrates at a few degrees above the bulk melting point and it is of fundamental interest to understand the effects of the interfaces on phase formation in adsorbed films. Formation of such a solid-like film lowers the free energy of the system, see Fig. 5.16 below.

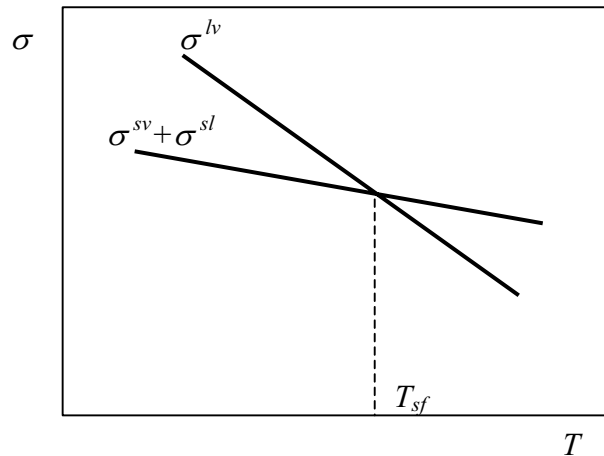


Figure 5.16. Schematic extrapolation of surface freezing with respect to surface energies of the liquid-vapour, solid-vapour and solid-liquid; T_{sf} is the surface freezing temperature.

It follows that,

$$\sigma^{lv} > \sigma^{sv} + \sigma^{sl}. \quad (5.10)$$

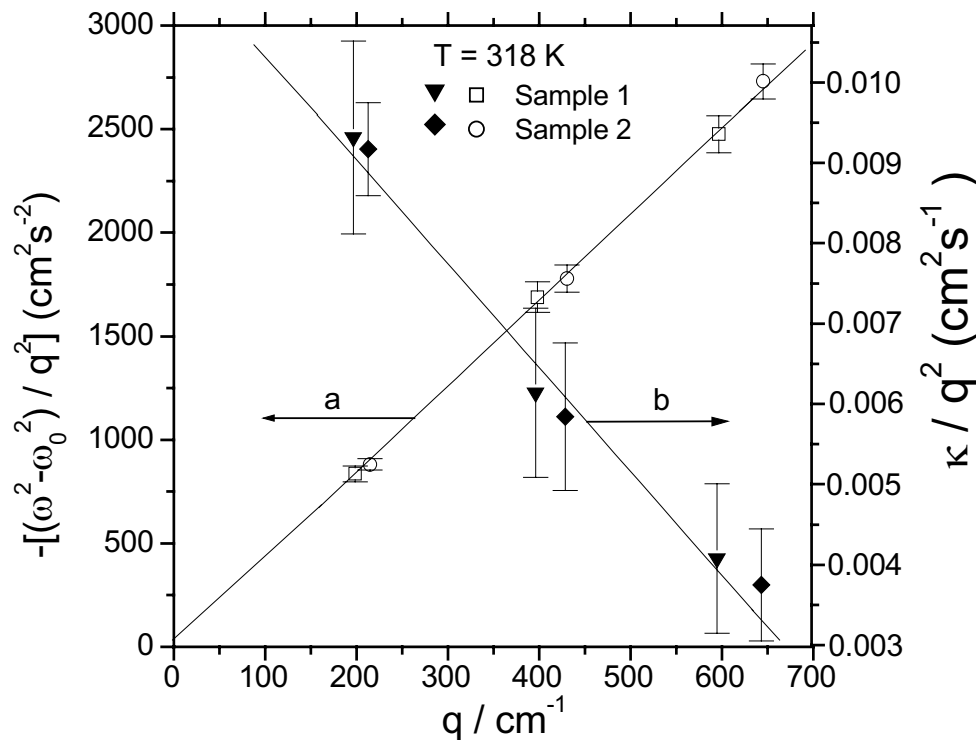
We have to note that replacing the inequality in equ. (5.10) by an equality means that surface freezing may or may not occur, since the condition of minimum free enthalpy is fulfilled with the liquid-vapour interface and there is no need to be replaced by the sum $\sigma^{sv} + \sigma^{sl}$. These considerations (equ. 5.10) are based on the thermodynamic

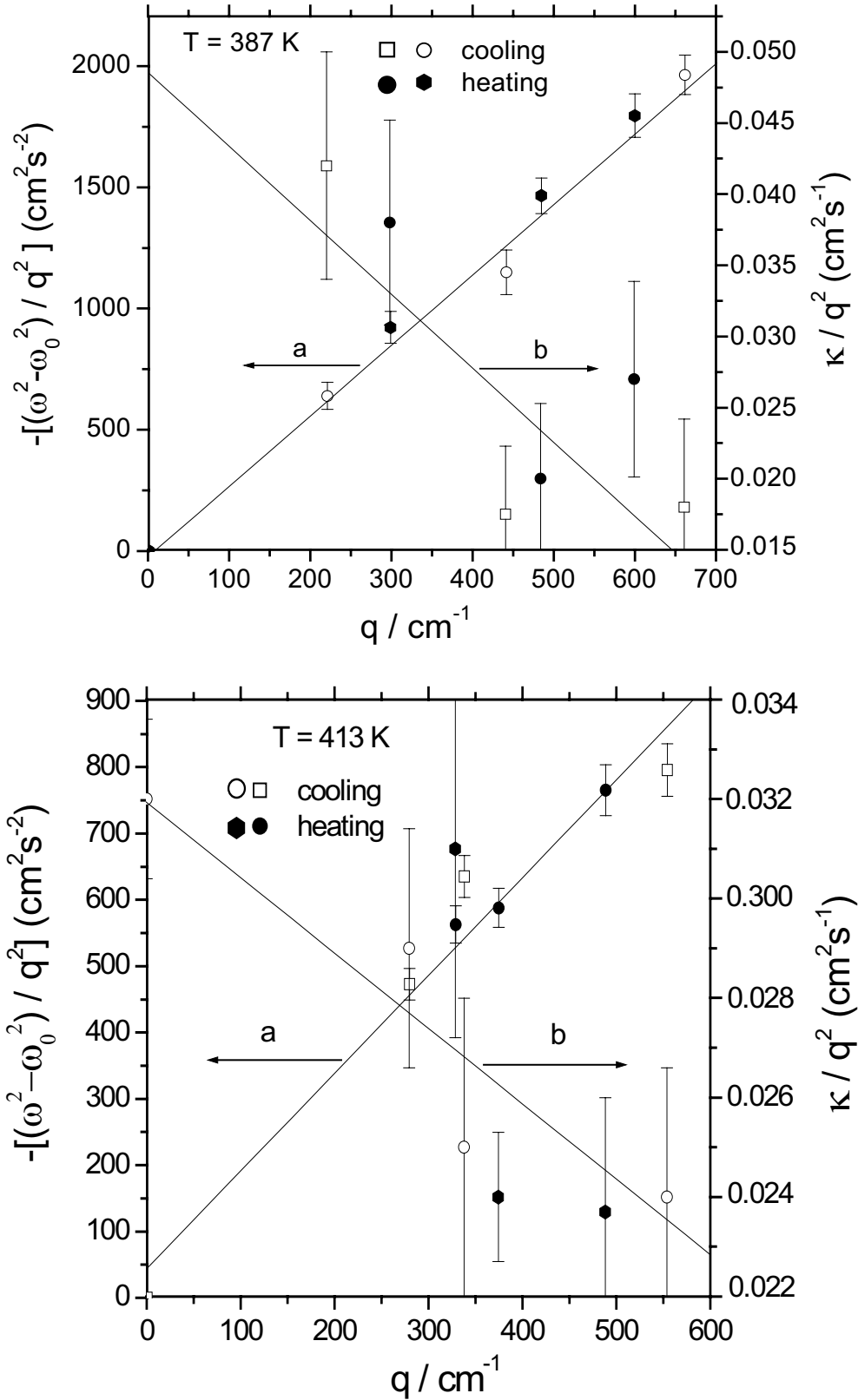
surface energies, i.e. the interface between two macroscopic stable equilibrium phases. However, since the surface freezing film has a microscopic thickness in the range of several nanometers, a correct description is that by the effective interfacial potential which takes into account the correction for finite film thickness [27]. These are some aspects which we think are relevant to the subject we are dealing with.

5.3.1 Surface excess viscoelastic modulus of the Bi and Pb solid-like films

It has been mentioned in chapter 2 that when a monolayer or surface freezing film is present at a fluid interface equ. (2.6) has to be replaced by equ. (2.10) because the monolayer or surface freezing film possess viscoelastic properties. Here we are interested in the capillary wave regime (hydrodynamic regime). In this regime only the surface excess viscoelastic modulus is treated, which consists of two parts: a surface excess elastic part ($\bar{\gamma}_s$) and a surface excess viscous part ($\bar{\eta}_s$). Just to remind ourselves, these two parts describe the resistance against changes in shape of a surface element in the film.

In order to determine these two quantities we extrapolated the values of the density ρ and the surface energy σ of the free surface below the surface freezing temperature T_{sf} and plotted $[\omega^2(q) - \omega_0^2(q)]/q^2$ and $\kappa(q)/q^2$ versus q as shown in Figs. 5.17-5.19 for $x_{Bi} = 0.0022, 0.0073$ and 0.0127 , respectively.





Figures 5.17-19. Surface excess viscoelastic moduli of the liquid-surface freezing films in the liquid $\text{Ga}_{0.9978}\text{Bi}_{0.0022}$, $\text{Ga}_{0.9927}\text{Bi}_{0.0073}$ and $\text{Ga}_{0.9873}\text{Bi}_{0.0127}$ alloys, respectively: (a) determination of $\bar{\gamma}_s$ according to equ (2.10); (b) determination of $\bar{\eta}_l$ according to equ. (2.10). For description of the lines see text.

The lines in Figs. 5.17-19 are linear best fits to the data and the temperatures shown are the surface freezing temperatures. The slopes of these curves yield, see table 5b below:

x_{Bi}	$\bar{\gamma}_s / \text{mNm}^{-1}$	$\bar{\eta}_t \cdot 10^5 / \text{mN}\cdot\text{s}\cdot\text{m}^{-1}$
0.0022	-25.1 ± 0.73	-16.2 ± 2
0.0073	-17.4 ± 0.69	-6.6 ± 3.35
0.0127	-10.6 ± 0.6	-2.1 ± 1.85

Table 5b. Results of the linear best fits to the data in Figs. 5.17-19.

Obviously both $\bar{\gamma}_s$ and $\bar{\eta}_t$ are negative, which is expected according to the drop in ω and κ . A negative $\bar{\gamma}_s$ and $\bar{\eta}_t$ were also observed in the case of surface freezing in alkanes [23]. It has been pointed out by Earnshaw [23] that “in the one density van der Waal’s theory the variation of any quantity through the interface is imagined to follow that of the quantity whose density is used as the defining property (here entropy)”. So following Earnshaw’s argument, a negative surface excess for one quantity implies similar surface excesses for the other. Going back to Figs. 4.18, 4.22 and 4.25 (chapter 4), it is clear that the surface excess entropy density becomes more negative approaching the surface freezing temperature, in accord with the previous argument e.g. for the eutectic composition Ga-Bi liquid alloy (Fig. 4.18) it changes from $\sim -1.9 \cdot 10^{-6} \text{ Jm}^{-2}\text{K}^{-1}$ for the bare liquid surface (in the temperature range 327 K – 343 K to $\sim -1.53 \cdot 10^{-4} \text{ Jm}^{-2}\text{K}^{-1}$ for a surface covered with a Bi solid-like film (in the temperature range 319 K – 326 K).

A remarkable observation is the linear q -dependence in Figs. 5.17-19, which is in line with the dispersion relation according to equ. (2.4). In comparison with the surface freezing films in alkanes [22-23], for all Bi-concentrations studied $\bar{\gamma}_s$ is about an order of magnitude larger, especially for $x_{Bi} = 0.0022$ and 0.0073 with a tendency to approach that of n-alkanes [23] with increasing Bi-concentration. This difference is presumably due to a larger compressional modulus of the metallic surface freezing film in comparison with alkanes. The same trend is found for $\bar{\eta}_t$ which is an order of magnitude higher than in alkanes for the eutectic Ga-Bi liquid alloy and decreases to a value ($-2.1 \cdot 10^{-5} \text{ mN}\cdot\text{s}\cdot\text{m}^{-1}$) very close to that of alkane (e.g. for n-hexadecane $\bar{\eta}_t \approx -2.6$

$\cdot 10^{-5} \text{ mN}\cdot\text{s}\cdot\text{m}^{-1}$) for $x_{Bi} = 0.0073$ (see table 5b above). This excess quantity is not well understood, but qualitatively corresponds to shear stress applied normal to the surface film and not within the film. However, it is plausible that a metallic surface freezing film is more rigid and has a stronger bending elastic modulus [87] than a structured surface layer in alkanes. We have to say that this conclusion applies only to the first two concentrations in table 5b. It is worth mentioning that in the q -range studied here both quantities do not exhibit a significant dependence on ω –see Figs. 5.17-19. A more quantitative interpretation of the surface excess viscoelastic modulus without knowledge of the actual film thickness is difficult.

5.3.2 Concentration and temperature dependence of $\bar{\gamma}_s$ and $\bar{\eta}_t$

In order to discuss the concentration and in addition the temperature dependence of $\bar{\gamma}_s$ and $\bar{\eta}_t$, we first plot the data in table 5b including the errors as shown in Figs. 5.20 and 5.21.

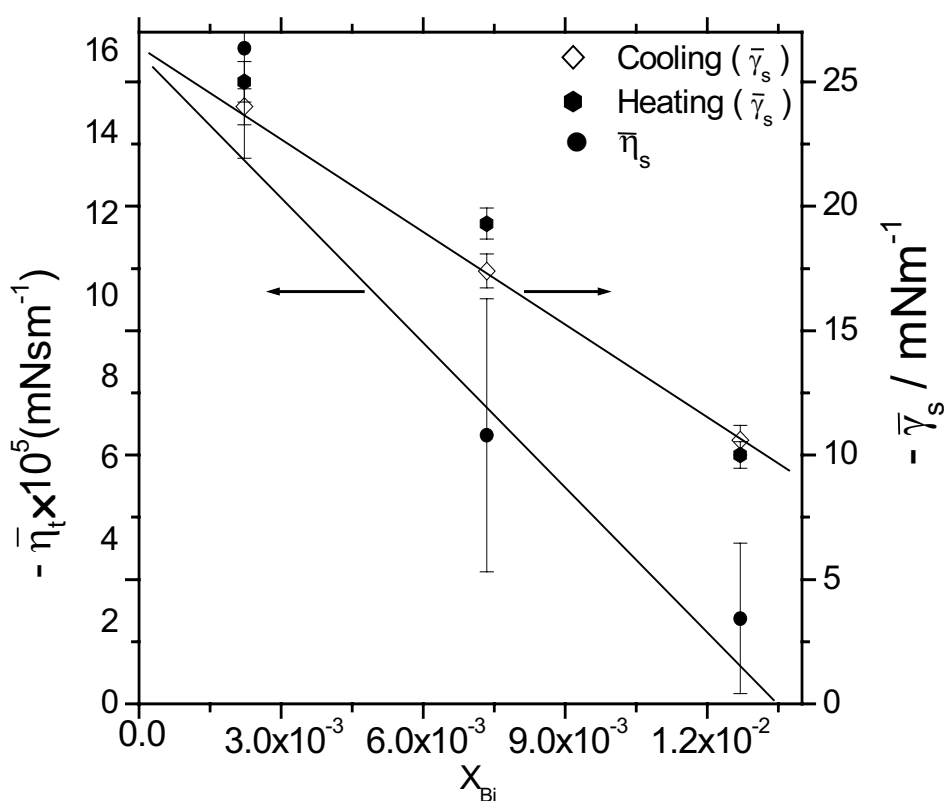


Figure 5.20. Concentration dependence of the surface excess elastic modulus ($\bar{\gamma}_s$) and the surface excess shear viscosity ($\bar{\eta}_t$). The arrows point to the corresponding data of each quantity. Error bars are due the linear fits in Figs. 5.17-19 plus the errors in ω and κ . The lines are linear fits to data.

As can be seen in Fig. 5.20 both quantities within experimental errors decrease almost linearly with increasing Bi-concentration (we will come back to this point latter on). A remarkable finding as briefly mentioned above is that the value of $\bar{\eta}_t$ at the highest Bi-concentration in table 5b is within errors very close to that of alkanes [23], also the value of $\bar{\gamma}_s$ is getting closer to that of alkane.

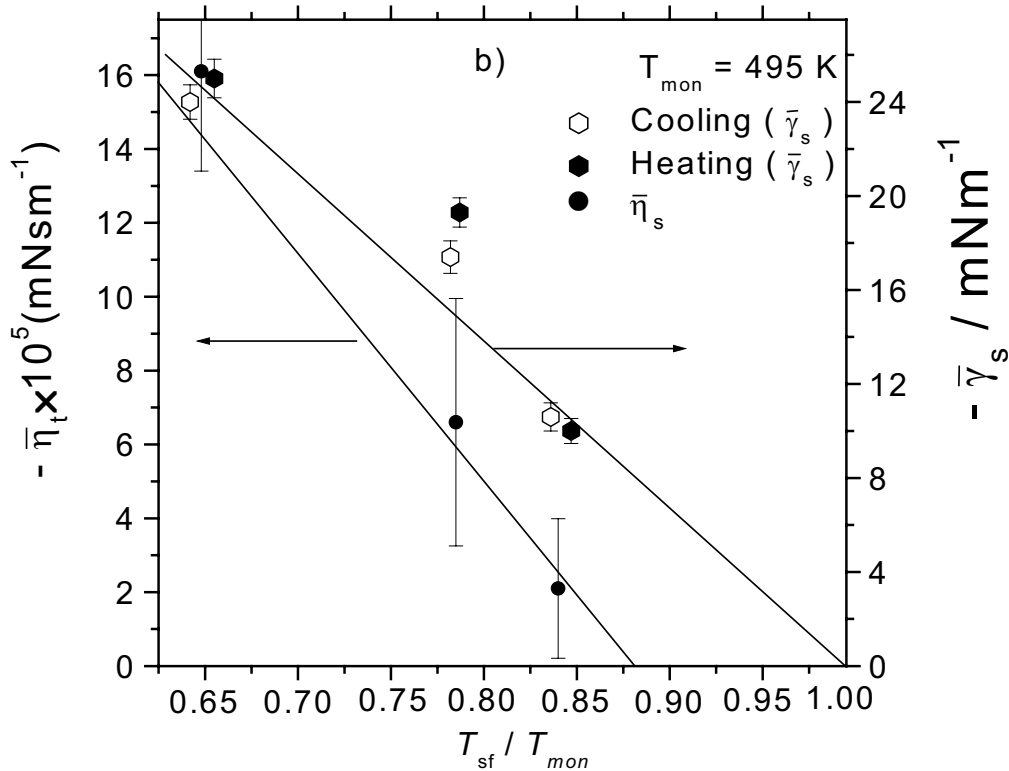


Figure 5.21. $\bar{\gamma}_s$ and $\bar{\eta}_t$ as a function of temperature. T_m refers to the monotectic temperature. The lines are linear fits to data.

Surface viscoelasticity in a eutectic Ga-Pb liquid alloy

In order to determine $\bar{\gamma}_s$ and $\bar{\eta}_t$ for the surface freezing film of Pb on top of the bulk liquid Ga-Pb alloy we proceed like in the case of the Ga-Bi system (see text above). The result is shown in Fig. 5.22 below. The slopes of the curves yield $\bar{\gamma}_s = -13.2 \pm 0.51 \text{ mJm}^{-2}$ and $\bar{\eta}_t = -3.1 \pm 3.5 \cdot 10^{-4} \text{ mN} \cdot \text{s} \cdot \text{m}^{-1}$. The error in $\bar{\eta}_t$ exceeds 100% due to the large scattering in data points of Fig. 5.22 caused by large errors in κ . In this case we can not discuss this quantity, nevertheless the error in $\bar{\gamma}_s$ does not exceed 4%. $\bar{\gamma}_s$ for the Pb surface freezing film at the bulk liquid eutectic Ga-Pb alloy is also one order of

magnitude higher than that found for alkane, but is almost half the value found for its counterpart Bi surface freezing film at the bulk liquid eutectic Ga-Bi alloy. Obviously for the same reasoning given in section 5.2.1: higher Bi bulk concentration and thus surface concentration of the eutectic Ga-Bi alloy than for its counterpart Pb in the liquid eutectic Ga-Pb. This leads to a thinner Pb surface freezing film with smaller compressional modulus.

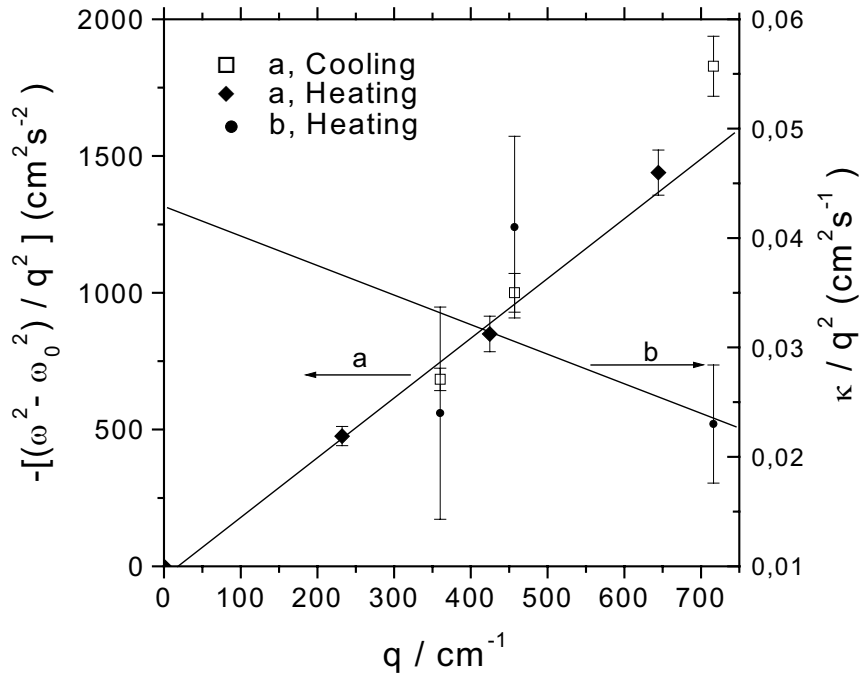


Figure 5.22. Surface excess viscoelastic moduli of the liquid-surface freezing film interface in liquid eutectic Ga-Pb alloy: (a) determination of the surface excess elastic modulus $\bar{\gamma}_s$; (b) determination of the surface excess shear viscosity $\bar{\eta}_t$.

The reduction of $\bar{\gamma}_s(T)$ and $\bar{\eta}_t$ reflects the decrease of the σ - drop on surface freezing. It obviously goes to zero at the monotectic point. With the definition of $\bar{\gamma}_s(T)$ and $\bar{\eta}_t$ the fall of the magnitude of these surface excess quantities with temperature and composition indicates a decrease of the excess viscoelastic modulus governing shear normal to the surface plane. This may happen if with increasing temperature or composition the surface freezing film gets thicker and more rigid. However, there is as yet no theory of the viscoelasticity of surface freezing films, so that we refrain to draw further conclusions. Instead we discuss the relation between the surface freezing film and wetting transitions in these alloys. In the light of the Γ -values (table 5b and

Figs 5.5 and 5.9) and the thickness variation of the wetting films in Figs. 5.14 and 5.15 we consider these wetting films along the liquidus curve as strongly undercooled Bi or Pb liquid films. At a given undercooling ΔT freezing of these films may set in if their thickness d^σ reaches the size of a critical nucleus, R_c , i.e. $d^\sigma \geq R_c$ [88]. Assuming homogeneous nucleation [89];

$$R_c = \frac{2\sigma^{sl}}{n\Delta\mu}. \quad (5.11)$$

where σ^{sl} is the solid-liquid interfacial tension, $\Delta\mu = \Delta T\Delta H_m / T_o$ is the change in chemical potential on transferring n moles from the liquid phase to the solid phase, ΔH_m is the enthalpy of melting, T_o is the melting point of the undercooled liquid, $\Delta T = T_o - T$, where T is any temperature below T_o . For σ^{sl} we use the Turnbull approximation [90], see also [91], $\sigma^{sl} \sim 0.43 n^{2/3} \Delta H_m$, where ΔH_m has the same definition as before. A first rough estimate yields: $R_c \sim 1\text{nm}$ for $\Delta T = 200\text{K}$. This is of the right order of magnitude in comparison with the d^σ . Furthermore, since $R_c \propto \Delta T^{-1}$, we expect thicker surface freezing films approaching the monotectic point, which is in agreement with the merging of the liquidus curve and the T_{sm} -line at T_m – see Fig. 5.23 below. It also predicts fast freezing kinetics, since $\Delta G_c = 0$ for $\theta \rightarrow 0$ at complete wetting. Here θ refers to the contact angle between the frozen phase and the liquid phase. So this nucleation model explains the main features of the observed wetting and surface freezing. Their surface and bulk phase diagrams are summarised in Fig. 5.23 for the example of the Ga-Bi system.

To summarise these findings of the surface freezing measurements, we schematically draw the behaviour of the surface energy of Ga-Bi (or Pb) with temperature at constant x_{Bi} in Fig. 5.24. There are four distinguishable regions in the behaviour of the surface energy with temperature, which are separated by dotted vertical lines in Fig. 5.24. Region I corresponds to a bare liquid surface and the surface excess entropy is large (less negative) as can be seen from the slope of the surface energy vs temperature in this region (see e.g. Fig. 4.18). Capillary wave propagation is high in this region, $\omega_l^2 \propto \sigma_l$. In region II the surface excess entropy is more negative, which indicates surface structural changes or a transition to a quasi-structured surface known as hexatic (h) film of Bi or Pb on top of the bulk liquid.

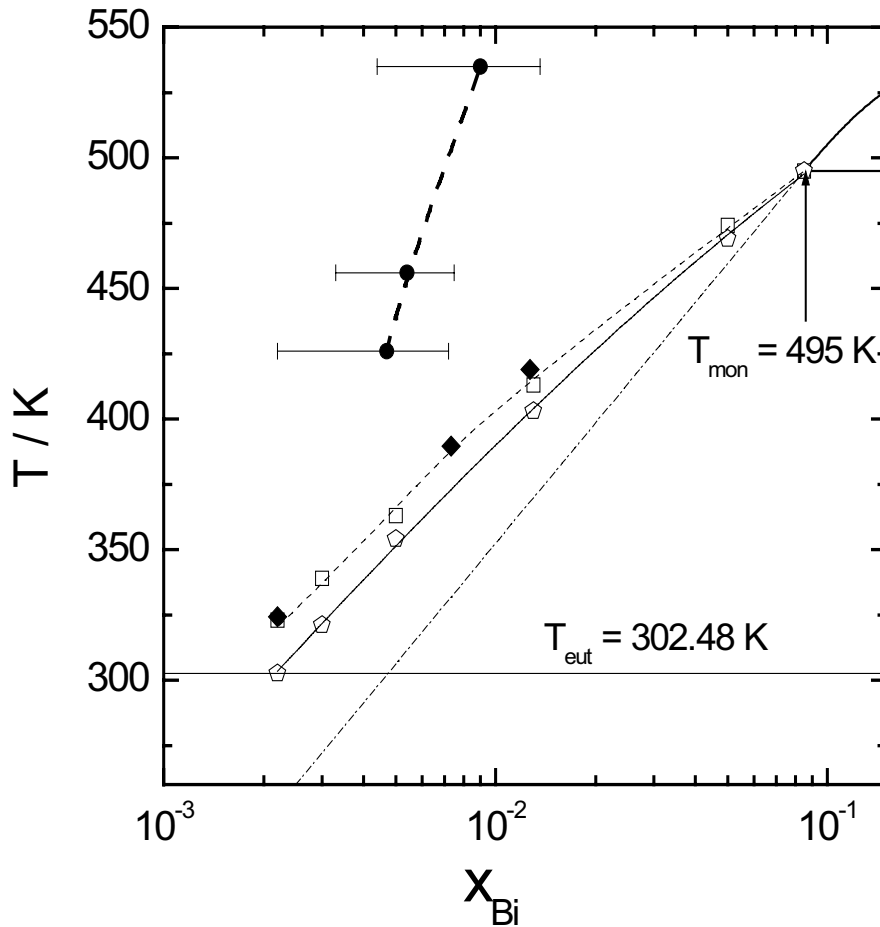


Figure 5.23. Surface phase diagram of Ga-rich liquid Ga-Bi alloys: prewetting line (●--●), surface freezing line (◆--◆) this work, □--□ from [29], liquidus curve (△--△) from [62], section of the liquid-liquid demixing gap (—), linear metastable extension of the latter (— · —), T_{eut} = eutectic temperature, T_{mon} = monotectic temperature.

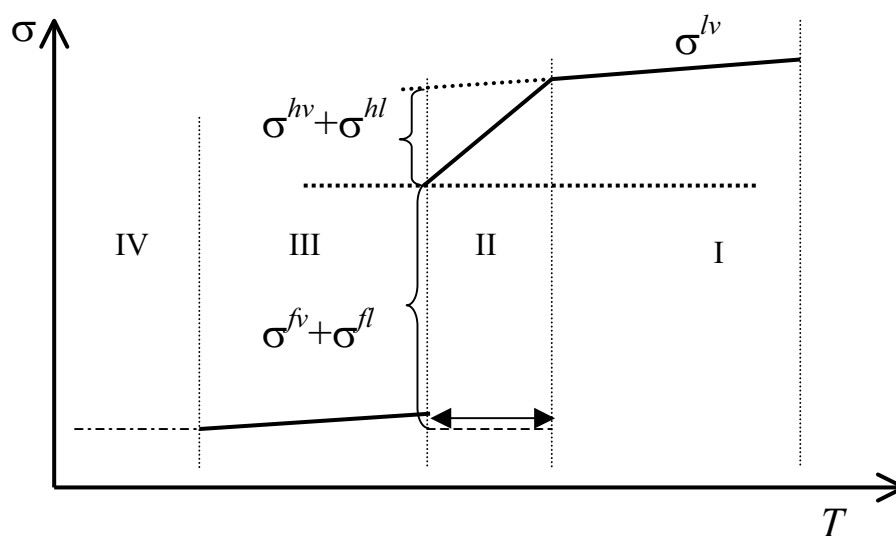


Figure 5.24. Schematic drawing of the different regions observed in the behaviour of the surface free energy of Ga-Bi(Pb) with temperature. For definition of the lines drawn see text.

This region can be considered as a surface-prefreezing transition since capillary waves are slightly more damped and their coupling to longitudinal waves is less, $\omega_{II} < \omega_I$ and $\sigma^{lv} > \sigma^{hv} + \sigma^{hl}$. In region III the coupling and damping of capillary waves is higher than in region II, $\omega_{III} < \omega_{II} < \omega_I$, $\sigma^{fv} + \sigma^{fl} < \sigma^{hv} + \sigma^{hl} < \sigma^{lv}$, which indicates that surface freezing has propagated to more surface layers in region III than in region II and therefore the thickness of the surface freezing film (f) is larger than the hexatic film (h) in region II. Hence, here we make a distinction between a hexatic (h) film in region II and a surface freezing film (f) in region III only to indicate different thickness of the film in these regions.

In region IV the capillary waves are completely damped (frozen), $\omega_{IV} = 0 < \omega_{III} < \omega_{II} < \omega_I$. Here the surface freezing has propagated to more surface layers than in region III, thus forming a relatively macroscopic surface freezing film of a thickness in the order of $\sim \mu m$.

The height and width of the hysteresis gap, indicated by the double headed arrow in Fig. 5.24, are reduced with increasing Bi concentration (see e.g. Fig. 5.20).

Finally the wetting, prewetting and the related surface freezing transitions in these alloys is completely consistent with the tetra point scenario of Dietrich and Schick [92].

Appendix

Data of all CWS measurements on Pure Ga, pure Bi, Ga-Bi and Ga-Pb liquid alloys*

Pure Ga

<i>T</i> (K)	<i>q</i> / <i>cm</i> ⁻¹	<i>Frequ.</i> / <i>s</i> ⁻¹
302	431.3	15523.3 ± 11
304	431.3	15549.9 ± 17
307	431.3	15587.9 ± 9
309	431.3	15608.3 ± 22
311	431.3	15634.8 ± 14
313	431.3	15670.9 ± 6
315	431.3	15689.6 ± 31
318	431.3	15734.7 ± 12
323	431.3	15744.5 ± 15
327	431.3	15751.3 ± 11
333	431.3	15756.2 ± 23
340	431.3	15763.3 ± 4
348	431.3	15763.9 ± 33
355	431.3	15769.4 ± 50
367	443	16384.2 ± 13
381	443	16343.2 ± 24
403	443	16309.4 ± 3
426	443	16298.1 ± 19
442	443	16264.3 ± 8
462	443	16253.0 ± 2
473	443	16241.7 ± 74
496	443	16230.4 ± 29

*Ga*_{0.9978}*Bi*_{0.0022}

<i>T</i> (K)	<i>q</i> / <i>cm</i> ⁻¹	<i>Frequ.</i> / <i>s</i> ⁻¹
325	291.4	8440.8 ± 14
328	291.4	8448.6 ± 9
333	291.4	8462.3 ± 13
348	291.4	8470.8 ± 9
363	291.4	8478.5 ± 5
378	291.4	8482.8 ± 9
393	291.4	8490.3 ± 13
408	291.4	8494 ± 19
423	291.4	8505 ± 11
438	291.4	8511 ± 12
453	319.12	9755.3 ± 6
468	319.12	9752.5 ± 10

* Note, the values given for the measured peak frequencies are without multiplication by 2π . All the original spectra used in this work have been saved on a CD-rom and can be found in Prof. Freyland's room.

483	319.12	9755.6 ± 17
498	319.12	9755.7 ± 11
513	347	10949 ± 22
324	347	11010. ± 15
424	361	11730 ± 17
484	361	11725 ± 8

 $Ga_{0.99865}Bi_{0.00135}$

T (K)	q / cm^{-1}	Freque. / s^{-1}
303	443.9	15774 ± 13
313	443.9	15866 ± 22
328	443.9	15948 ± 7
343	443.9	15960 ± 11
358	443.9	15974 ± 6
373	443.9	15978 ± 9
388	443.9	15981 ± 16
403	443.9	15987 ± 4
418	443.9	15988 ± 10
433	443.9	15988 ± 12
449	443.9	15988 ± 3
465	443.9	16256 ± 30
477	457	16847 ± 19
483	457	16839 ± 12
499	457	16858 ± 22
514	457	16860 ± 6
528	457	16865 ± 14
302	321	9815 ± 4
344	321	9891 ± 1
388	321	9893 ± 6
448	333.5	10483 ± 9
501	333.5	10525 ± 4

 $Ga_{0.9964}Bi_{0.0036}$

T (K)	q / cm^{-1}	Freque. / s^{-1}
343	477.78	17206.9 ± 42
353	477.78	17301 ± 21
373	477.78	17403 ± 18
393	477.78	17441 ± 51
413	477.78	17502 ± 34
433	477.78	17544 ± 7
453	477.78	17555 ± 30
473	534.9	20790 ± 26
493	534.9	20797 ± 24
519	534.9	20799 ± 18
533	534.9	20824 ± 61
345	494.6	18078 ± 9
392	494.6	18342 ± 32
453	494.6	18425 ± 11
513	511.42	19473 ± 16

*Ga*_{0.9874}*Bi*_{0.0126}

<i>T</i> (K)	<i>q</i> / <i>cm</i> ⁻¹	<i>Freque.</i> / <i>s</i> ⁻¹
408	287.6	7909 ± 10
423	287.6	7892 ± 10
448	287.6	7891 ± 19
463	287.6	7927 ± 12
488	287.6	7897 ± 6
413	287.6	7921 ± 20
457	287.6	7933 ± 16
416	309	8836 ± 14
459	309	8822 ± 8
493	309	8849 ± 3
514	309	8849 ± 11

*Ga*_{0.949}*Bi*_{0.051}

<i>T</i> (K)	<i>q</i> / <i>cm</i> ⁻¹	<i>Freque.</i> / <i>s</i> ⁻¹
476	359.7	10219 ± 8
478	359.7	10255 ± 15
484	359.7	10313 ± 12
495	359.7	10342 ± 11
503	359.7	10359 ± 12
513	359.7	10371 ± 11
523	359.7	10378 ± 43
458	410.6	12220 ± 9
463	410.6	12442 ± 5
473	410.6	12593 ± 7
494	410.6	12631 ± 9
513	372	10528 ± 11
459	372	10685 ± 7
469	372	10820 ± 12
494	372	10848 ± 11
514	372	10877 ± 9

*Ga*_{0.9926}*Bi*_{0.0074}

<i>T</i> (K)	<i>q</i> / <i>cm</i> ⁻¹	<i>Freque.</i> / <i>s</i> ⁻¹
383	571.83	22484 ± 5
393	571.83	22558 ± 12
413	571.83	22655 ± 13
433	571.83	22677 ± 10
453	571.83	22698 ± 13
473	571.83	22715 ± 12
493	586.4	23581 ± 25
513	586.4	23598 ± 24
533	586.4	23625 ± 13
381	571.83	22477 ± 11
432	571.83	22666 ± 10
492	583.5	23363 ± 13
532	583.5	23399 ± 11

*Ga*_{0.97}*Bi*_{0.03}

<i>T</i> (K)	<i>q</i> / <i>cm</i> ⁻¹	<i>Freque.</i> / <i>s</i> ⁻¹
448	328	9175 ± 5
453	328	9214 ± 5
468	328	9247 ± 16
484	328	9256 ± 10
499	328	9268 ± 12
512	328	9277 ± 13
528	328	9283 ± 8
449	356	10398 ± 41
461	356	10447 ± 12
497	356	10471 ± 7
428	356	10504 ± 4

*Ga*_{0.9291}*Bi*_{0.00709}

<i>T</i> (K)	<i>q</i> / <i>cm</i> ⁻¹	<i>Freque.</i> / <i>s</i> ⁻¹
488	465	14640 ± 10
489	465	14751 ± 9
499	465	14849 ± 3
508	465	14878 ± 9
519	465	14920 ± 34
529	465	14925 ± 5
485	459	14332 ± 13
502	459	14578 ± 7
517	459	14602 ± 32
526	459	14632 ± 8

*Ga*_{0.91}*Bi*_{0.09}

<i>T</i> (K)	<i>q</i> / <i>cm</i> ⁻¹	<i>Freque.</i> / <i>s</i> ⁻¹
496	411.1	11389 ± 16
503	411.1	12013 ± 12
511	411.1	12058 ± 14
521	411.1	12095 ± 13
531	411.1	12109 ± 18
496	423.6	11863 ± 10
510	423.6	12582 ± 4
530	423.6	12682 ± 9

*Ga*_{0.8901}*Bi*_{0.1099}

<i>T</i> (K)	<i>q</i> / <i>cm</i> ⁻¹	<i>Freque.</i> / <i>s</i> ⁻¹
496	374	9562 ± 24
501	374	9693 ± 15
511	374	10160 ± 30
520	374	10198 ± 29
530	374	10225 ± 32
496	391	10255 ± 14
509	391	10825 ± 31
529	391	10904 ± 15

*Ga*_{0.702}*Bi*_{0.298}

<i>T</i> (K)	<i>q</i> / <i>cm</i> ⁻¹	<i>Frequ.</i> / <i>s</i> ⁻¹
498	452.56	11911 ± 33
507	452.56	12021 ± 4
522	452.56	12048 ± 9
537	452.56	12278 ± 12
554	452.56	12345 ± 31
567	452.56	12438 ± 15
499	477.4	12860 ± 34
523	477.4	13069 ± 7
553	477.4	13404 ± 29
565	477.4	13462 ± 71

*Ga*_{0.61}*Bi*_{0.39}

<i>T</i> (K)	<i>q</i> / <i>cm</i> ⁻¹	<i>Frequ.</i> / <i>s</i> ⁻¹
497	539.3	14045 ± 10
501	539.3	14096 ± 10
508	539.3	14158 ± 6
520	539.3	14213 ± 19
531	539.3	14310 ± 17
498	553.6	14662 ± 64
507	553.6	14856 ± 69
532	553.6	14842 ± 55

*Ga*_{0.19}*Bi*_{0.81}

<i>T</i> (K)	<i>q</i> / <i>cm</i> ⁻¹	<i>Frequ.</i> / <i>s</i> ⁻¹
503	583.8	14644 ± 373
513	583.8	14646 ± 33
528	583.8	14673 ± 40
544	583.8	14728 ± 30
557	583.8	14758 ± 32
573	583.8	14764 ± 19
502	559.4	13697 ± 60
526	559.4	13677 ± 24
571	559.4	13893 ± 8

Pure Bi

<i>T</i> (K)	<i>q</i> / <i>cm</i> ⁻¹	<i>Frequ.</i> / <i>s</i> ⁻¹
546	497.5	10973 ± 7
560	497.5	10950 ± 16
577	508.36	11290 ± 10
591	508.36	11269 ± 12
605	515.2	11465 ± 14
618	515.2	11444 ± 9
545	477.8	10298 ± 13
576	477.8	10290 ± 18
604	486.56	10490 ± 36

$Ga_{0.99947}Pb_{0.000523}$

T (K)	q / cm^{-1}	Freque. / s^{-1}
336	413.47	14112 ± 222
339	413.47	14135 ± 19
342	413.47	14155 ± 12
346	413.47	14174 ± 16
349	413.47	14209 ± 10
352	413.47	14234 ± 15
356	413.47	14254 ± 17
360	413.47	14275 ± 19
376	413.47	14340 ± 11
391	413.47	14389 ± 27
406	413.47	14419 ± 46
423	413.47	14454 ± 12
439	422.2	15048 ± 20
454	422.2	15056 ± 22
472	422.2	15038 ± 27
491	422.2	15029 ± 27
507	422.2	15016 ± 9
523	422.2	15008 ± 31
539	431.8	15517 ± 68
555	431.8	15499 ± 20
569	440.74	15976 ± 15
583	440.74	15966 ± 19
337	562.5	22338 ± 49
350	562.5	22573 ± 7
359	562.5	22622 ± 13
373	562.5	22808 ± 12
404	562.5	22844 ± 20
455	574.8	23946 ± 19
505	574.8	23888 ± 17
567	586	24452 ± 63

 $Ga_{0.999102}Pb_{0.000898}$

T (K)	q / cm^{-1}	Freque. / s^{-1}
344	392	12868 ± 13
347	392	12870 ± 15
350	392	12876 ± 20
354	392	12914 ± 10
358	392	12955 ± 19
362	392	12972 ± 12
366	392	13006 ± 16
369	392	13027 ± 13
373	392	13047 ± 12
388	392	13105 ± 19
404	392	13155 ± 10
422	392	13168 ± 15
440	417.4	14488 ± 17
452	417.4	14481 ± 16
467	417.4	14482 ± 16
482	417.4	14478 ± 13
497	417.4	14473 ± 19
512	417.4	14467 ± 16

527	417.4	14464 ± 12
452	436	15434 ± 18
557	436	15432 ± 16
582	436	15430 ± 5
345	422.6	14420 ± 33
356	422.6	14476 ± 18
374	422.6	14552 ± 17
387	422.6	14651 ± 13
438	442.75	15793 ± 21
498	442.75	15792 ± 13
554	442.75	15804 ± 10

 $Ga_{0.99803}Pb_{0.00197}$

T (K)	q / cm^{-1}	Freque. / s^{-1}
441	457.6	15789 ± 16
445	457.6	15849 ± 15
449	457.6	15883 ± 20
455	457.6	15924 ± 15
460	457.6	15977 ± 19
466	457.6	15998 ± 20
480	457.6	16021 ± 25
494	457.6	16036 ± 15
510	457.6	16032 ± 17
524	457.6	16038 ± 20
538	469	16727 ± 16
554	469	16731 ± 17
568	469	16739 ± 14
583	469	16746 ± 22
441	428.36	14269 ± 13
454	428.36	14448 ± 8
479	428.36	14529 ± 14
523	428.36	14504 ± 22
567	443.96	15387 ± 18

 $Ga_{0.99579}Pb_{0.00421}$

T (K)	q / cm^{-1}	Freque. / s^{-1}
504	437.72	14616 ± 17
509	437.72	14657 ± 20
523	437.72	14674 ± 14
538	437.72	14689 ± 23
554	453.4	15497 ± 12
568	453.4	15496 ± 9
583	453.4	15498 ± 20
503	428.65	14130 ± 15
539	428.65	14256 ± 17
582	428.65	14211 ± 16

*Ga*_{0.98101}*Bi*_{0.01899}

<i>T</i> (K)	<i>q</i> / <i>cm</i> ⁻¹	<i>Frequ.</i> / <i>s</i> ⁻¹
473	331.7	9490.5 ± 9
488	331.7	9487.7 ± 5
503	331.7	9491.7 ± 7
518	331.7	9502.2 ± 14
533	331.7	9508.7 ± 5
473	331.7	9519.7 ± 3
488	331.7	9529.5 ± 18
503	331.7	9530.7 ± 1
518	331.7	9536.1 ± 23
473	428.93	13975.7 ± 25
488	428.93	13932.8 ± 32
503	428.93	13935.1 ± 44
518	428.93	13933.4 ± 7
533	428.93	14004 ± 19
473	428.93	14007 ± 3
488	428.93	14028.2 ± 11
503	428.93	14023.8 ± 32
518	428.93	14038.2 ± 48
473	542.4	19869 ± 52
488	542.4	19849.5 ± 74
503	542.4	19878.7 ± 36
518	542.4	19828.8 ± 12
533	542.4	19814.6 ± 41
473	542.4	19848.2 ± 29
488	542.4	19915 ± 33
503	542.4	19994 ± 20
518	542.4	19981.6 ± 24
473	347.6	10252.5 ± 26
488	347.6	10258.1 ± 39
503	347.6	10262.7 ± 6
518	347.6	10267.3 ± 17
533	347.6	10272 ± 23

*Ga*_{0.99366}*Pb*_{0.00634}

<i>T</i> (K)	<i>q</i> / <i>cm</i> ⁻¹	<i>Frequ.</i> / <i>s</i> ⁻¹
508	518.7	18290.7 ± 15
513	518.7	18380.8 ± 12
528	518.7	18400.1 ± 23
542	518.7	18412.8 ± 9
557	531.4	19182.3 ± 10
572	531.4	19200.8 ± 13
581	531.4	19216.5 ± 16
507	498.58	17188.3 ± 11
541	498.58	17319.8 ± 12
580	512.83	18193.6 ± 38

$Ga_{0.9922}Pb_{0.00778}$

<i>T</i> (K)	<i>q</i> / cm^{-1}	<i>Freque.</i> / s^{-1}
532	563.7	20116.5 ± 22
544	563.7	20184.9 ± 58
556	563.7	20226.4 ± 206
567	575.39	20882.5 ± 32
579	575.39	20903.2 ± 8
585	575.39	20899.7 ± 12
532	554.28	19568.4 ± 21
555	554.28	19692.1 ± 8
579	561.46	20089.3 ± 65
584	561.46	20111.2 ± 15

 $Ga_{0.99118}Pb_{0.00882}$

<i>T</i> (K)	<i>q</i> / cm^{-1}	<i>Freque.</i> / s^{-1}
540	487.2	15807.8 ± 11
545	487.2	15856.9 ± 64
550	487.2	15916.7 ± 66
558	487.2	15939.2 ± 7
568	502.6	16741.7 ± 58
578	502.6	16771.1 ± 19
583	502.6	16783 ± 35
540	495.39	16267.5 ± 144
551	495.39	16303.3 ± 25
568	495.39	16413.6 ± 15
582	495.39	16378.7 ± 19

 $Ga_{0.98825}Pb_{0.01175}$

<i>T</i> (K)	<i>q</i> / cm^{-1}	<i>Freque.</i> / s^{-1}
562	398.7	11493.4 ± 16
567	398.7	11548.7 ± 13
570	398.7	11618.6 ± 10
573	398.7	11672.6 ± 15
578	398.7	11693.8 ± 13
583	398.7	11711.3 ± 10
588	417.92	12581.1 ± 11
592	417.92	12603.7 ± 10
561	400.59	11554.3 ± 12
572	400.59	11728.2 ± 11
588	400.59	11788.1 ± 11

Ga_{0.9978}Bi_{0.0022} (cooling, sample 1)

<i>T/K</i>	<i>Freque.1, s⁻¹</i>	<i>Freque.2, s⁻¹</i>	<i>Freque.3, s⁻¹</i>
312	4627.2 ± 4	13141.0 ± 12	24068.2 ± 11
314	4626.5 ± 7	13123.0 ± 6	24086.9 ± 32
315.5	4630 ± 9	13137.4 ± 11	24107.1 ± 27
317.7	4628.5 ± 1	13126.7 ± 13	24094.3 ± 8
319.7	4708.8 ± 6	13348.8 ± 31	24451.2 ± 33
321.8	4711.9 ± 2	13356.7 ± 22	24501.3 ± 42
324	4713.3 ± 15	13365.5 ± 15	24497.0 ± 12
326	4717 ± 9	13373.6 ± 13	24535.8 ± 41
328	4717.8 ± 13	13382.9 ± 7	24516.4 ± 25
343	4719.9 ± 17	13385.2 ± 5	24522.7 ± 22
<i>q/cm⁻¹</i>	198.16	398.15	596.416

Ga_{0.9978}Bi_{0.0022} (cooling, sample 2)

<i>T/K</i>	<i>Freque.1, s⁻¹</i>	<i>Freque. 2, s⁻¹</i>	<i>Freque.3, s⁻¹</i>
343	5301.3 ± 7	15035.3 ± 19	27617.2 ± 47
320	5298.3 ± 7	14979.1 ± 18	27520.4 ± 46
318	5215.5 ± 3	14740.6 ± 15	27051.5 ± 29
312	5204.6 ± 9	14759.5 ± 33	27069.5 ± 33
<i>q/cm⁻¹</i>	214,9	430,2	645

Ga_{0.9978}Bi_{0.0022} (heating)

<i>T/K</i>	<i>Freque.1, s⁻¹</i>	<i>Freque.2, s⁻¹</i>	<i>Freque.3, s⁻¹</i>
314	5204.4 ± 4	14751.8 ± 28	27065.0 ± 30
318	5207.9 ± 8	14736.6 ± 45	27099.0 ± 58
320	5203.3 ± 5	14749.0 ± 23	27109.1 ± 73
322	5210.9 ± 7	14736.0 ± 28	27091.4 ± 42
324	5206.1 ± 1	14755.0 ± 31	27104.8 ± 46
326	5306.0 ± 9	15017.1 ± 0.4	27625.5 ± 43
343	5306.9 ± 7	15021.4 ± 34	27554.3 ± 60
<i>q/cm⁻¹</i>	214.9	430.2	645

Ga_{0.9978}Bi_{0.0022} (cooling, last measurements)

<i>T/K</i>	<i>Freque.1, s⁻¹</i>	<i>Freque.2, s⁻¹</i>	<i>Freque.3, s⁻¹</i>
331	7840.2 ± 2	13178.4 ± 4	23541.6 ± 51
334	7828.7 ± 5	13188.1 ± 11	23576.1 ± 66
337	7840.2 ± 13	13207.5 ± 6	23576.1 ± 42
339	7834.4 ± 9	13188.1 ± 22	23507.0 ± 37
<i>q/cm⁻¹</i>	278.58	394.6	580.38

*Ga*_{0.99266}*Bi*_{0.00734} (cooling)

<i>T</i> / K	<i>Freque.1</i> , s ⁻¹	<i>Freque.2</i> , s ⁻¹	<i>Freque.3</i> , s ⁻¹
402	5369.0 ± 52	15172.2 ± 22	27871.2 ± 101
395	5356.4 ± 12	15163.1 ± 19	27865.2 ± 82
392	5366.3 ± 3	15125.7 ± 40	27782.0 ± 38
389	5347.5 ± 2	15122.4 ± 27	27773.3 ± 33
387	5352.5 ± 10	15125.7 ± 10	27772.8 ± 54
385	5278.4 ± 16	14937.3 ± 12	27378.6 ± 53
383	5277.8 ± 9	14935.2 ± 17	27378.9 ± 87
380	5272.5 ± 10	---	---
<i>q</i> / cm ⁻¹	220.3	440.7	660.8

*Ga*_{0.99266}*Bi*_{0.00734} (heating)

<i>T</i> / K	<i>Freque.1</i> , s ⁻¹	<i>Freque.2</i> , s ⁻¹	<i>Freque.3</i> , s ⁻¹
386	8287.2 ± 9	23689.7 ± 68	17188.6 ± 10
388	8291.4 ± 4	23662.1 ± 34	17189.2 ± 12
390	8415.5 ± 5	24005.0 ± 117	17440.5 ± 11
392	8429.1 ± 4	24025.0 ± 107	17428.7 ± 12
394	8444.3 ± 9	24030.0 ± 82	17459.1 ± 10
396	8433.3 ± 5	24029.0 ± 7	17456.8 ± 9
398	8441.2 ± 5	24032.0 ± 38	17432.7 ± 13
403	8433.4 ± 3	24031.0 ± 24	17452.7 ± 11
<i>q</i> / cm ⁻¹	297.8	599.18	483.9

*Ga*_{0.9873}*Bi*_{0.0127} (cooling)

<i>T</i> / K	<i>Freque.1</i> , s ⁻¹	<i>Freque.2</i> , s ⁻¹	<i>Freque.3</i> , s ⁻¹
412	7515.1 ± 5	20970.5 ± 13	9988.0 ± 6
414	7577.1 ± 4	21117.4 ± 18	10086.7 ± 8
416	7570.7 ± 3	21130.7 ± 8	10087.0 ± 4
418	7589.7 ± 4	21136.8 ± 11	10094.8 ± 4
420	7579.7 ± 5	21141.1 ± 25	10075.3 ± 7
427	7574.0 ± 3	21145.9 ± 11	10068.2 ± 7
<i>q</i> / cm ⁻¹	279.37	553.65	337.71

*Ga*_{0.9873}*Bi*_{0.0127} (heating)

<i>T</i> / K	<i>Freque.1</i> , s ⁻¹	<i>Freque. 2</i> , s ⁻¹	<i>Freque.3</i> , s ⁻¹
415	11656.4 ± 11	17367.3 ± 20	9588.4 ± 15
417	11745.6 ± 10	17500.0 ± 21	9668.4 ± 14
424	11739.4 ± 13	17509.8 ± 15	9670.0 ± 10
<i>q</i> / cm ⁻¹	374.2	488.4	328.54

Ga_{0.9994}Pb_{0.0006} (cooling)

<i>T/K</i>	<i>Freque.1, s⁻¹</i>	<i>Freque.2, s⁻¹</i>	<i>Freque.3, s⁻¹</i>
378	5990.1 ± 38	14819.6 ± 63	27730.0 ± 111
365	5987.9 ± 31	14809.7 ± 72	27718.9 ± 108
362	5989.6 ± 32	14802.1 ± 60	27703.8 ± 90
360	5985.7 ± 28	14808.6 ± 66	27705.6 ± 128
358	5983.0 ± 23	14807.5 ± 71	27703.6 ± 146
356	5928.4 ± 23	14675.9 ± 56	27428.8 ± 143
354	5931.9 ± 21	14671.5 ± 60	27421.9 ± 157
352	5930.6 ± 20	14674.8 ± 51	27422.6 ± 125
<i>q/cm⁻¹</i>	232.2	424.6	644.4

Ga_{0.9994}Pb_{0.0006} (heating)

<i>T/K</i>	<i>Freque.1, s⁻¹</i>	<i>Freque.2, s⁻¹</i>	<i>Freque.3, s⁻¹</i>
358	11442.7 ± 21	32100.0 ± 72	16390.7 ± 33
360	11471.4 ± 23	32094.6 ± 79	16391.0 ± 35
362	11568.9 ± 31	32462.8 ± 107	16551.7 ± 48
370	11592.2 ± 29	32477.1 ± 99	16545.5 ± 49
<i>q/cm⁻¹</i>	360	716.23	456.9

Ga_{0.9994}Pb_{0.0006} (second sample)

<i>T/K</i>	<i>Freque.1, s⁻¹</i>	<i>Freque.2, s⁻¹</i>	<i>Freque.3, s⁻¹</i>
353	6070.18 ± 7	14704.71 ± 18	24139.74 ± 32
356	6064.21 ± 8	14734.04 ± 17	24107.25 ± 36
358	6113.34 ± 6	14863.41 ± 22	24302.48 ± 39
363	6123.78 ± 7	14834.66 ± 23	24381.64 ± 42
367	6131.54 ± 7	14865.38 ± 25	24341.2 ± 40
372	6137.1 ± 6	14914.1 ± 25	24386.3 ± 41
374	6127.39 ± 7	14889.69 ± 31	24410 ± 32
<i>q/cm⁻¹</i>	235.7	425.63	591.8

References

- 1- K. Christmann, *Surface physical chemistry*, Steinkopf, Darmstadt, (1991).
- 2- R.J. Borg, G.J. Dienes, *The physical chemistry of solids*, Academic Press Inc., San Diego, (1992).
- 3- J.W. Cahn, *J. Chem. Phys.* **66** (1977) 3667.
- 4- B. Widom, *J. Chem. Phys.* **68** (1978) 3878.
- 5- S. Dietrich, in: C. Domb, J. Lebowitz (Eds), *Phase transitions and critical phenomena*, Academic Press, London, (1988); J. Charvolin, J. F. Joanny, J. Zinn-Justin (Eds), *Liquids at interfaces*, Elsevier, Amsterdam, (1990); S. Dietrich, G. Findenegg, W. Freyland (Eds), *Phase transitions at interfaces*, Proceedings Bunsen discussion meeting, *Ber. Bunsenges. Phys. Chem.* (1994) 98(3).
- 6- J.H. Perepezko, C. Galang, K.P. Cooper in: G.E. Rindone (Ed.), *Materials processing in the reduced gravity environment of space*, Elsevier, Amsterdam, 1982, 491.
- 7- W. Freyland, D. Nattland, *Ber. Bunsenges. Phys. Chem.* **102** (1998) 1.
- 8- D. Nattland, P.D. Poh, S.C. Müller, W. Freyland, *J. Phys. Condens. Matter* **7** (1995) L457.
- 9- E.B. Flom, Mengyangli, A. Acero, N. Maskil, S.A. Rice, *Science* **206** (1993) 332.
- 10- N. Lei, H. Zhengqing, S.A. Rice, *J. Chem. Phys.* **104** (1996) 4802; *ibid.* **105** (1996) 9615.
- 11- H. Tostmann et al., *Phys. Rev. Lett.* **84** (2000) 4385.
- 12- A. Turchanin, D. Nattland, W. Freyland, *Chem. Phys. Lett.* **337** (2001) 5.
- 13- D. Chatain, P. Wynblatt, *Surf. Sci.* **345** (1996) 85.
- 14- P. Wynblatt, A. Saul, D. Chatain, *Acta Mater.* **46** (1998) 2337.
- 15- C. Serre, P. Wynblatt, D. Chatain, *Surf. Sci.* **415** (1998) 336.
- 16- P. Wynblatt, D. Chatain, *Ber. Bunsenges. Phys. Chem.* **102** (1998) 1142.
- 17- B. Yang, D. Gidalevitz, Li. Dongxu, H. Zhengqing, S.A. Rice, *Proc. Nat. Acad. Sci. USA*, **96** (1999) 13009.
- 18- H. Löwen, *Phys. Rep.* **237** (1994) 249.
- 19- J.F. van der Veen, J.W.H. Frenken, *Surf. Sci.* **178** (1986) 382; J.F. van der Veen, *Surf. Sci.* **433-435** (1999) 1.

- 20- D.M. Zhu, J.G. Dash, *Phys. Rev. Lett.* **60** (1988) 432.
- 21- H. Dosch, T. Höfer, J. Peisel, R.L. Johnson, *Europhys. Lett.* **15** (1991) 527; J.G. Dash, H. Fu, J.S.E. Ettläufer, *Rep. Prog. Phys.* **58** (1995) 115.
- 22- J.C. Earnshaw, C.J. Hughes, *Phys. Rev. A.* **46** (1992) 4494.
- 23- J.C. Earnshaw, C.J. Hughes, *Prog. Colloid. Polym. Sci.* **93** (1993) 108.
- 24- X.Z. Wu, E.B. Sirota, S.K. Sinka, B.M. Ocko, M. Deutsch, *Phys. Rev. Lett.* **70** (1993) 958; *Phys. Rev. Lett.* **80** (1998) 1264.
- 25- O. Gang, B.M. Ocko, X.Z. Wu, E.B. Sirota, M. Deutsch, *Phys. Rev. Lett.* **82** (1999) 588.
- 26- T.K. Xia, U. Landman, *Phys. Rev. B.* **48** (1993) 11313.
- 27- M. Heni, H. Löwen, *Phys. Rev. Lett.* **85** (2000) 3668.
- 28- B. Pluis, J.W.H. Frenken, J.F. van der Veen, *Surf. Sci.* **239** (1990) 282.
- 29- A. Turchanin, D. Nattland, W. Freyland, *Phys. Chem. Chem. Phys.* **4** (2002) 647.
- 30- C. Serre, D. Chatain, P. Wynblatt, M. Muris, M. Bienfait, *Metallurgical and Materials Transactions A*, **32** (2001) 2851.
- 31- N.W. Ashcroft, N.D. Mermin, *Solid state physics*, Holt, Rinehart and Winston, New York, (1976).
- 32- H. Tostmann, E. DiMasi, P.S. Pershan, B.M. Ocko, O.G. Shpyrko, M. Deutsch, *Phys. Rev. B.* **61** (2000) 7284.
- 33- M.J. Regan, P.S. Pershan, O.M. Magnussen, B.M. Ocko, M. Deutsch, L.E. Berman, *Phys. Rev. B.* **55** (1997) 15874.
- 34- O.M. Magnussen, B.M. Ocko, M.J. Regan, K. Penanen, P.S. Pershan, M. Deutsch, *Phys. Rev. Lett.* **74** (1995) 4444.
- 35- W. Freyland, *Comm. Sol. State Phys.* **1** (1981) 10.
- 36- M.J. Regan, E.H. Kawamoto, S. Lee, P.S. Pershan, N. Maskil, M. Deutsch, O. M. Magnussen, B.M. Ocko, L.E. Berman, *Phys. Rev. Lett.* **75** (1995) 2498.
- 37- M.J. Regan, P.S. Pershan, O.M. Magnussen, B.M. Ocko, M. Deutsch, L.E. Berman, *Phys. Rev. B.* **54** (1996) 9730.
- 38- C.A. Croxton, *Statistical mechanics of the liquid surface*, John Wiley & Sons, Chicester, (1980).
- 39- P.W. Atkins, *Physical chemistry*, Oxford University Press, Oxford, (1997).
- 40- M. Schick, in: J. Charvolin, J.F. Joanny, J. Zinn-Justin (Eds.), *Liquids at interfaces, Proceedings of the Les Houches 1998 Session XLVII*, North Holland.
- 41- P.G. de Gennes, *Rev. Mod. Phys.* **57** (1985) 827.

- 42- D. Bonn, D. Ross, *Rep. Prog. Phys.* **64** (2001) 1085.
- 43- D. Nattland, P.D. Poh, S.C. Müller, W. Freyland, *J. Non-Cryst. Solids*, **205-207** (1996) 205.
- 44- D. Langevin, *Light scattering by liquid surfaces and complementary techniques*, Marcel Dekker, New York, (1992).
- 45- H.Z. Cummins, in: H.Z. Cummins, E.R. Pike (Eds.), *Photon correlation and light beating spectroscopy*, Plenum, New York, (1974).
- 46- V.G. Levich, *Physicochemical hydrodynamics*, Prentice Hall, New York, (1962).
- 47- H. Lamb, *Hydrodynamics*, Dover, New York, (1945).
- 48- M.G. Muñoz, L. Luna, F. Monroy, R. Runio, F. Ortega, *Langmuir* **16** (2000) 6657.
- 49- J.G.H. Joosten, A. Vrij, H.M. Fijnaut, *Physicochem. Hydrodyn.* **2** (1977) 639.
- 50- E.H.L. Reynders, J. Lucassen, *Adv. Colloid Interface Sci.* **2** (1969) 347.
- 51- A.C. McLaughlin, J.C. Earnshaw, *Journal of Colloid and Interface Science* **158** (1993) 247.
- 52- L. Kramer, *J. Chem. Phys.* **55** (1971) 2097.
- 53- C.F. Tejero, M. Baus, *Mol. Phys.* **54** (1985) 1307.
- 54- K.E. van Holde, *Physical Biochemistry*, Prentice Hall, Englewood Cliffs, NJ, (1985).
- 55- D.A. McQuarrie, *Statistical mechanics*, Harper Collins, New York, 1976.
- 56- M. von Schmoluchowski, *Ann. Physik.* **25** (1908) 225.
- 57- S. Hård, Y. Hamnerius, O. Nilsson, *J. Appl. Phys.* **47** (1976) 2433.
- 58- V. Kolevzon, *Quasi-elastic light scattering from capillary waves at the liquid metal surface, Dissertation*, Technische Universität Berlin, Berlin, 1997.
- 59- E. Hecht, *Optics*, Addison-Wesley, Reading, MA, 1987.
- 60- D. Byrne, J.C. Earnshaw, *J. Phys. D: App. Phys.* **12** (1979) 1133.
- 61- A.C. McLaughlin, J.C. Earnshaw, *Applied Optics* **28** (1989) 5266.
- 62- B. Predel, *Z. Phys. Chem. NF* **24** (1960) 206; I. Ansara, F. Ajerseh, *J. Phase Equilib.* **12** (1991) 73.
- 63- I. Masanori, S. Takeda, U. Tetsuo, *J. Phys. Soc. Jpn.* **61** (1992) 3203.
- 64- S. Hård, R. Neuman, *Journal of Colloid and Interface Science* **115** (1987) 73.
- 65- V. Kolevzon, *J. Phys. Condens. Matter* **12** (2000) 1657.
- 66- S.C. Hardy, *Journal of Crystal Growth* **71** (1985) 602.

- 67- S.P. Yatsenko, V.I. Kononenko, A.L. Sukhmann, *High. Temp. (USSR)*, **10** (1975) 55.
- 68- Kh.B. Khokonov, S.N. Zadumkin, B.B. Alchagirov, *Electrokhimiya* **10** (1974) 911.
- 69- U. König, W. Keck, *J. Less-Common Metals* **90** (1983) 299.
- 70- A.A. Karashaev, S.N. Zadumkin, A.I. Kukhno, *Russ. J. Phys. Chem.* **41** (1967) 329.
- 71- U.V. Arsamikov, R.U. Goitemirov, R.Kh. Dadashev, Kh.I. Ibragimov, *Adgez. Rasplavov Paika. Mater.* **25** (1991) 26.
- 72- O.G. Ashkhotov, M.V. Zdravomyslov, *Poverkhnost* **11** (1996) 15.
- 73- H. Reichert (Private communication).
- 74- V.V. Filippov, P.S. Popel, *Acta Physica Slovaca, Bratislava* **47** (1997) 109.
- 75- *Gmelins Handbuch der Anorganischen Chemie*, Blei, Teil C1, System Nr. 47, (1969).
- 76- J. Vollman, D. Riedel, *J. Phys. Condens. Matter* **8** (1996) 6175.
- 77- J.C. Earnshaw, *Physics Letters* **92** (1982) 40.
- 78- A.H. Ayyad, W. Freyland, *Surf. Sci.* **506** (2002) 1.
- 79- J.C. Earnshaw, E. McCoo, *Phys. Rev. Lett.* **72** (1994) 84.
- 80- V. Kolevzon, *J. Chem. Phys.* **106** (1997) 5816.
- 81- W.H. Shih, D. Stroud, *Phys. Rev. B.* **33** (1986) 8048.
- 82- M.P. D'Evelyn, S.A. Rice, *Phys. Rev. Lett.* **47** (1981) 1844.
- 83- M.P. D'Evelyn, S.A. Rice, *Faraday Symp. of the Royal Society of Chemistry*, No. **16** (1982).
- 84- R. Defay, I. Prigogine, A. Bellemans, D.H. Everett, *Surface tension and adsorption*, Longmans, London, (1966).
- 85- I. Ansara, F. Ajersch, *J. Phase Equilib.* **12** (1991) 73.
- 86- N. Maeda, V.V. Yaminsky, *International Journal of Modern Physics B.* **15**(23) (2001) 3055.
- 87- A.H. Ayyad, I. Mechdiev, W. Freyland, *Chem. Phys. Lett.* **359** (2002) 326.
- 88- W. Freyland, A. H. Ayyad, I. Mechdiev, *J. Phys. Condens. Matter* (submitted).
- 89- W.A. Adamson, P.A. Gast, *Physical chemistry of surfaces*, J. Wiley and Sons, New York, (1997).
- 90- D. Turnbull, *J. Appl. Phys.* **21** (1950) 1022.
- 91- B. B. Laird, *J. Chem. Phys.* **115** (2001) 2887.

92- S. Dietrich, M. Schick, *Surf. Sci.* **382** (1997) 178.

Curriculum Vitae

Ahmed H.A. Ayyad

PERSONAL DATA

Family name: Ayyad
First names: Ahmed Hassan Ahmed
Date of birth: 25th Oct. 1969
Place of birth: Abu Dees, East Jerusalem, Palestine
Nationality: Palestinian
Marital status: Married, one daughter

BASIC EDUCATION

1976-1982 Elementary school, Abu-Dees, East Jerusalem
1982-1985 Junior high school, Abu-Dees, East Jerusalem
1985-1989 High school, Al-Rashidia, East Jerusalem

SCIENTIFIC CAREER

1992-1996 B.Sc. in chemistry
Al-Quds University, East Jerusalem, Palestine
1996-1998 M.Sc. in physical chemistry
Department of Physical and Macromolecular Chemistry,
Leiden University, Leiden, The Netherlands
Supervisor: Dr. J.A.M. Smit
1999-2002 Ph.D. Physical chemistry
Institute of Physical Chemistry, Karlsruhe University,
Karlsruhe, Germany
Promoter: Prof. Dr. W. Freyland

Acknowledgements

In the end, I would like to thank all those people who made it possible for me to finish this work.

Prof. Dr. W. Freyland for welcoming me in his group and offering me the possibility to carry out Ph.D. research on a high level of personal and scientific challenges, for our fruitful discussions and teaching me things that I would never have learned without his broad vision.

Prof. Dr. M. Ballauff for his acceptance of taking part as a co-referee.

Dr. V. Kolevzon for introducing me to capillary wave spectroscopy.

Dr. O. Terakado for his helping out time to time, for critical reading of this thesis and providing me with useful comments.

Dr. D. Nattland for his availability whenever there was a need for substantial discussion.

Dr. I. Mechdiev for his friendly co-working, and for reminding me that mathematics is a cornerstone of physical chemistry.

Mr. Ernesti for the smart and quick solutions to technical problems that would not have been tackled without him, and for his patience with my personal hurry and eagerness concerning cleaning the Mo crucible.

Mr. Rotter for making my wonderful glass syringes that made the Gallium flow shiny. The people of the mechanical workshop of the institute, for constructing the lovely UHV-chamber and helping me whenever a technical problem arose.

The people of the electrical workshop of the institute, for assistance in case of problems with electrical components.

All the people of the 'condensed matter group' (PC I) for contributing to a positive work atmosphere.

Last but not least my wife for helping me with typing and correcting my English, and my daughter for hardly letting me work at home.